PHOTOPHYSICAL MECHANISM OF PHOTOACTIVATION OF THE ORANGE CAROTENOID PROTEIN

By

Justin Brian Rose

A DISSERTATION

Submitted to
Michigan State University
in partial fulfillment of the requirements
for the degree of

Chemistry - Doctor of Philosophy

2024

ABSTRACT

In cyanobacteria, the orange carotenoid protein (OCP) mediates nonphotochemical quenching of bilin excited states in the phycobilisome. An intrinsic ketocarotenoid serves in OCP as an ambient light-intensity sensor by triggering the conversion of the resting, orange form (OCP^O) to the active, red form (OCP^R), which can then bind to the phycobilisome's core.

We have performed absorbance and fluorescence measurements to determine the process by which the carotenoid mediates photoactivation. This dissertation describes an intermediate protein species between the resting and active states, which is formed by the separation of a protein dimer unit into two separate monomers. This intermediate, herein named OCP^I, converts further to form the active state, OCP^R. A wavelength-dependent study of the photoactivation process reveals increased rates of photoproduct formation when exposed to higher energy actinic light. Contrary to previous literature asserting that the photoactivation process occurs due to bond length alternation, these results suggest that the carotenoid distorts through nonplanar coordinates to initiate the photoactivation process.

We subsequently measured the distortion of the ketocarotenoid canthaxanthin (CAN) through fluorescence anisotropy. These experiments reveal CAN undergoes twisting and bending displacements along the isoprenoid backbone during the decay pathway from the S_2 state via the S_X intermediate to the dark S_1 state, even when sterically constrained. In solution, the carotenoid forms a pyramidal structure with significant intramolecular charge-transfer character. However, in the protein cavity, the carotenoid distorts primarily through concerted volume-conserving motions of more than one carbon bond, such as those of the "bicycle-pedal" mechanism.

These findings indicate definitively that the photoactivation process is initiated by torsional motions of the ketocarotenoid inside the OCP structure, and that these motions are not hindered by the protein's residues. We propose that the ketocarotenoid triggers the photoactivation reaction by shortening its effective length through multiple out-of-plane distortions, thereby breaking hydrogen bonds with the protein and allowing displacement of the C-terminal domain.

Standing on the shoulders of giants

ACKNOWLEDGEMENTS

It seems that the passage of time has little to do with calendar years and much to do with self-identifying your personality, thoughts, and interests at discrete points in life. Matriculating at the Virginia Military Institute feels no further than beginning graduate school, nor is it further than publishing my first manuscript in 2022; these experiences equally feel like a lifetime ago. This sentiment evidences the extraordinary personal growth opportunities offered by a doctoral education. As I pass this juncture in my life, I would like to acknowledge the many individuals who have contributed to my professional and personal development.

I extend my deepest gratitude to Professor Warren F. Beck for the opportunity to research within his group. Your exceptional tutelage, paired with your friendly and generous working environment, was pivotal to my academic and personal growth, making me the person I am today. I am also indebted to my senior students, Dr. Jessica Gurchiek and Dr. Ryan Tilluck, who shaped me into an independent student researcher capable of persevering till the end.

Persisting through graduate school would not have been worthwhile without the companionship of my colleagues, Dr. Nila Mohan, Dr. Sourav Sil, Chase Leslie, and Kunwei Yang. Your camaraderie made the best moments better, and your solidarity eased times of hardship. Thank you also to our group's junior students, Shanu Shameem and Megha Dinesh, who have given me one last opportunity to lose myself in my love of teaching.

Special thanks are also owed to Professor John McCracken, who openhandedly shared laboratory equipment, technical advice, and fun conversations.

Over a decade ago and seven hundred miles away, the faculty of Fork Union Military Academy started my success story: Thank you to CPT Michael Pavlansky, who taught leadership in its purest form, COL Carl Muench, who provided my first lesson of mathematics as a tool for understanding our world, CPT Matthew Perry, whose personal character inspired me to major in chemistry and attend VMI, and COL Robert Grant, whose sincere interest in my happiness and success was the foundation of my cadetship.

Many lessons learned at the Virginia Military Institute echo[1] through my life today. Thank you to COL Stanton Smith for the initial experiences conducting chemical research and instructing, SFC Christopher Bean for his friendship and validation of my performance as a cadet, and CDR Charles "Chip" Barber for lessons in professional conduct outside of the military. Lastly, a belated thanks to the many cadre and upperclassmen who "helped" me develop resilience when confronted with adversity.

As I prepare for a career in the United States Space Force, I would like to thank those who made the opportunity possible: Mr. Adrian Law, who made every imaginable resource available from day one, COL Rhet Turnbull, whose career guidance solidified my interest in a commission, and MSgt. Larry Fishel, whose operational efficiency turned a dream into reality.

No one has impacted me more than my wife, Marissa, whose love and support have enabled all my accomplishments. Words cannot convey my gratitude and appreciation. I simply hope to make you proud.

[1] Violence, Intensity, Discipline, *Tiger Echo!*

TABLE OF CONTENTS

OVERVIEW OF THE DISSERTATION

The purpose of the work presented in this dissertation is to determine how the Orange Carotenoid Protein (OCP) senses ambient light conditions and initiates photoactivation when light conditions are too intense. A combination of spectroscopic measurements and novel uses of quantum and molecular mechanical theories and software packages has yielded a compelling answer to explain this process. Time-resolved absorbance studies of OCP have revealed a previously unidentified step in the photoactivation mechanism that involves a metastable intermediate, thereby nullifying all previous studies of OCP photoactivation that claimed to produce the final photoproduct with single-photon excitation. Additionally, subsequent fluorescence anisotropy experiments provided a direct measurement of torsional distortion of carotenoids in the excited state as functions of wavelength, temperature, and solvent polarity, thereby definitively establishing a potential energy surface that accurately describes the decay pathways, electronic structure, and spectral properties of carotenoids. When considered together, the results from these experiments allow us to address the following questions:

1. What are the stepwise components of the photoactivation process and which wavelengths of actinic light drive the reaction?

2. What conformational distortions does the carotenoid undergo while relaxing from the S_2 state, through the S_X state, to the S_1 state?

3. What are the electronic effects of carbonyl substitution on the carotenoid's β-ionone rings?

4. Is it possible to couple the actions of the carotenoid in solution to that of a carotenoid bound within the protein, and do those actions sufficiently explain the yield of OCP^R formation?

The dissertation is organized as follows:

Chapter 1 provides a brief overview of cyanobacterial systems, of which the Orange Carotenoid Protein belongs, and touches on the biological risks associated with harvesting excess amounts of solar energy. The relationship between OCP and the phycobilisome is explained, underlining

how knowledge of the photoactivation process will also inform studies of how the excess light intensity is quenched. A history of the Orange Carotenoid Protein's discovery, as well as the known factors of its structure and function, are addressed. Additionally, carotenoids that are involved in the photoactivation process are introduced to include a review of their electronic structure and properties.

Chapter 2 outlines a series of absorbance experiments where the evolution of OCP from the resting OCP^O toward the photoactive OCP^R was analyzed as functions of temperature, solvent viscosity, light intensity, and actinic light wavelength. The number of states and their lifetimes were analyzed using global modeling, a practice that is standard in ultrafast absorbance spectroscopy but not previously applied to studying OCP photoactivation. The results identified for the first time an intermediate in the photoactivation process, herein named OCP^I, whereby the dark-stable OCP^O dimer first separates into two separate OCP^O monomers before interaction with a subsequent photon, which forms the final OCP^R photoproduct. The rate of photoproduct formation as a function of photolysis wavelength was investigated, providing much finer granularity in understanding which wavelengths of light create the photoproduct. The action spectrum of photoactivation suggests that the photoactivation process is not caused by planar bond length alternation but likely involves a series of out-of-plane motions to trigger the cascading protein response.

Chapter 3 describes an extensive series of fluorescence measurements of β-carotene and canthaxanthin, carotenoids of the same length but differing in electronic structure and conjugation of the isoprenoid backbone. Fluorescence anisotropy measurements of these carotenoids provided direct evidence of transition dipole moment (TDM) rotation following optical preparation of the excited state. The magnitude of TDM rotation as a function of excitation wavelength revealed a local potential energy barrier on the S_2 energy level, which separates two coordinates of carotenoid distortion, distortion through relatively planar bond length alternation in the Franck-Condon region, and a torsional coordinate which leads to a conical intersection with the S_1 energy level. The roles of the carbonyl substituents on the β-ionone rings of canthaxanthin were identified as stabilizing charge separation, promoting the formation of a pyramidalized zwitterionic structure. A series

of temperature-dependent anisotropy studies revealed that carotenoids also undergo out-of-plane distortions through the volume-conserving "bicycle-pedal" mechanism prior to greater relaxation via torsion about the polyene chain. The fluorescence anisotropy of OCP binding canthaxanthin (OCP-CAN) was measured, indicating that the residues of the protein promote the "bicycle-pedal" distortion mechanism, whereby the effective length of CAN is shortened until it can no longer form hydrogen bonds with the protein, causing photoactivation.

Chapter 1: Background: Photoprotection in Cyanobacteria by the Orange Carotenoid Protein

Commonly known as blue-green algae, cyanobacteria are a group of bacteria that carry out oxygenic photosynthesis. Photosynthetic energy is harvested by the cyanobacteria's light-harvesting antenna, the phycobilisome, which transfers energy to chlorophyll. During periods of overly intense ambient light conditions, chlorophyll molecules become saturated with energy and cannot relax before their S_1 states decays to the T_1 state, which then forms biologically dangerous triplet oxygen. Without a protective mechanism, this means uncertain doom for cyanobacteria.

Simultaneously during these intense light conditions, a neighboring Orange Carotenoid Protein (OCP) undergoes protein lysis to form an active state which binds to the phycobilisome. The interaction between the phycobilisome and OCP causes light gathered by the phycobilisome to be dissipated as heat through vibrational means, preventing singlet oxygen formation.

It is important not to anthropomorphize this process: the Orange Carotenoid Protein is an unthinking system, yet it serves as a sensor of ambient light conditions, undergoes a photonically initiated lysis process, quenches phycobilisome energy, and stops quenching when conditions are more favorable. Despite its miraculous importance, the photophysical trigger that initiates these actions is not known. In this dissertation, we aim to solve the mechanism of photoactivation of the Orange Carotenoid Protein.

1.1 Orange Carotenoid Protein

The Orange Carotenoid Protein (Figure 1.1) is a water-soluble protein found within cyanobacteria that mediates nonphotochemical quenching (NPQ) of bilin-excited states in the phycobilisome by serving as a sensor of ambient light intensity. The orange carotenoid protein was first discovered by Holt and coworkers[1] in 1981 when samples of cyanobacterial cells from *Scenedemus obliquus D3* were lysed, separated, and the components were chromatographically purified and cataloged. In addition to the other known components of cyanobacterial cells, a water-soluble orange pigment

with a molecular mass of 47 kDa was extracted, which contained only trace amounts of chlorophyll and other photosynthetic chromophores. However, it was observed that this protein spontaneously changed to a different, red protein with a molecular mass of 27 kDa during the purification process. Spectrally, the absorbance spectrum of the protein in its orange state had a resolved vibronic structure with peaks centered at 465 and 495 nm. In contrast, the red state had an absorption spectrum characterized by a broad, unresolved peak centered at 505 nm. Owing to the similarity of the orange state's absorption spectrum and the absorption spectrum of the carotenoid 3'-hydroxyechininone (3hECN) (Figure 1.5), the protein was identified as containing the carotenoids (Scheme 1) as its light-absorbing pigments.

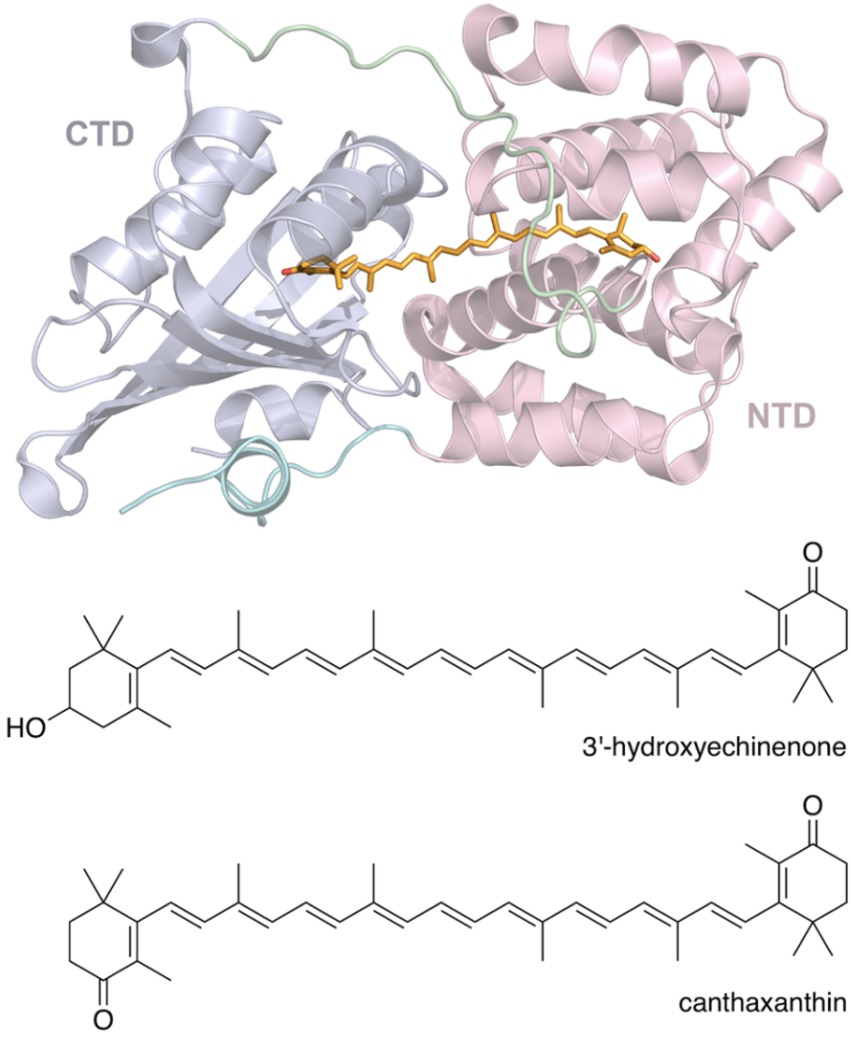

Figure 1.1 Structure in the resting, orange state (OCP^O) from *Arthrospira maxima* (5UI2.pdb). The N- and C-terminal domains (NTD and CTD, respectively) are rendered as red and gray ribbons; the peripheral N-terminal α helix and the linker between the NTD and CTD are rendered green. The bound 3'-hydroxyechinenone (3hECN) is rendered as a stick structure, with carbon atoms in orange and oxygen atoms in red. (Bottom) Structures of the two ketocarotenoids discussed in this study, 3'-hydroxyechininone and canthaxanthin (CAN). Figure reprinted with permission from reference 2. Copyright 2018 American Chemical Society.

Structural details of the Orange Carotenoid Protein were reported by Kerfeld et al.[3] in 2003 following X-ray crystallography of the orange state of OCP (Figure 1.1). Analysis of a crystal of OCP from *Arithrospira maxima* binding 3'-hydroxyechininone revealed that the protein exists as a homodimer, where each monomer is composed of two domains, called the C-terminal domain (CTD) and N-terminal domain (NTD), held together by a linking polypeptide, and which together

bind one carotenoid molecule per monomer. The 3'-hydroxyechininone molecule is in a slightly distorted all-trans configuration within a hydrophobic tunnel between the two domains and held in place by hydrogen bonds between the carotenoid's carbonyl group and the tryptophan-290 and tyrosine-203 residues within the CTD. In contrast, the distal end of the 3'-hydroxyechininone molecule lacking carbonyl substituents does not form hydrogen bonds with the NTD. Although Kerfeld's crystal structure of OCP provided information only for the protein's orange state, it was speculated that the changing absorbance spectrum of the protein resulted from the ability of protein residues to keep the apolar carotenoid within the hydrophobic tunnel within the protein, which preserves the orange absorbance spectrum, and that the absorbance spectrum shifts to the red when the carotenoid interacts with the aqueous surroundings during an unspecified action of the protein.

As the constituent chromophore within OCP is a carotenoid, and since carotenoids commonly feature within cyanobacteria as photoprotective agents, it was presumed that OCP served to regulate absorbed energy in some way. The specific photoprotective role of OCP's carotenoid was reported by Rakhimberdieva et al.[4] in 2004, where it was determined that OCP was able to quench energy harvested by the phycobilisome (PBS), the light-harvesting antenna within Photosystem II (PS-II). In this study, a mutant of *Synechocystis* sp. PCC 6803 lacking PS-II was used. In the absence of PS-II, the light-harvesting antenna phycobilisomes will emit absorbed light as fluorescence, enabling quantitative measurement of energy quenching in the cell. This study discovered that exposing *Synechocystis* cells to actinic light led to a temporary reduction in PBS fluorescence. Additionally, it was observed that the decrease in fluorescence was more pronounced when higher energy (bluer) actinic light was used. An action spectrum was measured to determine the fluorescence quenching induced by actinic light from 280 nm to 700 nm. The resulting spectrum showed similar peaks and resolution to 3'-hydroxyechininone, which led the researchers to conclude that the quenching process was caused by a carotenoid. From this action spectrum, it was argued that carotenoids in the cell quenched PBS fluorescence through direct electronic interactions or altering the PBS structure to induce a quenching state. This question remains open to this day. However, this study did not specify that the carotenoid responsible for fluorescence quenching was bound within OCP;

instead, it employed a more permissive interpretation that the quenching carotenoid could be any within the cell. However, a subsequent publication by Wilson et al.[5] in 2006 correctly identified that the carotenoid within OCP was causing PBS quenching, which was demonstrated by producing a *Synechocystis* mutant without OCP, which did not show fluorescence quenching after exposure to actinic light.

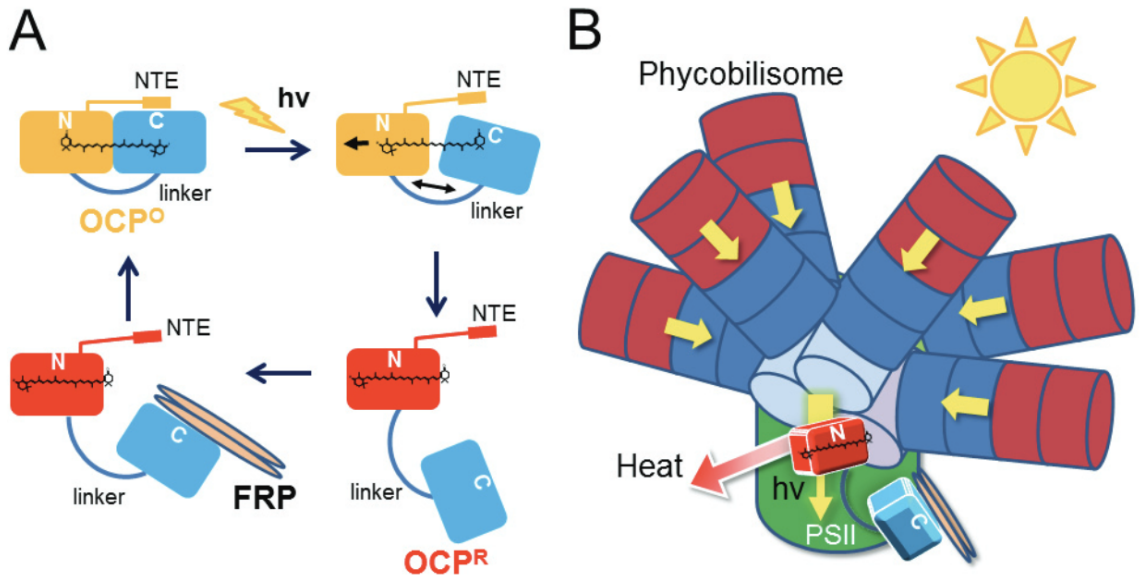

Figure 1.2 Model of the OCP photocycle and the OCP/FRP-related photoprotective mechanism. (A) Mechanism for OCP photoregulation: light absorption by OCP^O induces conformational changes in the carotenoid and domain interfaces, allowing the carotenoid translocation entirely into the NTD, accompanied by complete dissociation of the two domains. Photoactivated OCP^R reverts to inactive OCP^O in darkness and can be accelerated by the interaction between the FRP and CTD. (B) OCP^R interacts with the PBS through the APC trimer of the core to mediate excess energy dissipation as heat. The FRP accelerates the detachment of OCP^R from the PBS. Figure reprinted with permission from reference 6. Copyright 2017 Elsevier.

The observation of OCP's two different absorptive states remained unresolved until a follow-up paper by Wilson et al.[7] in 2008, which demonstrated that the change in visual appearance and molar mass was caused by photolysis with sufficient light intensities. When resting in the dark, OCP adopts the stable orange state, called OCP^O, where the carotenoid is hydrogen bonded to the residues of the CTD. However, after illumination with blue-green light, the carotenoid undergoes distortions that break the hydrogen bonds and allow a protein cascade response, which forms the

red state, called OCP^R, with an estimated quantum yield of 0.03 (Figure 1.2).[6] This mechanism of photoinduced molecular distortion leading to protein reorganization is similar to that of other photoactive proteins, such as Phototropins and the Photoactive Yellow Protein.[8,9] The rate of OCP^R formation increased with higher intensities of actinic light, analogous to the rate of PBS quenching, establishing a direct correlation between the two. Following photoactivation, OCP^R quenches phycobilisomes' fluorescence and recovers to the OCP^O after resting in the dark. The recovery rate shows a strong temperature dependence, increasing at higher temperatures. Following the two proposed quenching mechanisms from Rakhimberdieva, this work supported the hypothesis that OCP quenches PBS fluorescence through direct electronic interactions, postulating that the redshift of OCP^R tunes the absorbance spectrum closer to the electronic S_1 state, increasing the transition overlap of the PBS fluorescence spectrum and OCP absorbance spectrum.

The protein's structural changes associated with photoactivation and PBS quenching were elucidated following advances in the construction of OCP mutants by Wilson et al.,[10] which varied the interfacial protein residues that hold the CTD and NTD together, Glu244 and Arg155, respectively. A sequence of amino acid substitutions for each residue demonstrated that varying the charge on the CTD 244 residue did not affect the binding affinity of OCP to PBS, but decreasing the charge on the NTD 155 residue significantly decreased the binding rate of OCP^R to the PBS, even to the extent of completely prohibiting binding when amino acids with negative charges are introduced. Thus, it was determined that the carotenoid-NTD complex is the specific quenching agent of PBS fluorescence, binding to allophycocyanin molecules in PBS.

The inability of the active OCP^R state to form a stable crystal prevented structural analysis of the protein's NTD and bound carotenoid following photoactivation. Following the advancements in OCP mutant construction, researchers discovered the Red Carotenoid Protein (RCP),[11] an analog of OCP where the CTD is removed through proteolysis, leaving only the NTD and a bound carotenoid molecule, similar to the active OCP^R state (Figure 1.3). The RCP can quench PBS fluorescence like OCP^R and has an absorbance spectrum similar to OCP^R. However, it differs because it is permanently photoactivated and cannot revert to an inactive OCP^O-like state. This characteristic

enables the synthesis of a stable RCP crystal for structural analysis. Information about the difference in carotenoid configuration was reported by Leverenz et al. in 2015.[12] By comparison of the OCP^O and RCP X-ray diffraction crystal structures, it was determined that after the photoactivated protein cascade, the bound carotenoid moves 12 angstroms further into the NTD compared to OCP^O to reduce interaction with the aqueous buffer solution. As a result of this movement, the structure of the carotenoid also changes, leading to a decrease in the out-of-plane torsions of the carotenoid's terminal rings. This change increases the polyene conjugation length of the carotenoid, which is consistent with the redshift in the absorbance spectrum.

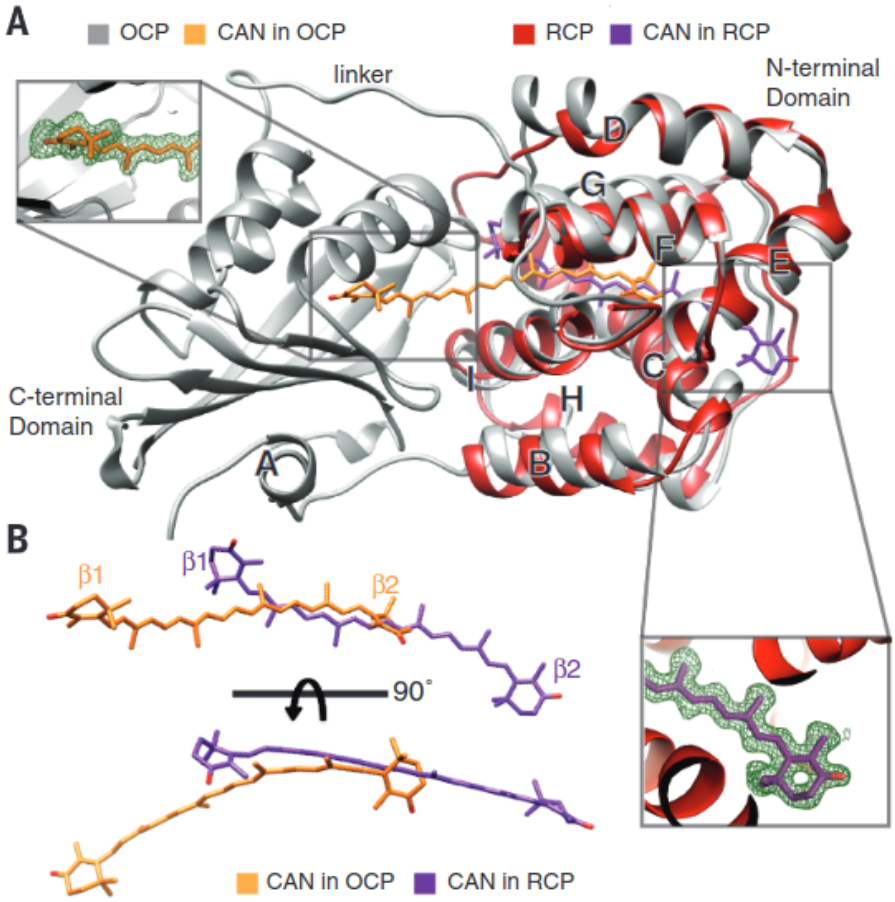

Figure 1.3 Crystal structures of the orange carotenoid protein (OCP) and red carotenoid protein (RCP) binding canthaxanthin (CAN). (A) Superimposed ribbon structures of OCP-CAN (gray) and RCP-CAN (red). CAN is shown in orange sticks in OCP and purple sticks in RCP. Inset panels show representative electron density for the carotenoid in each. (B) CAN structures in OCP and RCP show increased planarity of the polyene chain in RCP and distinctly different β-ionone configurations. Figure reprinted with permission from reference 12. Copyright 2015 AAAS.

Hydrogen bonding within the CTD for select carotenoids was discovered by J. K. Gurchiek[13] of the Beck group in 2018 through analysis of fluorescence results and previously published X-ray crystal structures. In this study, Gurchiek and coworkers compared the fluorescence quantum yields of OCP binding the carotenoids 3'-hydroxyechininone and canthaxanthin, which differ as carotenoid 3'-hydroxyechininone has a carbonyl on the carotenoid's terminal ring in the protein's CTD. In contrast, canthaxanthin has one carbonyl on each terminal ring in the protein's CTD and NTD. The sample of OCP binding 3'-hydroxyechininone had a higher quantum yield than OCP binding canthaxanthin, and the quantum yield of OCP binding canthaxanthin was higher than that of canthaxanthin in solution. Upon close inspection of the X-ray structure data of the canthaxanthin binding site, it was revealed that the terminal ring hydroxyl substituent of 3'-hydroxyechininone in the NTD was within hydrogen bonding distance with the NTD's Leu37 residue (Figure 1.4). Following the theory that OCP photoactivation occurs due to the breaking of hydrogen bonds between the carbonyl and protein residues, the increased quantum yield suggests that the carotenoid is kept in its initial configuration with greater force and thus experiences a longer lifetime before nonradiative decay. Combined with the crystal structure results, this reveals that the cause of restricted molecular motions in the excited state is due to hydrogen bondings of 3'-hydroxyechininone's hydroxyl to the NTD Leu37 residue and, conversely, that large-amplitude motions of the excited state carotenoid initiate OCP^O photochemistry.

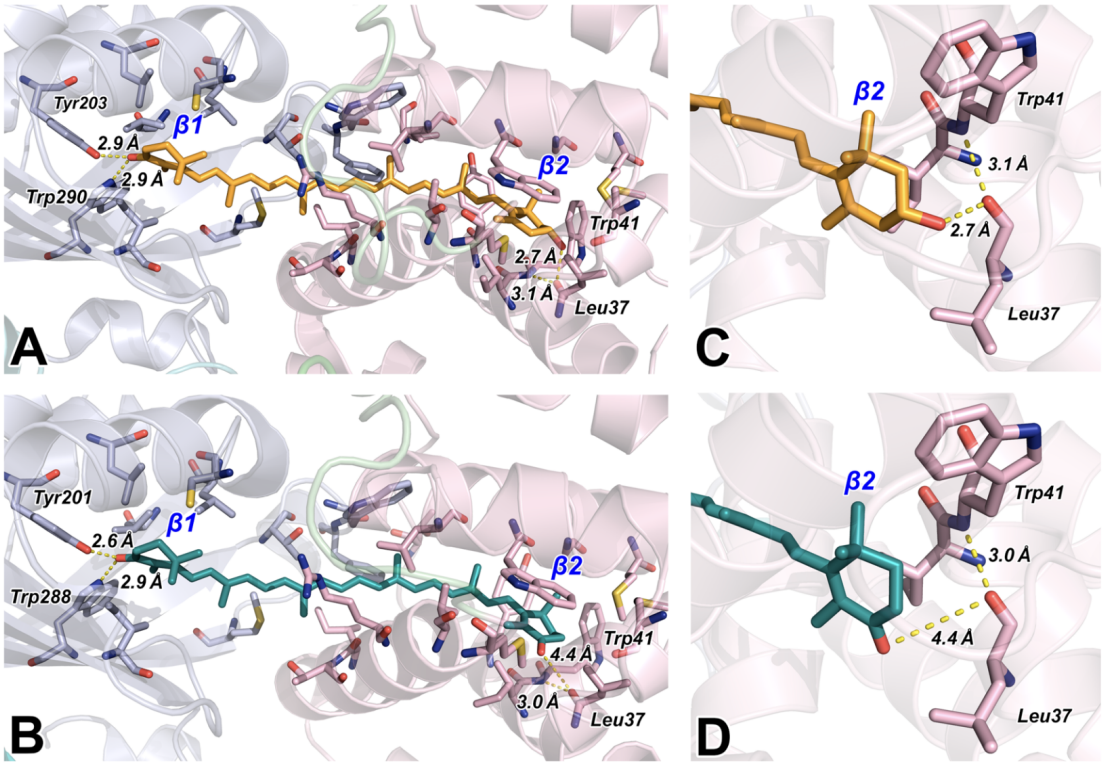

Figure 1.4 Protein-ketocarotenoid hydrogen bonding interactions by the β_1 (CTD) and β_2 (NTD) β-cyclohexene rings of the carotenoids bound in OCP^O: (a) for 3'-hydroxyechininone, from structure 5UI2.pdb from *Arthrospira maxima*; (b) for CAN, from structure 4XB5.pdb from *Synechocystis* sp. PCC 6803 (c) detail from a rotated vantage point of the β_2 ring's hydrogen bonding interaction between the hydroxyl group and the carbonyl on Leu37 and (d) for the clash between the β_2 carbonyl on CAN and that on Leu37. Protons are not displayed in these diagrams. Figure reprinted with permission from reference 2. Copyright 2018 American Chemical Society.

Punginelli et al.[14] further demonstrated the importance of the electronic structure of the carotenoids bound within OCP by expressing a mutant that binds the carotenoid Zeaxanthin, which has hydroxyls on each terminal ring rather than carbonyls. This study created a mutant of OCP binding zeaxanthin and exposed it to the same photolysis conditions as OCP binding 3'-hydroxyechininone and canthaxanthin. Despite being irradiated with actinic light sufficient for the photoactivation of other samples, OCP binding zeaxanthin does not photoactivate, has a permanent OCP^O absorbance spectrum, and does not quench PBS fluorescence. As a result of this work, it was postulated that the carbonyl on the carotenoid's terminal ring in the CTD is essential to photoactivate and quench PBS fluorescence.

1.2 Carotenoid Photophysics

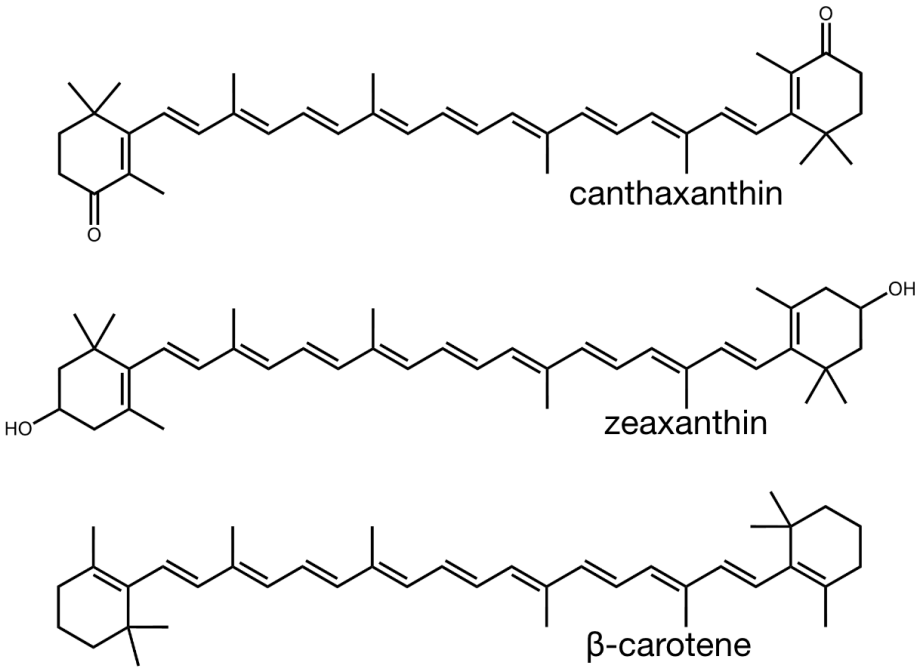

Scheme 1: Structures of essential carotenoids involved in photoregulation.

Carotenoids (Scheme 1) are organic pigments naturally found in higher plants and algal cyanobacteria. Characterized by conjugated polyene chains that absorb visible light, they are responsible for most photosynthetic systems' red, orange, and yellow colors. Carotenoids play multiple roles in photosynthetic systems, including light harvesting via singlet state energy transfer, scavenging singlet oxygen, quenching chlorophyll triplet states, and sensing ambient light conditions.[15,16]

The functions of carotenoids are caused by their two lowest electronic excited states, S_1 and S_2.[15–20] The spectral properties and electronic states of all-trans carotenoids, such as beta carotene, are typically explained through point group theory (Figure 1.5, right). All-trans carotenoids belong to the C_{2h} point group, which assigns the S_0, S_1, and S_2 states as A_g, A_g, and B_u states, respectively. Due to the Laporte rule, the one-photon electric-dipole transition from S_0 to S_1 is forbidden due to symmetry exclusion. However, the population of the S_0 to S_2 state is permitted due to different symmetry characters, resulting in strongly allowed $\pi \rightarrow \pi^*$ transitions caused by the absorbance

of a photon in the mid-visible absorption band. The π* antibonding orbital population causes bond-length alternation (BLA) of the polyene's C=C and C-C bonds, giving rise to a vibronic progression in the ground-state absorption spectrum (Figure 1.5, left).

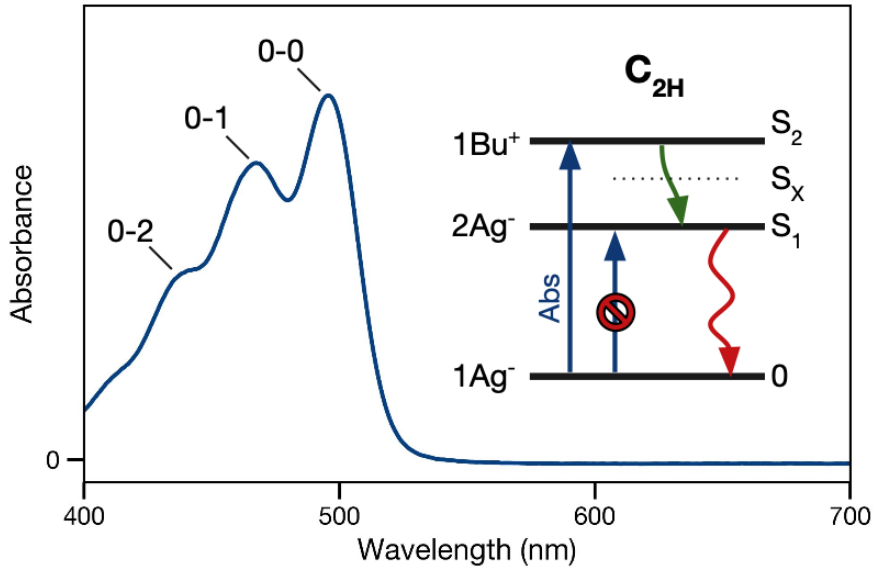

Figure 1.5 Typical absorbance of carotenoids (blue) and symmetry allowed transitions. The structure of carotenoid absorbance is characterized by the vibronic peaks rising from excitation to higher order carbon-carbon vibrational modes (0-0, 0-1, 0-2) following optical preparation of the S_2 energy level from a $\pi \rightarrow \pi^*$ transition. Carotenoids putatitively belong to the C_{2h} point group,[15] prohibiting one-photon transitions from the ground state to the S_1 state due to symmetry exclusion rules.

After populating the S_2 electronic state, which has a lifetime of 140 femtoseconds,[19] carotenoids undergo nonradiative decay to the S_1 state, which has a lifetime of 10 picoseconds and is reached through vibrations of the polyene's C=C and C-C bonds until a conical intersection is reached.[21] Despite one-photon transitions from the S_0 state to the S_1 state being symmetry prohibited, the S_1 state of carotenoids is readily observed through excited-state absorption, which populates higher energy singlet excited states with different symmetrical characters.[21]

Carotenoids, despite being considered planar C_{2h} symmetric molecules,[21] are held in non-planar configurations in solution and in-vacuo, violating C_{2h} symmetry rules.[22–25] In addition, some carotenoids, such as peridinin, have structures that are explicitly non-C_{2h} symmetric, yet one photon population of the S_1 state is prohibited, similar to C_{2h} carotenoids.[26] These observations

suggest that carotenoids' spectroscopic and excited state properties do not result from molecular symmetry but instead originate from their electronic structures and the Franck-Condon overlaps of their potential energy surfaces.[24] Further, due to their theoretical complexity, quantum chemical calculations of carotenoid electronic character, energy orderings, and the potential energy surfaces of the lowest singlet excited states have not been possible.[27–32]

In addition to the known lowest singlet excited states of carotenoids, recent studies of carotenoid photophysical properties describe multiple additional dark excited states at energies adjacent to the S_2 and S_1 states.[15,17,18,21,33] Resonance Raman excitation profiles and ultrafast time-resolved spectroscopy studies suggest that an intermediate dark state, S_X, mediates nonradiative transfer between the S_2 and S_1 energy levels.[34–38] There are currently two theories describing the S_X state. One theory by Polivka et al.[18,21] suggests that S_X is a discrete singlet energy level below S_2. In contrast, the other theory proposed by the Beck research group[13,17–19,33] argues that S_X is an intermediate structure of S_2 as it moves along an out-of-plane portion of the potential energy surface before reaching the conical intersection with S_1.

In the model proposed by the Beck research group, the initial population of the S_2 energy level distorts the carotenoid via bond-length alternation along the polyene chain until a low activation energy barrier is reached.[33,39,40] This barrier separates the regions of the S_2 potential energy surface into planar and out-of-plane distorted conformations. Variations in the carotenoid's electronic structure affect barrier height, particularly the extent of electron-withdrawing character on the carotenoid's terminal rings. Crossing the barrier leads to a steep potential energy gradient characterized by torsional distortion of the carotenoid's polyene chain, leading to a conical intersection of the S_2 and S_1 potential energy surfaces.[28] Following the decay of the S_2 state to the S_1 state near the conical intersection, the carotenoid undergoes conformational relaxation back to the ground state's planar structure.

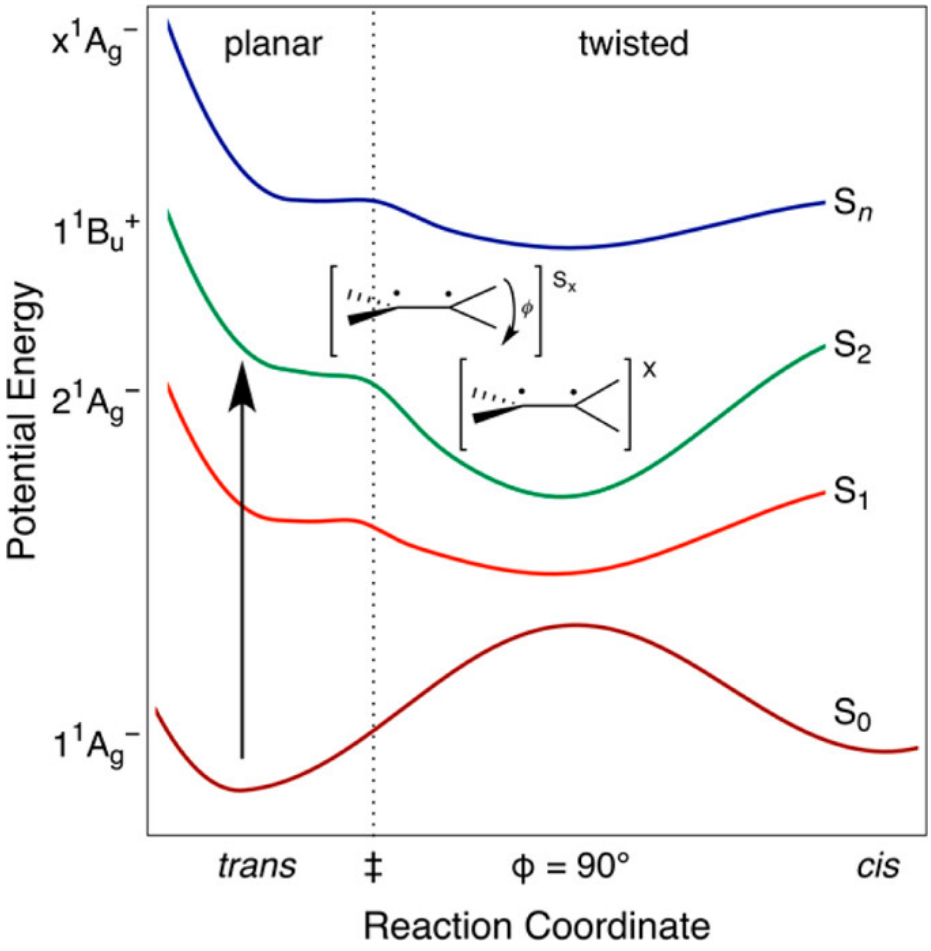

Figure 1.6 Proposed scheme for the radiationless decay of the S_2 state of carotenoids. The states that apply to planar structures are indicated by symmetry labels. The ethylenic structures shown depict the S_x and X states as torsionally distorted S_2 structures near the transition state barrier (‡) and further along the torsional gradient, respectively. Figure reprinted with permission from reference 40. Copyright 2016 American Chemical Society.

Work by Soumen Ghosh[33] of the Beck lab detected the S_x state of the carotenoid peridinin as a dynamic intermediate following the decay of the Franck–Condon S_2 state and before the rise of the ESA from the S_1 state. The lifetime of S_X in various solvents was observed to follow a power law relationship with the polar solvation time of the solvent, suggesting that the transition from the S_X intermediate on the S_2 surface to the S_1 state is mediated by out-of-plane distortions of the polyene chain (Figure 1.6), with the polar solvation dependence indicating the formation of intramolecular charge-transfer (ICT) character across the molecule.

Unlike the significant molar extinction coefficients that give rise to strong absorbance, carotenoids have very low fluorescence quantum yields due to their short excited state lifetimes resulting from non-radiative decay via polyene chain vibrations.[41] Additionally, typical fluorescence measurements of carotenoids include Raman scattering features of the same magnitude as the fluorescence emission, allowing the study of the molecular vibrations that mediate excited state dynamics.[13,41,42] Nonetheless, fluorescence measurements of carotenoids in solution and proteins provide rich details of their excited state dynamics and the effects of electronic structure. Work done in the Beck research group by J. K. Gurchiek[13] measured the fluorescence of the carotenoids 3'-hydroxyechininone and canthaxanthin when bound within a protein and canthaxanthin in chloroform solvent. The fluorescence spectra of both 3'-hydroxyechininone and canthaxanthin within the protein are mirror asymmetric to the absorbance spectrum, but the fluorescence line shapes of the two carotenoids bound within the protein differ significantly. The fluorescence lineshape of 3'-hydroxyechininone within the protein exhibits lognormal characteristics,[43] indicating an unresolved vibronic progression caused by vibrations along the polyene chain. On the other hand, the fluorescence lineshape of canthaxanthin within the protein is Lorentzian, suggesting an extremely short excited state lifetime.[2] These differences are also evidenced by the fluorescence quantum yields, as the longer excited state lifetime of 3'-hydroxyechininone results in the emission of more photons. The fluorescence quantum yield of canthaxanthin in solution was ten times lower than that of canthaxanthin in the protein, and the Lorentzian lineshape was broader than the canthaxanthin bound within the protein, together indicating an extremely short excited state lifetime.[13] These fluorescence results suggested that large distortions of the carotenoid initiate a photochemical response in the protein, moderated by hydrogen bonds between oxygen-bearing substituents on the carotenoid terminal rings and the protein residues (Figure 1.4).[13]

Chapter 2: Photoactivation of the Orange Carotenoid Protein Requires Two Light-Driven Reactions Involving Out-of-plane Distortion

2.1 Summary

The Orange Carotenoid Protein (OCP) functions as a sensor of the ambient light intensity and as a quencher of bilin excitons when it binds to the core of the cyanobacterial phycobilisome. We show herein that the photoactivation mechanism that converts the resting, orange-colored state, OCP^O, to the active red-colored state, OCP^R, requires a sequence of two reactions, each requiring absorption of a photon by an intrinsic ketocarotenoid chromophore. Absorption spectra recorded during continuous illumination of OCP^O preparations from *Synechocystis* sp. PCC 6803 detect the reversible formation of a metastable intermediate, OCP^I, in which the ketocarotenoid canthaxanthin exhibits an absorption spectrum with a partial red shift and a broadened vibronic structure compared to that of the dark-adapted OCP^O state. The lifetime of the OCP^I intermediate is more than twenty minutes in the dark at 293 K. Based on the crystal structure of OCP, we propose that the first step of the photoactivation reaction is a light-induced photodissociation of the dark-stable OCP^O dimer aggregate. Formation of the OCP^O monomer from the dimer increases the mean value and broadens the distribution of the solvent-accessible surface area of the canthaxanthin chromophore measured in molecular dynamics trajectories at 300 K. Absorption of a second photon by canthaxanthin in the monomeric OCP^I intermediate would initiate the second reaction, which obtains the fully red-shifted and broadened absorption spectrum detected in the OCP^R product state owing to displacement of the C-terminal domain and the translocation of canthaxanthin more than 12 Å into the N-terminal domain. An action spectrum of photoactivation reveals that higher energy wavelengths preferentially photoactivate both the OCP dimers and monomers, suggesting that both steps in the photoactivation reaction of OCP involve both bond length alternation and also out-of-plane distortions of canthaxanthin in the structure of the C-terminal domain.

The material in this chapter has been published in another form: Rose, J. B.; Gascón, J. A.; Sutter, M.; Sheppard, D. I.; Kerfeld, C. A.; Beck, W. F. Photoactivation of the Orange Carotenoid Protein Requires Two Light-Driven Reactions Mediated by a Metastable Monomeric Intermediate. *Phys. Chem. Chem. Phys.* **2023,** DOI: 10.1039/d3cp04484j.

2.2 Introduction

The Orange Carotenoid Protein (OCP) mediates nonphotochemical quenching (NPQ) in cyanobacteria by serving as a sensor of the ambient light intensity and by quenching bilin excited states in the core of the phycobilisome.[44–55] Photoactivation of the OCP from the resting, orange-colored state, OCP^O, to the NPQ-active, red-colored state, OCP^R, is driven by absorption of blue-green light by a ketocarotenoid, such as 3'-hydroxyechinenone or canthaxanthin which spans the interface between the N-terminal and C-terminal domains (NTD and CTD, respectively) of the protein. Formation of the active OCP^R product translocates the ketocarotenoid more than 12 Å and allows the CTD to rotate away (Figure 2.1).[53,55] This reorganization of the protein structure of OCP requires dissociation of a dark-stable homodimer complex.[45,51,56,57] The OCP^O dimer is stabilized by salt bridges and hydrogen bonds principally between the parallel facing α helices from the NTD of the two interacting monomers.[45,51] The absorption spectrum of the ketocarotenoid shifts more than 50 nm to the red in response to the structural changes that accompany the translocation of the ketocarotenoid.[52,53] The recent cryo-EM structure of the complex of OCP^R with the phycobilisome shows that the exposed NTD surface associates with allophycocyanin-containing segments in the core, allowing the exposed length of the ketocarotenoid to be inserted near to bilin chromophores along the excitation energy transfer pathway to the terminal emitter bilins.[55]

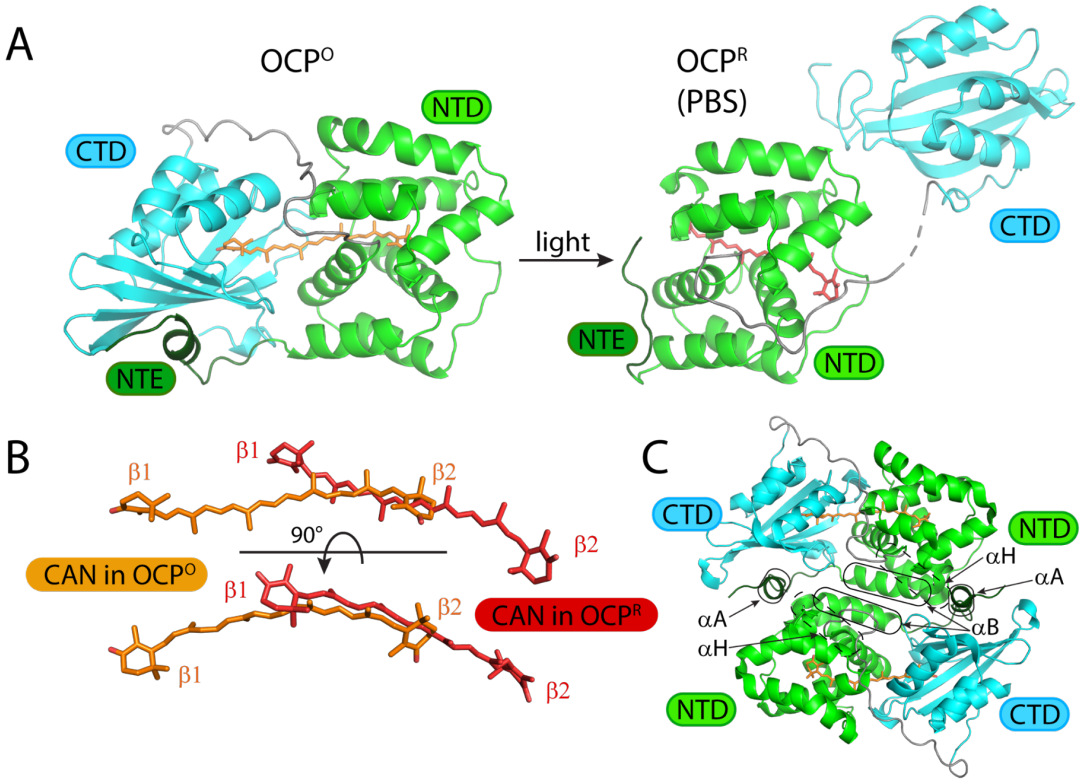

Figure 2.1 Structures of OCP^O, OCP^R, and the OCP^O dimer. (a) Structures of the OCP^O (left, pdb id 4xb5) with canthaxanthin (CAN, orange) and the phycobilisome (PBS)-bound form of OCP^R (right, from the OCP-PBS structure, pdb id 7sc9) with CAN (red). C-terminal domains (CTD) are cyan, N-terminal domains (NTD) green, the N-terminal extension (NTE) dark green, and the connecting linkers grey. (b) Detailed view showing the translocation of CAN in OCP^O (orange) and OCP^R (red) in two orientations, indicating the β-ionone rings in the CTD and NTD, β1, and β2, respectively. (c) Overview of the OCP^O dimer as observed in the crystal structure of Syncechocystis sp. PCC 6803 OCP (pdb id 4xb5), with the α helices labeled that form the major interaction surface between the two monomers. Figure reprinted with permission from reference 58. Copyright 2023 Royal Society of Chemistry.

The photochemical mechanism that initiates photoactivation of OCP following optical excitation of the ketocarotenoid to its second excited singlet state, S_2, remains elusive because the quantum yield of the OCP^R product state is only a few percent at best. Currently available evidence supports the idea that the ketocarotenoid undergoes a change in its conformation during nonradiative decay from the S_2 state that initiates photoactivation in a small number of events. Wilson et al.[49] assigned a non-decaying signal they observed in femtosecond pump–probe spectra to OCP^R

with the ketocarotenoid in the electronic ground state, S_0, with a yield of ~1%. Šlouf et al.[59] subsequently detected light-induced changes in the conformation of the ketocarotenoid in OCP using the magnitude of a S_1-state intramolecular charge transfer (ICT) signal they observed in the near-IR to assess the torsional angles of the beta-ionone end rings. Konald et al.[60] then used information from time-resolved IR spectroscopy to conclude that nonradiative decay from S_2 and S_1 in OCP produces the low-energy S_1 intermediate called S*,[61] which initiates the translocation of the ketocarotenoid by breaking the hydrogen bonds between the carbonyl substituent on the ketocarotenoid's β_1-ionone ring and the side chains of two conserved amino-acid residues in the CTD, Y201 and W288 (in *Synechocystis* sp. PCC 6803).[2,45] A subsequent study by Yaroshevich et al.[62] of OCP with the Y201W mutation led them to propose that this process involves protonation of the carbonyl substituent. However, a recent study by Niziński et al.[63] of pump–probe spectra with coverage of the near-IR region has suggested instead that the first intermediate P_1 in the ketocarotenoid translocation mechanism arises not from S* but from the S_1 state proper. Based on evidence from time-resolved X-ray crystal structures, Chukhutsina et al.[64] raised the alternative proposal that a "bicycle pedal" configuration[65] of the ketocarotenoid's isoprenoid backbone is produced during the photoactivation reaction.

Although the photochemistry of retinal in rhodopsin[66,67] should not be directly compared to that of the ketocarotenoid in OCP,[49] it is similarly assumed in most studies that absorption of a single photon by the ketocarotenoid in OCP initiates the entire sequence of events in the photoactivation mechanism that produces the OCP^R state.[68] The observations by Maksimov et al.[69] and by Niziński et al.[68] that the rate of formation of OCP^R depends nonlinearly on the incident light intensity, however, suggest that the mechanism incorporates a sequence of at least two light-driven reactions. In this contribution, we have investigated this further by using the vibronic structure and red shift of the absorption spectrum of the bound ketocarotenoid canthaxanthin (CAN) as intrinsic probes of the surrounding protein environment during the photoactivation of OCP preparations from *Synechocystis* sp. PCC 6803. Absorption spectroscopy measurements during continuous illumination suggest that absorption of light by CAN first causes dissociation of the dark-stable

OCP^O dimer, which results in partial exposure of the CAN binding site region in between the CTD and NTD to the surrounding aqueous medium.[45] We then find that the monomeric intermediate of OCP is metastable in the dark for at least twenty minutes at 293 K until a second light-driven reaction triggers the formation of OCP^R. We propose that both steps in the photoactivation reaction are triggered by excited-state conformational motions of CAN that are launched in the photoexcited S_2 electronic state.

2.3 Experimental

2.3.1 Orange Carotenoid Protein Sample Preparation

OCP^O preparations from *Synechocystis* sp. PCC 6803 with the ketocarotenoid canthaxanthin (CAN) were isolated as described previously.[2] Briefly, the gene for OCP was expressed in in BL21(DE3) competent *Escherichia coli* cells with a C-terminal 6× His tag added and cloned in a pCDFDuet-1 vector (Novagene). The BL21(DE3) cells were transformed with the pCDFDuet-1 vector and the pAC-CANTHipi plasmid (Addgene plasmid #53301)[70] containing the genes for biosynthesis of CAN in *E. coli*. The OCP-CAN holoprotein was isolated using the method described previously.[53] Ni-NTA affinity chromatography (HisTrap Affinity column, GE Healthcare) was used to obtain a mixture of the apo- and holoproteins, and then the OCP-CAN holoprotein was isolated by hydrophobic interaction chromatography (HiTrap HIC phenyl column, GE Healthcare).

For use in the photoactivation and dark-recovery experiments, the OCP–CAN holoprotein was suspended in a buffer solution containing 50 mM *tris*(hydroxymethyl)aminomethane–NaOH, pH 8.0, and 200 mM NaCl. For some experiments, 60% (*v*/*v*) glycerol was also present as a cryoprotectant. The stock protein solution was diluted 30-fold with the buffer solution chosen for a particular experiment to obtain an absorbance of 0.12 at 505 nm. The OCP–CAN solutions were prepared in the dark and then allowed to further rest at 3 °C for one week in a dark refrigerator prior to use in an experiment. 1.5 mL aliquots were then transferred in total darkness to a fluorescence cuvette and placed in the sample temperature controller in the photoactivation spectrometer. Prior

to illumination, the sample was cooled *in situ* to 273 K and allowed to incubate further in total darkness for 10 min.

CAN (Sigma-Aldrich 11775) was used as received for measurement of the absorption spectrum in 2-methyltetrahydrofuran (Sigma-Aldrich 673277).

2.3.2 Photoactivation Assay Experimental Protocol

Absorption spectra during continuous illumination of OCP preparations were recorded with a home-built multichannel absorption spectrometer. Continuous excitation light for the photoactivation reaction was routed from a 430-nm LED (Thorlabs M430L5) to the sample by a fiber-bundle light guide (Thorlabs OSL2FB) after passing through a computer-controlled shutter (Thorlabs SH-1), a 430-nm interference filter (Thorlabs FB430-10, 10-nm bandpass), and then a stack of neutral density filters, which were varied to adjust the illumination power for a particular experiment. The diameter of the excitation beam was 1 cm across the sample cuvette. A Newport Model 835 power meter equipped with a 1-cm silicon photodiode detector was used to measure the power after the excitation beam passed through a sample cuvette containing a blank solution. The continuous white-light probe beam for the absorption measurement was obtained from a tungsten halogen lamp in an Ocean Optics DH-2000 fiber light source. An Ocean Optics QP400-1-VIS-NIR fiber and a Thorlabs FS240SMA-A fiber collimator were used to direct the unfiltered probe beam (3-mm diameter) across the sample cuvette at 90° incidence from the excitation beam and centered inside its profile across the sample. The integrated power of the probe beam incident on the sample was 450 μW; the total absorbed power due to the ground-state absorption of the OCP sample in the blue-green region of the probe spectrum was 23 μW. The transmitted probe beam was collected by a fiber collimator and then routed by an optical fiber to an Ocean Optics Flame-T grating spectrometer/CCD detector, which was controlled by a LabVIEW (National Instruments) program. During illumination and during the subsequent dark recovery periods, the CCD detector was operated with a 4-ms integration time per scan; 25 successive spectra were integrated to obtain a total acquisition time of 0.1 s per spectrum. The OCP samples were held in 1-cm square fluorescence cuvettes in a Peltier-

type sample temperature controller (Quantum Northwest Luma 40), which was also used to stir the sample continuously with a magnetic stir bar. Singular-value decomposition (SVD) analysis of the time-resolved spectra was performed using the GlobalWorks software package (On-Line Instrument Systems). Global and target modeling employed the GlobalWorks and CarpetView (Light Conversion) software packages.

2.4 Results

2.4.1 Identification of a Meta-stable Photoactivation Intermediate

In line with the results reported by Niziński et al.,[68] our recordings of the photoactivation of OCP under continuous illumination (Figure 2.2) exhibit more than one kinetic phase as OCP^O is converted into OCP^R. The approach we used to determine the mechanism behind this phenomenon was to record snapshots of the absorption spectra of OCP solutions during continuous illumination with blue light (wavelength of 430 nm), which we find results in a more rapid conversion to the OCP^R product than with light at longer wavelengths. Further, we chose initially to record photoactivation assays at 273 K because the dark recovery of OCP^R is slowed by a factor of at least 55 compared to that of the forward photoactivation rate (Figure 2.3).

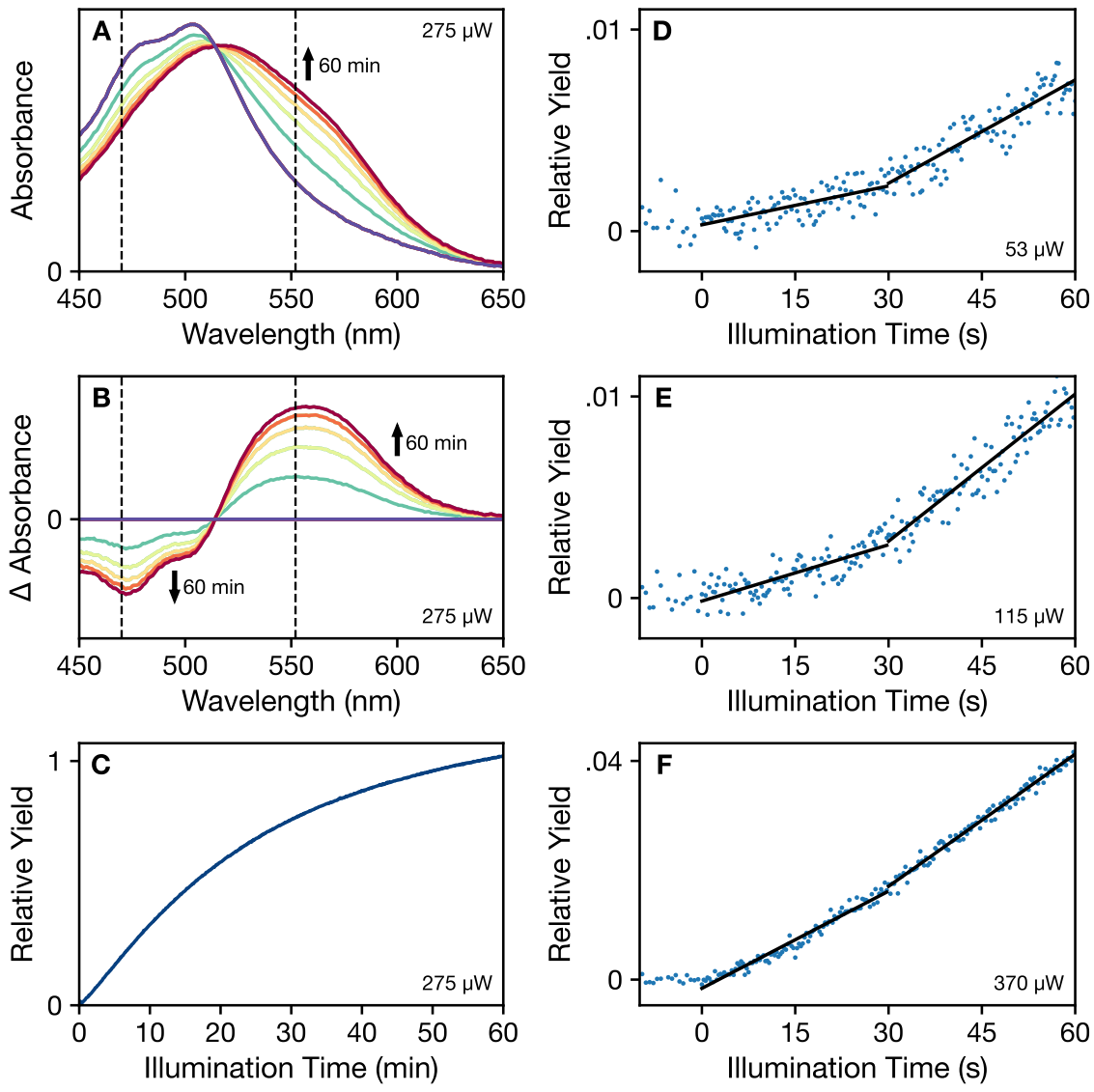

Figure 2.2 Photoactivation assays of dark-adapted OCP at 273 K under continuous 430-nm illumination (275 µW). (a) Time evolution of the absorption spectrum from zero illumination (purple) to 60 min of illumination (dark red), with intermediate spectra spaced by 12 min of illumination. (b) Difference absorption spectra (light - dark adapted) for the set of spectra shown in panel (a). The vertical dashed lines shown in (a, b) mark the wavelengths used for the transients in Figure 2.5. (c) Time course of the relative yield of the OCP^R product, determined from the integral of the absolute value of the difference spectrum. (d-f) Time courses of the relative yields of OCP^R at short illumination times with increasing illumination power: 53 µW, 115 µW, and 370 µW, respectively. The y-axis scaling is consistent with that used in panel (c). Approximately linear segments in these time courses are indicated with superimposed black lines. Figure reprinted with permission from reference 58. Copyright 2023 Royal Society of Chemistry.

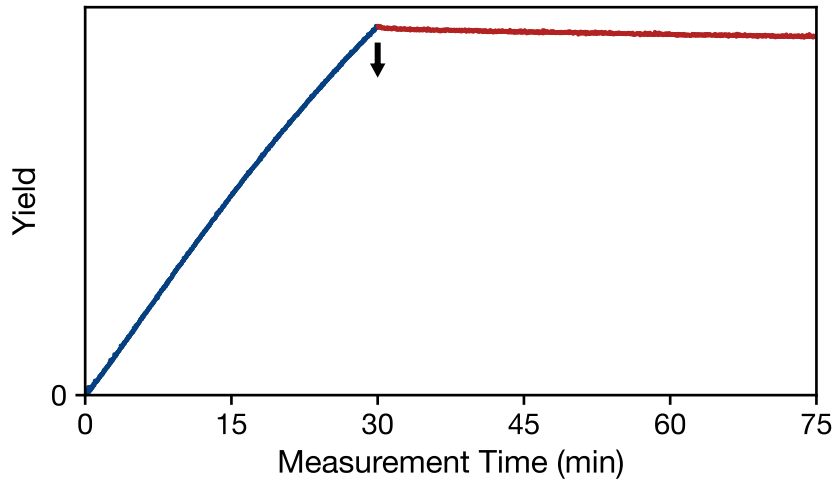

Figure 2.3 Photoactivation and dark recovery of the Orange Carotenoid Protein (OCP) at 273 K in the presence of 60% (v/v) glycerol. The sample was illuminated at 430 nm (275 µW) for 30 minutes (blue) followed by incubation in the dark starting at the down arrow (red). The relative yield was determined as in Figure 2.2 using the integral of the absolute value of the light - initial dark difference spectrum as a function of time. Figure reprinted with permission from reference 58. Copyright 2023 Royal Society of Chemistry.

The series of absorption spectra in Figure 2.2a show the pattern of spectral changes commonly observed as OCP^O is converted to OCP^R under continuous illumination. Extending to bluer wavelengths from the peak maximum at 505 nm, the absorption spectrum of OCP^O exhibits a progression of partially resolved vibronic transitions due to excited-state stretching displacements of the C–C and C=C bonds of the isoprenoid backbone[61,71] of the bound CAN chromophore in these samples from *Synechocystis* sp. PCC 6803. With illumination, however, the absorption spectrum shifts to longer wavelengths and broadens, largely eliminating any resolution of vibronic peaks. Although the overall absorption maximum of the spectrum shifts only to 520 nm, the 50% absorbance wavelength shifts from 535 nm in OCP^O to 580 nm in OCP^R. The corresponding series of light – dark-adapted difference spectra in Figure 2.2b decrease in intensity in the 470-nm region as the vibronic structure broadens and increases in intensity in the 560-nm region.

Figures 2.2c–2.2f show time courses of the relative yield of the photoactivated OCP^R state, as determined from the integral of the absolute value of the light – dark difference spectrum. This approach would be appropriate if the photoactivation mechanism involves a direct conversion from

OCP^O to OCP^R. Figure 2.2c indicates that the rate of change of the yield slows with increasing illumination time; similar trends were reported by Niziński et al.[68] using single-wavelength absorption traces. The decreasing rate of change accompanies the net accumulation of OCP^R at long illumination times. At short illumination times, the detailed views in Figures 2.2e–2.2f show that a period of induction precedes the onset of the maximum rate of change, which is here observed after about 30 s of illumination. At the lowest illumination power (53 μW in Figure 2.2d), two time regions are marked by linear segments at short illumination times to indicate that the initial rate increases as the illumination power increases to approach that reached at longer times. The trace shown in Figure 2.2f (370 μW) is almost linear over the entire 60 s time range. Despite the observation that the absorption spectra exhibit an isosbestic point, where the spectra at all illumination times appear to intersect at 510 nm in Figures 2.2a, this kinetic behavior indicates directly that an intermediate is formed at short illumination times and that conversion of the intermediate to the OCP^R product is also light induced.

The kinetics for the formation and decay of the intermediate during the photoactivation assays can be retrieved using global and target modeling[72] of the time evolution of the absorption spectrum. This approach allows us to model simultaneously the three-dimensional absorption vs. wavelength vs. time response surface. The absorption spectrum observed at any time from the ensemble of OCP molecules in a sample is modeled as the sum of that from each of the population compartments in a kinetic model, which are here treated as distinct chemical species. The total signal from each compartment is computed as the linear combination of the population (fraction of molecules in the ensemble) with the corresponding evolution-associated spectrum, the absorption spectrum of a pure sample of a given kinetic compartment. A preliminary singular-value decomposition (SVD) analysis (Figure 2.4) indicates that there are at least three spectrokinetic species with significant populations in the ensemble of OCP molecules under illumination. Global and target modeling then employed a linear kinetic model with three compartments, $OCP^O \xrightarrow{1/\tau_1} OCP^I \xrightarrow{1/\tau_2} OCP^R$, with the boundary conditions setting the initial dark concentrations of the intermediate OCP^I and the product OCP^R to zero. In order to apply the simplest possible model, we assume here

that OCP^I and OCP^R are dark stable, which is in line with the finding that the rate of dark recovery at 273 K is very slow (Figure 2.3).

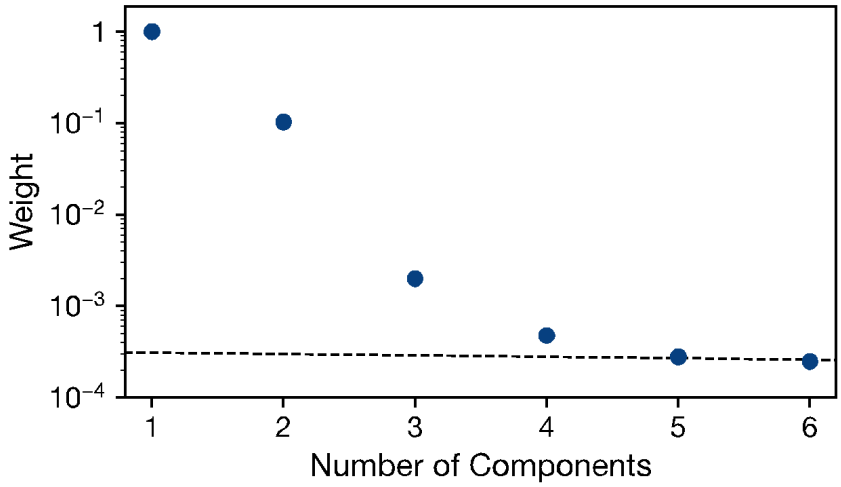

Figure 2.4 Singular-value decomposition (SVD) analysis of the time evolution of the absorption spectrum of OCP at 273 K in the presence of 60% (v/v) glycerol during continuous 430-nm illumination (275 μW). The dashed line marks the noise level of the data set. Figure reprinted with permission from reference 58. Copyright 2023 Royal Society of Chemistry.

Figure 2.5 summarizes the results of the three-compartment global model for the photoactivation assay carried out with 220 μW illumination. The evolution-associated spectra shown in Figure 2.5a resolve the absorption spectrum of the intermediate, labeled here as OCP^I, which exhibits a partially broadened vibronic structure and a partial red shift relative to those of the absorption spectrum of the product OCP^R. The time constant τ_1 for the formation of OCP^I is about ten times longer than that for its conversion to OCP^R, τ_2, so its presence in the ensemble is most evident at short illumination times. At the end of the 60-min exposure to light, the population ratio of OCP^R to OCP^O is about 5:1, and OCP^I is present with perhaps an order of magnitude smaller proportion. The need for OCP^I in the global model is made apparent, however, by a comparison with the results of a direct, two-compartment global model, $OCP^O \xrightarrow{1/\tau_1} OCP^R$ (Figure 2.6). The residuals (data – model) for this model exhibit systematic oscillatory trends, with large deviations from zero noted especially at short illumination times. In contrast, the residuals shown in Figure 2.5c,d for

the three-compartment model including OCP^I are flat and not significantly different from zero for the entire illumination period.

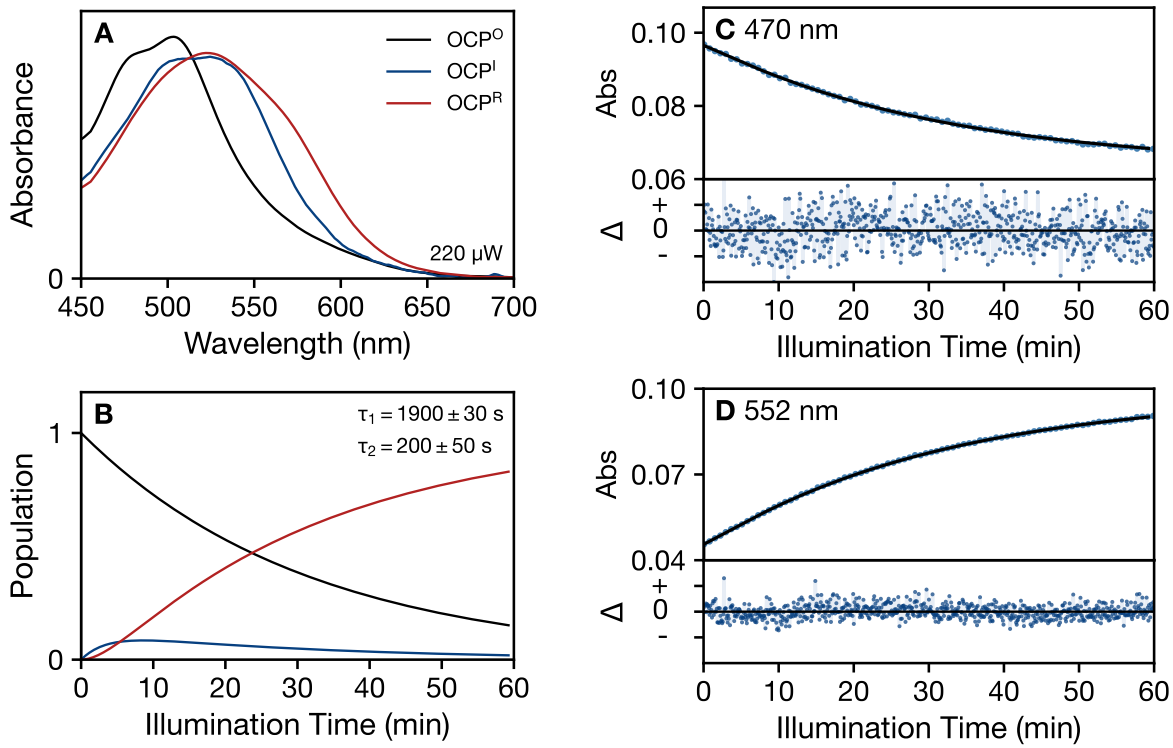

Figure 2.5 Global modeling of the time evolution of the absorption spectrum of OCP at 273 K under continuous 430-nm illumination (220 μW), applying a three-compartment kinetic model: $OCP^O \xrightarrow{1/\tau_1} OCP^I \xrightarrow{1/\tau_2} OCP^R$. (a) Evolution-associated absorption spectra for the three kinetic compartments: dark-adapted OCP^O reactant (black), the OCP^I intermediate (blue), and the final OCP^R product (red). (b) Time evolution of the populations for the OCP^O, OCP^I, and OCP^R kinetic compartments. (c, d) Fit of the global model (black) to the observed absorption (blue dots) at two detection wavelengths, 470 nm and 552 nm, as marked in Figure 2.2a and b, showing the single-wavelength absorption transients (top panel) and residuals (bottom panel). The residuals (Δ = data - global model) are shown with a 20× zoom factor for the absorbance ordinate. Figure reprinted with permission from reference 58. Copyright 2023 Royal Society of Chemistry.

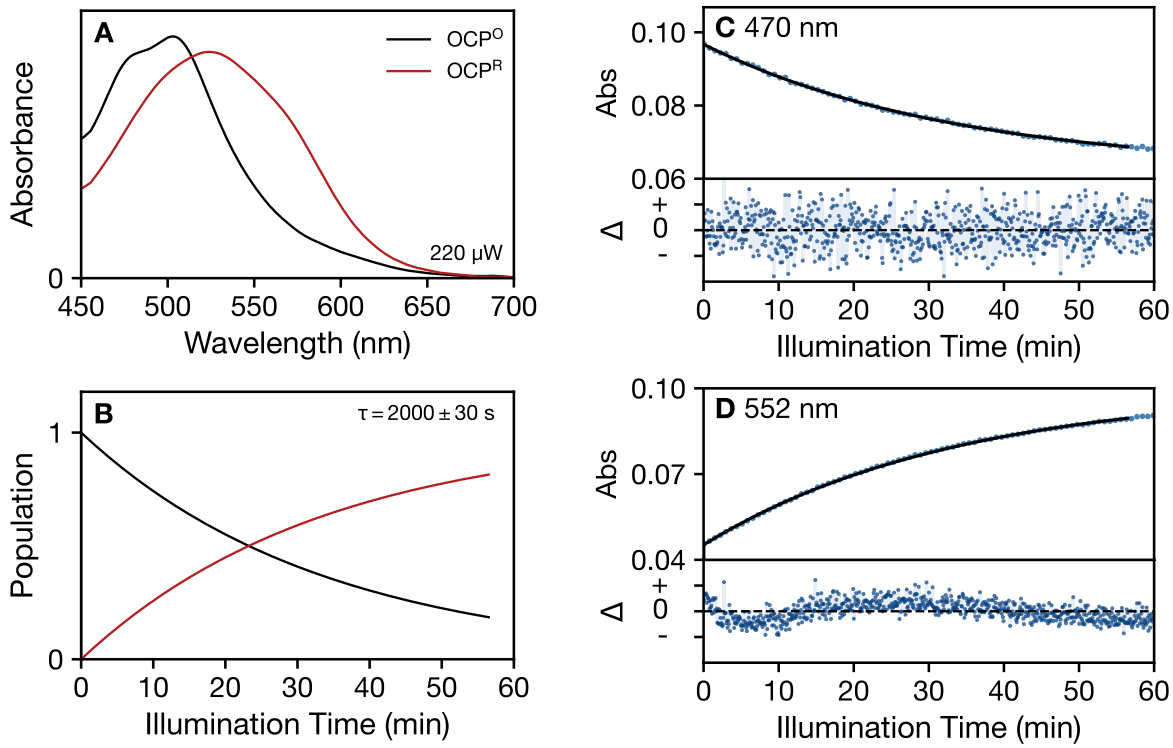

Figure 2.6 Global modeling of the time evolution of the absorption spectrum of OCP at 273 K in the presence of 60% (v/v) glycerol under continuous 430-nm illumination (220 µW), applying a two-compartment kinetic model: $\mathrm{OCP^O} \xrightarrow{1/\tau_1} \mathrm{OCP^R}$. (a) Evolution-associated absorption spectra for the two kinetic compartments: dark-adapted $\mathrm{OCP^O}$ reactant (black) and the final $\mathrm{OCP^R}$ product (red). (b) Time evolution of the populations for the $\mathrm{OCP^O}$ and $\mathrm{OCP^R}$ kinetic compartments. (c, d) Fit of the global model (black) to the observed absorption (blue dots) at two detection wavelengths, 470 nm and 552 nm, as marked in Figure 2.2a and b, showing the single-wavelength absorption transients (top panel) and residuals (bottom panel). The residuals (Δ = data - global model) are shown with a 20× zoom factor for the absorbance ordinate. Figure reprinted with permission from reference 58. Copyright 2023 Royal Society of Chemistry.

2.4.2 Intensity Dependence of Intermediate Formation

The time constants τ_1 and τ_2 exhibit a linear dependence on the power of the excitation light beam, at least under the low intensity conditions where $\mathrm{OCP^I}$ can be resolved with global modeling. The linear plots shown in Figure 2.7 of the rates $1/\tau$ as a function of illumination power retrieve estimates for the intrinsic rate constants k_1 and k_2 from the slopes and for the zero-intensity rate constants k_{01} and k_{02} from the y-intercepts. The y-intercepts are nonzero due to the use of the continuous white-light measurement beam to measure the photoactivation reaction's progress. The

possibility that the rate constants k_1 and k_2 depend on the wavelength of incident light could be addressed in future work to obtain additional information on how each step in the mechanism is triggered by the ketocarotenoid photochemistry.

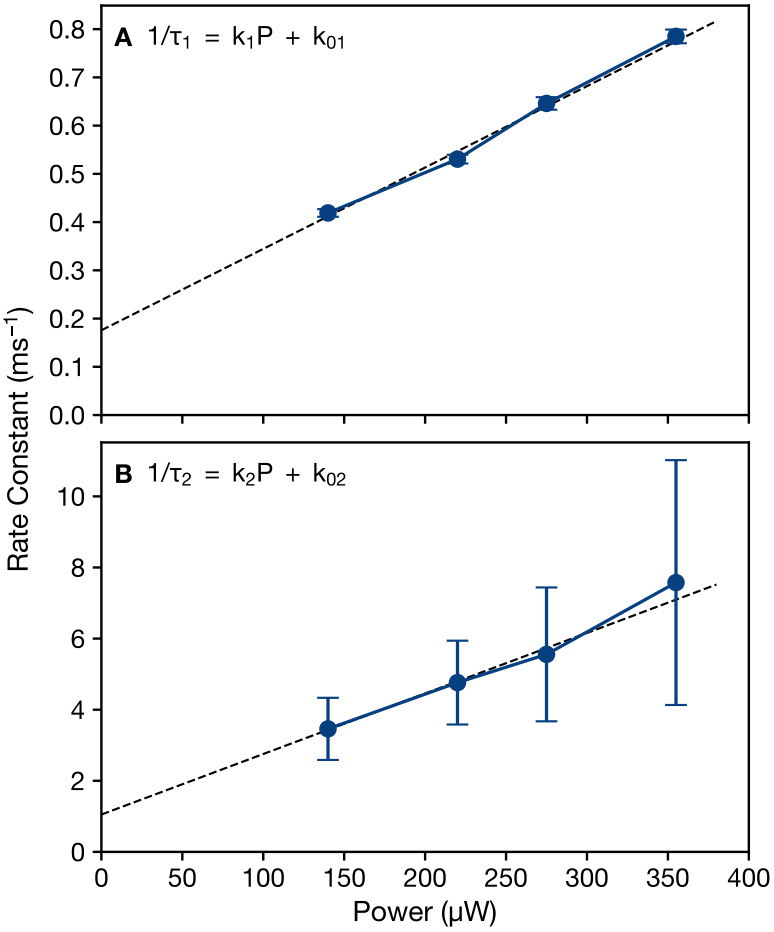

Figure 2.7 Dependence of the photoactivation rate constants observed at 273 K in the presence of 60% (v/v) glycerol on the incident total power of the 430-nm excitation beam for (a) $OCP^O \xrightarrow{1/\tau_1} OCP^I$ and (b) $OCP^I \xrightarrow{1/\tau_2} OCP^R$, as determined by two-step global models. The error bars show the 95% confidence limits for the measured rates at a given illumination power. The dashed lines are least-squares fits to the linear model $1/\tau = kP + k_0$, where k is the rate constant, P is the illumination power, and k_0 is the rate due to the white-light probe beam alone. For (a), k_1=0.00169±6.9x10^{-5} ms^{-1} μW^{-1} and k_{01}=0.176±0.016 ms^{-1}. For (b), k_2=0.0170±0.011 ms^{-1} μW^{-1} and k_{02}=1.05±2.16 ms^{-1}. Figure reprinted with permission from reference 58. Copyright 2023 Royal Society of Chemistry.

The dark recovery following illumination of OCP^R also follows a two-step mechanism, $OCP^R \xrightarrow{1/\tau_{-2}} OCP^{I'} \xrightarrow{1/\tau_{-1}} OCP^O$, with the prime used here in the label $OCP^{I'}$ for the

intermediate to distinguish it formally from the OCP^I intermediate present during illumination for the forward reaction. The spectral evolution shown in Figures 2.5a,b for the set of time-resolved absorption spectra recorded at 293 K in the dark following 30 min of illumination resembles the reverse of that shown in Figures 2.2ab for an OCP sample under illumination. The vibronic structure in the 450–500-nm region of the spectrum recovers and the broad, red-shifted region over the 510–600-nm range decreases as the OCP^O state is formed. SVD analysis of the set of time-resolved spectra (Figure 2.9) supports the conclusion that a kinetic intermediate is present during the nearly three-hour recovery back to the dark-stable OCP^O state. In support of this conclusion, a global model for the direct recovery from OCP^R to OCP^O omitting an intermediate (Figure 2.11) exhibits residuals with systematic deviations, indicating a poor fit to the overall spectral response.

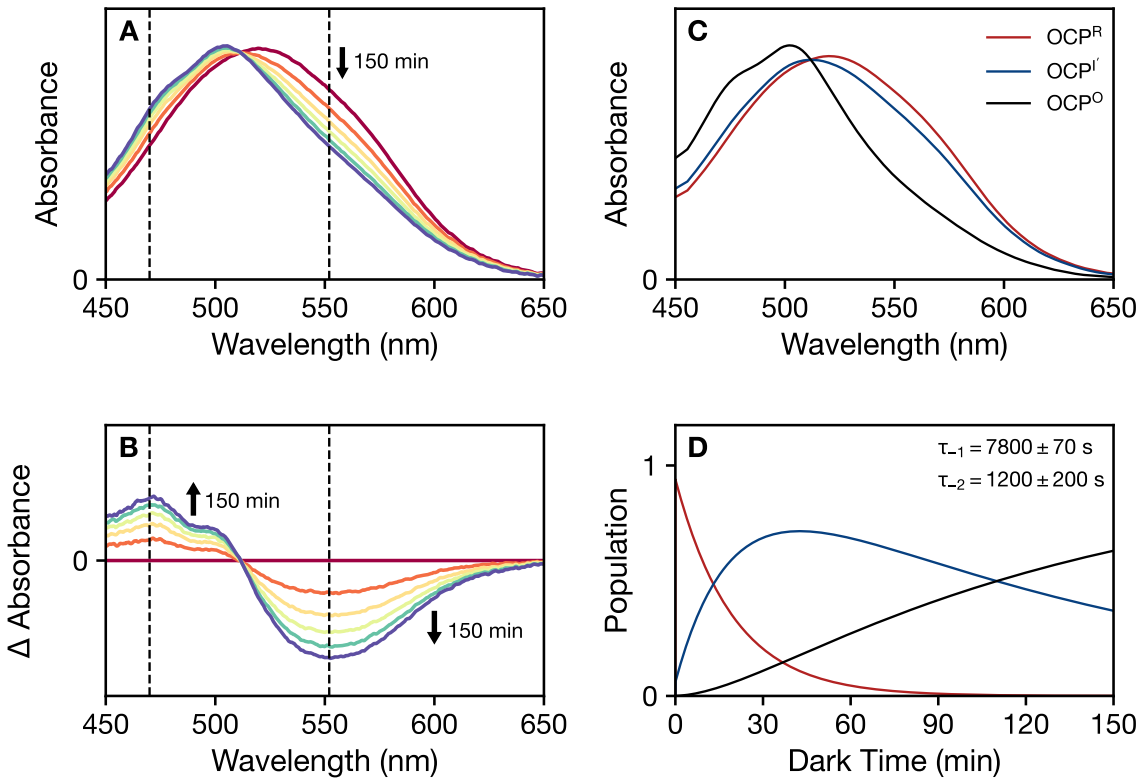

Figure 2.8 Dark recovery of photoactivated OCP at 293 K in the presence of 60% (v/v) glycerol following continuous 430-nm illumination (275 µW) for 30 min. (a) Time evolution of the absorption spectrum from zero dark time (red) to 150 min of darkness (purple), with intermediate spectra spaced by 30 min of darkness. (b) Difference absorption spectra (increasing dark time - initial spectrum after illumination) for the set of spectra shown in panel (a). (c, d) Evolution-associated spectra and populations for a two-step kinetic model: $\mathrm{OCP^R} \xrightarrow{1/\tau_{-2}} \mathrm{OCP^{I'}} \xrightarrow{1/\tau_{-1}} \mathrm{OCP^O}$. Figures 2.11 and 2.10, respectively, show the fitted transients and residuals for the one-step and two-step global models, respectively. Panel (d) indicates the initial populations (boundary conditions) for the dark recovery, which were determined from a global model for the forward, photoactivation response. The rates and the associated populations have not been compensated for the forward rates due to the white light measurement beam. Figure reprinted with permission from reference 58. Copyright 2023 Royal Society of Chemistry.

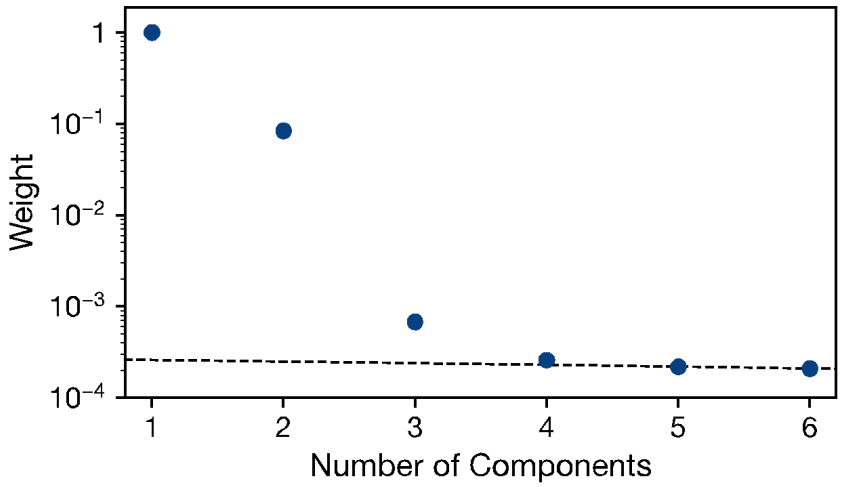

Figure 2.9 Singular-value decomposition (SVD) analysis of the time evolution of the absorption spectrum of OCP at 293 K in the presence of 60% (v/v) glycerol in the dark following continuous 430-nm illumination (275 µW). The dashed line marks the noise level of the data set. Figure reprinted with permission from reference 58. Copyright 2023 Royal Society of Chemistry.

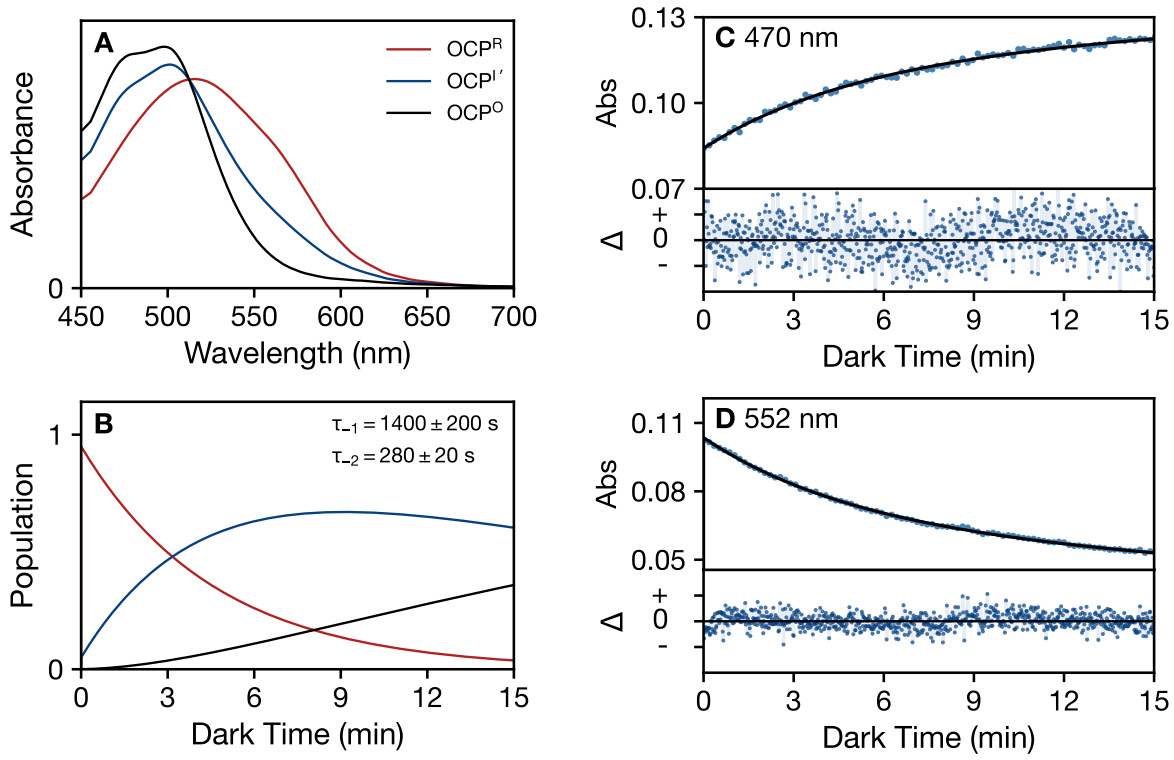

Figure 2.10 Global modeling of the time evolution of the absorption spectrum of OCP at 293 K in the dark in the presence of 60% (v/v) glycerol following continuous 430-nm illumination (275 μW), applying a three-compartment kinetic model: $OCP^{R} \xrightarrow{1/\tau_{-2}} OCP^{I'} \xrightarrow{1/\tau_{-1}} OCP^{O}$. (a) Evolution-associated absorption spectra for the three kinetic compartments: OCP^{R} reactant (red), the $OCP^{I'}$ intermediate (blue), and the final OCP^{O} product (black). (b) Time evolution of the populations for the OCP^{R}, $OCP^{I'}$, and OCP^{O} kinetic compartments; the initial mixture of $OCP^{R}(0) = 0.94$, $OCP^{I}(0) = 0.06$, and $OCP^{O} = 0.00$ was determined from modeling of the prior photoactivation response. (c, d) Fit of the global model (black) to the observed absorption (blue dots) at two detection wavelengths, 470 nm and 552 nm, showing the single-wavelength absorption transients (top panel) and residuals (bottom panel). The residuals (Δ = data - global model fit) are shown with a 20× zoom factor for the absorbance ordinate. Figure reprinted with permission from reference 58. Copyright 2023 Royal Society of Chemistry.

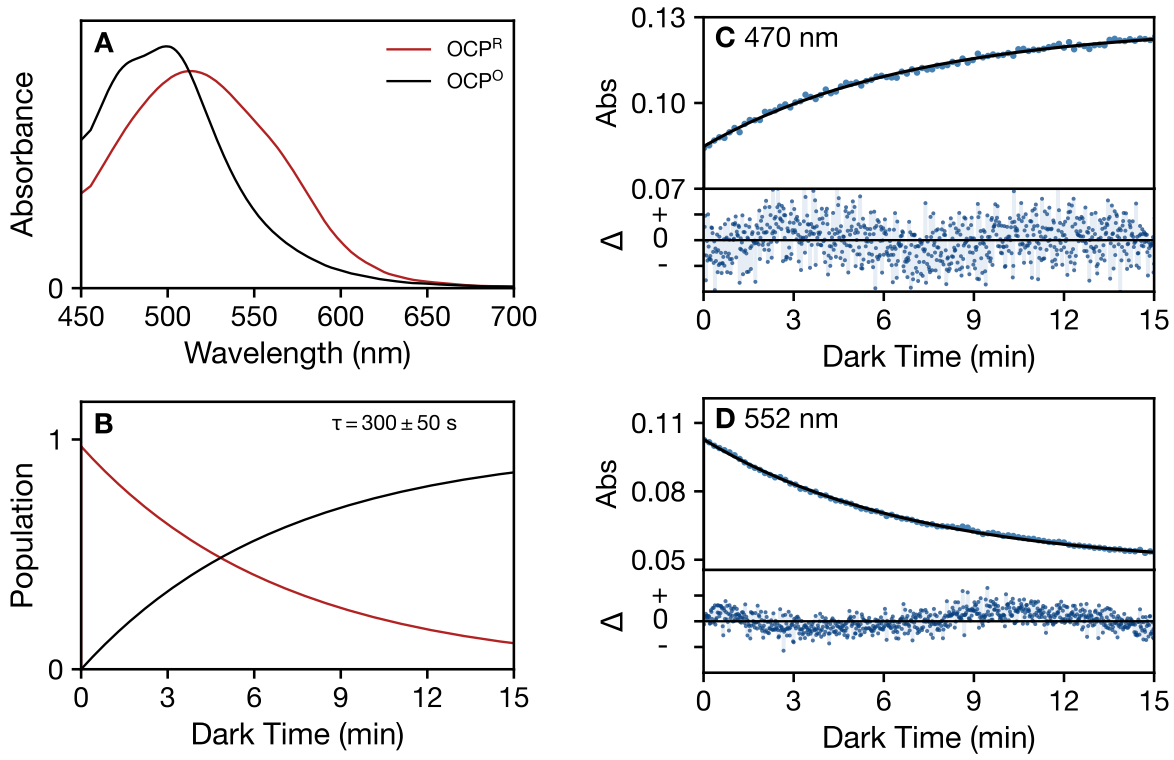

Figure 2.11 Global modeling of the time evolution of the absorption spectrum of OCP at 293 K in the presence of 60% (*v*/*v*) glycerol in the dark following continuous 430-nm illumination (275 μW), applying a two-compartment kinetic model: $OCP^R \xrightarrow{1/\tau_{-1}} OCP^R$. (a) Evolution-associated absorption spectra for the two kinetic compartments: OCP^R reactant (red) and the OCP^O product (black). (b) Time evolution of the populations for the OCP^R and OCP^O kinetic compartments; the initial mixture of $OCP^R(0)$ = 0.95 and OCP^O=0.05 was determined from modeling of the prior photoactivation response. (c, d) Fit of the global model (black) to the observed absorption (blue dots) at two detection wavelengths, 470 nm and 552 nm, showing the single-wavelength absorption transients (top panel) and residuals (bottom panel). The residuals (Δ = data - global model fit) are shown with a 10× zoom factor for the absorbance ordinate. Figure reprinted with permission from reference 58. Copyright 2023 Royal Society of Chemistry.

The two-step global model reported in Figure 2.10 returns estimates for the time constants τ_{-1} and τ_{-2} for the dark recovery of 7800 s and 1200 s, respectively, at 293 K in the presence of 60% (*v*/*v*) glycerol. These time constants are not compensated for the forward rate due to the continuous white-light probe beam, but it is clear that the intermediate $OCP^{I'}$ is metastable at physiological temperatures. It persists in the dark for certainly an hour, whereas OCP^R back-reacts to form OCP^I several times faster. Maksimov et al.[69] previously observed a biexponential kinetic response during the dark recovery of OCP preparations from *Arthrospira maxima*, which they attributed

to the presence of the sub-populations of OCP^R from isoforms containing 3'-hydroxyechinenone and echinenone. The results shown here also evidence a biexponential response, but the global model supports the conclusion that it arises from the sequential kinetics of the populations from OCP^R and $OCP^{I'}$. Recall that we are using here preparations of OCP expressed in *E. coli.* using the gene from *Synechocystis* sp. PCC 6803 along with that only for biosynthesis of CAN, so only the single type of ketocarotenoid is present. Further, modeling of the photoactivation and dark recovery responses with parallel one-step global models not including an intermediate proves to be inadequate especially at short illumination times, even though these models are parametrically overdetermined compared to the three-compartment, two-step global models discussed above.

2.4.3 Effects of temperature and glycerol

As noted above, our choice to characterize initially the photoactivation of OCP at 273 K was intended to suppress as much as possible the rate of the dark-recovery reaction, which simplifies the global model and allows the cleanest isolation of the absorption spectrum of the OCP^I intermediate. Inclusion of 60% (*v*/*v*) glycerol as a cryoprotectant further ensured that the samples remained liquid and bubble free at temperatures over the 220–300 K range while being stirred continuously during a photoactivation experiment.

We performed additional experiments at 293 K to test the relevance of the intermediates OCP^I and $OCP^{I'}$ in the two-step photoactivation and dark recovery models under physiological conditions. Figure 2.12 shows that OCP^I is required to model the photoactivation response of OCP at 293 K in the absence of glycerol, where a nearly complete conversion to OCP^R can be obtained in only a few minutes of illumination. With 545 μW illumination at 430 nm, the forward progress to OCP^R is perhaps ~50× faster than the rate of the dark recovery. The evolution associated spectrum of OCP^I is red shifted and exhibits an intermediate degree of line broadening compared to that of dark adapted OCP^O, but it is not quite as red shifted as that observed at 273 K in the presence of glycerol.

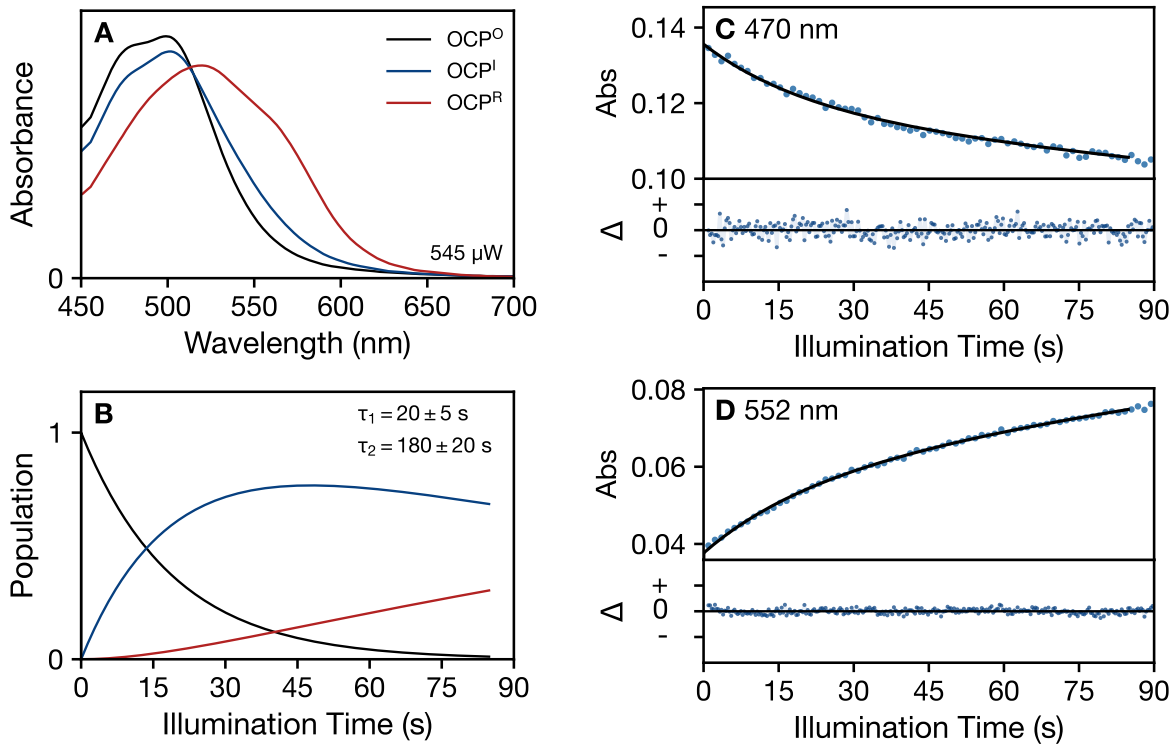

Figure 2.12 Global modeling of the time evolution of the absorption spectrum of OCP at 293 K in the absence of glycerol under continuous 430-nm illumination (545 µW), applying a three-compartment kinetic model: $OCP^O \xrightarrow{1/\tau_1} OCP^I \xrightarrow{1/\tau_2} OCP^R$. (a) Evolution-associated absorption spectra for the three kinetic compartments: dark-adapted OCP^O reactant (black), the OCP^I intermediate (blue), and the final OCP^R product (red). (b) Time evolution of the populations for the OCP^O, OCP^I, and OCP^R kinetic compartments. (c, d) Fit of the global model (black) to the observed absorption (blue dots) at two detection wavelengths, 470 nm and 552 nm, showing the single-wavelength absorption transients (top panel) and residuals (bottom panel). The residuals (Δ = data - global model) are shown with a 20× zoom factor for the absorbance ordinate. Figure reprinted with permission from reference 58. Copyright 2023 Royal Society of Chemistry.

The summary of results provided in Table 2.1 indicate that increasing the temperature from 273 K to 293 K and/or removing the glycerol cryoprotectant markedly increases the rates of the photoactivation and dark-recovery processes. The SVD analysis and global models for the dark recovery at 293 K in the absence of glycerol and for photoactivation at 293 K in the presence of glycerol. Under all of the conditions studied, a two-step global model with an intermediate was required to obtain an adequate description of the photoactivation and dark recovery responses. The first step of the photoactivation reaction and both steps of the dark recovery reaction at 293 K are

slowed by factors of 3 and 5, respectively, by the addition of glycerol. In contrast, the rate of the second step of the photoactivation mechanism, from OCP^I to OCP^R, is enhanced in the presence of glycerol by a factor of three. These findings suggest that the rates of the molecular mechanisms of the two steps are oppositely affected by the exchange of water molecules in the hydration shell with glycerol molecules from the bulk.[73] Further, comparison of the evolution-associated spectra for the photoactivation and dark recovery responses at 293 K and the absence of glycerol suggests that the spectral changes are more reversible than at 273 K in the presence of glycerol. This observation supports the conclusion that the structures of the intermediates OCP^I and $OCP^{I'}$ are equivalent.

Table 2.1 Rates for photoactivation and dark recovery of OCP at 273 K and 293 K determined by global modeling of the absorption spectrum with a two-state model

T (K)	Glycerol %	k_1 (ms^{-1} μW^{-1})	k_2 (ms^{-1} μW^{-1})	k_{-1} (ms^{-1})	k_{-2} (ms^{-1})
273 K	60	$0.00169 \pm 6.9 \times 10^{-5}$	$0.017 \pm 1.1 \times 10^{-2}$	~0	~0
293 K	60	$0.00333 \pm 6.2 \times 10^{-5}$	$0.030 \pm 5.0 \times 10^{-3}$	0.128 ± 0.0012	0.833 ± 0.14
293 K	<0.3	$0.0917 \pm 2.3 \times 10^{-2}$	$0.010 \pm 1.1 \times 10^{-3}$	0.714 ± 0.010	3.57 ± 0.26

2.4.4 Molecularity of the dark recovery

The three-compartment global models treat both steps of the photoactivation and dark recovery reactions as unimolecular reactions with first-order kinetic responses. Zhang et al[56] had concluded previously on the basis of mass spectrometric evidence, however, that OCP^O is a dimer aggregate and that photoactivation yields OCP^R monomers. The results presented so far show that the two steps in the photoactivation and dark recovery are well described by reversible first-order processes with respect to the concentration of CAN, as detected in terms of its absorption spectrum, but conversion of the monomer to the dimer of OCP during one of the steps in the dark recovery would be bimolecular and second-order with respect to the protein concentration. We can identify which of the two steps is bimolecular by determining the concentration dependence of the rate constants obtained by the global models for the dark-recovery reaction. To carry this out, we performed a

series of dark recovery experiments at 293 K in the absence of glycerol over a range of dilutions of the stock OCP^O solution. In each experiment, the sample was first illuminated for 30 min at 430 nm to generate the OCP^R photoproduct. The initial concentrations of the three OCP species for the subsequent dark recovery were obtained from the populations determined by a global model for the forward photoactivation response.

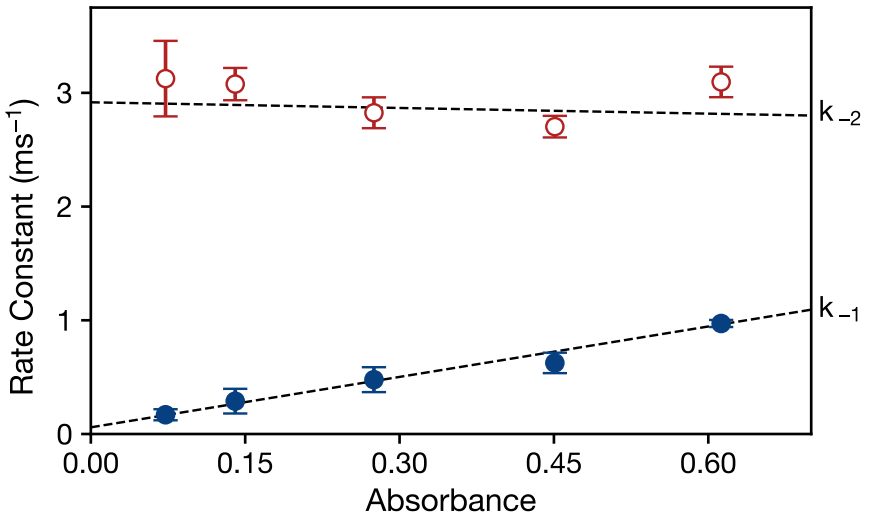

Figure 2.13 Concentration dependence of the first-order rate constants determined by global modeling of the dark recovery of OCP at 293 K in the absence of glycerol following illumination at 430 nm. The absorption (A) of the dark adapted OCP^O sample was measured at 500 nm prior to exposing the sample to light. The dashed lines show fitted linear models: k_1 = (1.48 ± 0.10) × A + (0.060 ± 0.050) ms^{-1}, and k_2 = (-0.17 ± 0.36) × A + (2.95 ± 0.15) ms^{-1}. Figure reprinted with permission from reference 58. Copyright 2023 Royal Society of Chemistry.

Figure 2.13 shows that the rate constant k_{-2} measured at 293 K in the absence of glycerol for the dark recovery from OCP^R to $OCP^{I'}$ is independent of the concentration of OCP, which confirms that this step of the mechanism is unimolecular, involving a reorganization of the structure of OCP^R to obtain the $OCP^{I'}$ intermediate. In contrast, the rate constant k_{-1} for the conversion of $OCP^{I'}$ to OCP^O is linearly dependent on the OCP concentration. These results prove that the conversion of $OCP^{I'}$ to OCP^R is a bimolecular reaction, combining two monomeric proteins to yield a dimer aggregate in the OCP^O state. In the simplest picture, the OCP^I and $OCP^{I'}$ intermediates correspond to two OCP^O monomers. The dark recovery mechanism, $2\,OCP^R \xrightarrow{1/\tau_{-2}} 2\,OCP^O \xrightarrow{1/\tau_{-1}} (OCP^O)_2$, exhibits first-order kinetics in the global models because each of the kinetic compartments

contains two CAN chromophores, each of which contributes identical absorption spectra. The forward photoactivation process would be the reverse of the dark recovery, $(OCP^O)_2 \xrightarrow{1/\tau_1}$ $2\,OCP^O \xrightarrow{1/\tau_2} 2\,OCP^R$, but the linear illumination power dependences (Figure 2.7) indicate that photoexcitation of only one of the two CAN chromophores in the OCP^O dimer is required to drive the photodissociation reaction yielding the two OCP^O monomers, which are then converted independently upon absorption of a second photon.

2.4.5 Absorption spectral line shapes

A structural interpretation of the finding that the evolution associated spectrum from OCP^I is broadened and red shifted compared to that of the resting OCP^O state is aided by numerical simulations of the absorption spectra of CAN using the multimode Brownian oscillator (MBO) model.[74] We discussed this theory previously in our analyses of the absorption and fluorescence spectra from carotenoids in solution and in the OCP.[2,75,76] In the MBO model, the reorganization energy, λ,[77] controls the broadening of the vibronic transitions due to the fluctuating electrostatic interactions of the chromophore with groups in the surrounding protein and aqueous medium.

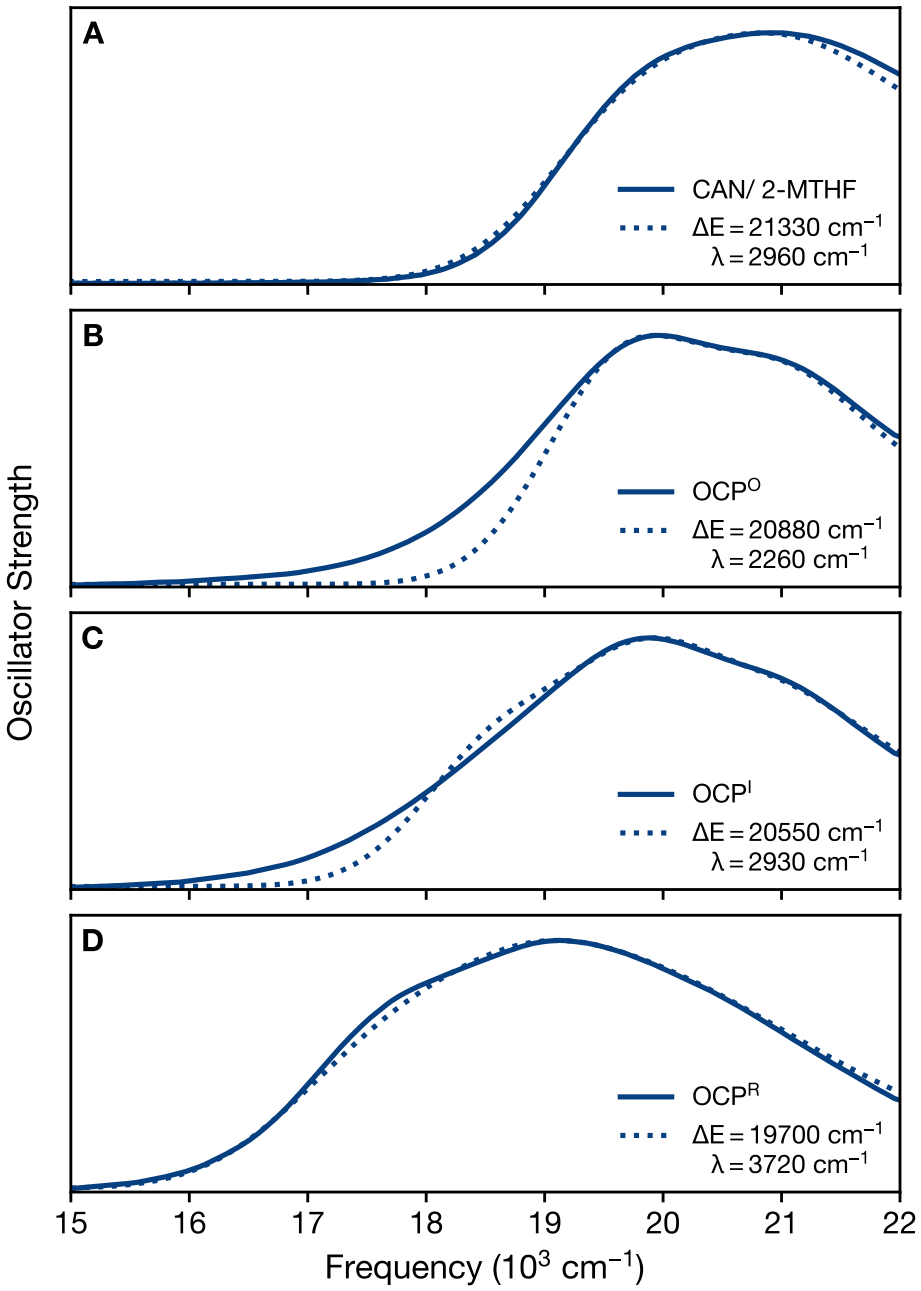

Figure 2.14 Numerical simulations (dotted spectra) using the multimode Brownian oscillator (MBO) model of the experimental absorption oscillator strength spectra (solid spectra) for (a) canthaxanthin (CAN) in 2-methyltetrahydrofuran solvent and (b-d) of the evolution-associated spectra for the components in the three-component, forward photoactivation global model at 293 K in the absence of glycerol (Figure 2.12). The absorption spectra are plotted here as the oscillator strength, $\epsilon(\nu)^3/\nu$, where ϵ gives the absorbance and ν stands for the frequency. The MBO model parameters for each of the simulated spectra are listed in Table 2.2. The legends for panels (a-d) give the values for the vertical ground-to-excited-state energy gap, E, and the reorganization energy, λ, in wavenumbers (cm^{-1}). Figure reprinted with permission from reference 58. Copyright 2023 Royal Society of Chemistry.

As an example, the MBO model fits the absorption spectrum of CAN in 2-methyltetrahydrofuran (Figure 2.14) very well except at the shortest wavelengths. The lack of any resolved vibronic structure is consistent with solvation of CAN in a polar solvent, which results in a fairly large value for λ. In comparison, the partial resolution of the vibronic structure in the OCP^O spectrum (Figure 2.14b) corresponds to a lower value for λ, which is consistent with CAN being largely protected from the surrounding water by the surrounding protein structure. The increasing values for λ and the shifting of the ground-to-excited-state energy gap to lower energies then required to fit the vibronic structure and the degree of red shifting in the spectra for OCP^I (Figure 2.14c) and OCP^R (Figure 2.14d) indicate that the CAN chromophore is more exposed to the surrounding water as the photoactivation reaction proceeds, especially for the OCP^I-to-OCP^R step in the mechanism. As the vibronic structure broadens, the MBO models provide a much better fit to the low-frequency onset of the absorption spectrum, which has been discussed in terms of an inhomogeneous distribution of CAN conformations.[78,79]

.

Table 2.2 Multimode Brownian oscillator (MBO) model parameters[a,b] for the simulated absorption spectra of canthaxanthin (CAN) in 2-methyltetrahydrofuran and for the forward photoactivation mechanism of OCP (Figure 2.14)

Species	ω_{eg}	G	E_1	E_2	ν_1	ν_2	λ
CAN/2-MTHF	21330	400	600	400	810	750	2960
OCP^O	20880	350	200	500	480	730	2260
OCP^I	20550	260	320	400	1350	600	2930
OCP^R	19700	90	750	800	880	1200	3720

a. See Gurchiek et al[42] for an explanation of the parameters and of the associated theory. As in that work, the MBO model used here incorporates an inertial solvation mode (G), two diffusive solvation modes (E_1 and E_2), and two underdamped vibrational modes of the CAN chromophore (the C–C stretching mode, 1=1150 cm^{-1} and the C=C stretching mode, 2=1550 cm^{-1}). *b.* All parameters have units of wavenumbers (cm^{-1}). The eg values are for the vertical $S_0 \rightarrow S_2$ energy gap for CAN's absorption transition, but the remaining parameters are for the reorganization energies for the given mode. The total of the reorganization energies is in the λ column.

2.4.6 Effects of actinic light wavelength

Previous studies of OCP photoactivation cite blue-green light as the driving force for photoactivation of OCP^O to OCP^R, with the most detailed approximation for the OCP action spectrum originating in Rakhimberdieva et al.[4] which produced an action spectrum matching the absorbance spectrum of the carotenoid bound within OCP. To investigate the photophysical mechanism that causes carotenoid distortions leading to photoactivation of the protein, the rates of photoactivation of the protein dimer and monomers were measured in the manner previously described, with photolysis wavelengths ranging from 430 nm to 700 nm and held at consistent light intensity of approximately 250 μW.

Measurements of the photoactivation spectrum were taken using the protocol established by Rakhimberdieva.[4] The results were successfully reproduced by correcting the raw rate of photoactivation by the intensity of photolysis light, as executed in their work (Fig 2.15). This was achieved even when employing global modeling software to obtain the photoactivation rates rather than relying on measurements from the overall change in the spectrum. However, this calculation fails to consider the probability of an actinic photon being absorbed by the protein, which excites the bound carotenoid and triggers the protein response. To understand the per-photon rate of photoactivation as a function of wavelength, which is necessary to understand the photophysical mechanism that causes carotenoid distortion, the rates of photoactivation were further corrected by accounting for by dividing the intensity-corrected rate, k, by the absorbance oscillator strength for the ground state molecule, f_{OCP}.

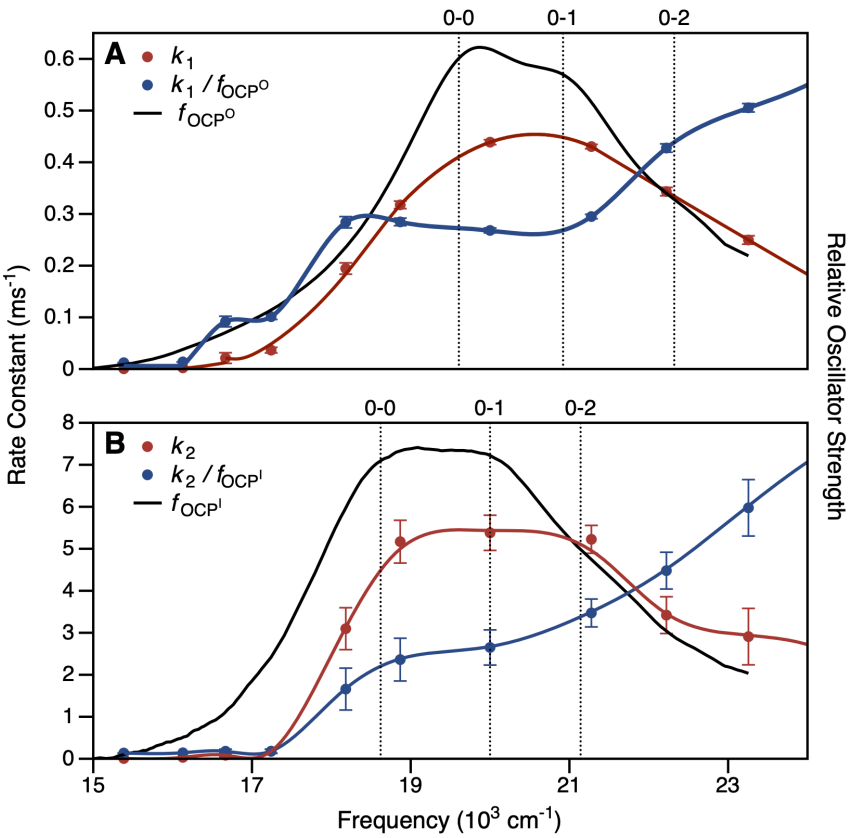

Figure 2.15 Photoactivation assays of dark-adapted OCP at 273 K under continuous illumination with varying wavelengths of actinic light. (a) Photoactivation of OCP^O to OCP^I, representing photolysis of the protein dimer to a monomer. The raw rates of photoactivation (k_1, red markers) are imposed on the oscillator strength absorbance spectrum of OCP^O (f_{OCP^O}, black line). The blue markers show the corrected rate of photoactivation (k_1 / f_{OCP^O}), which accounts for the probability of actinic photon absorbance at the excitation wavelength. (B) Photoactivation of OCP^I to OCP^R, representing photolysis of the CTD from the OCP^I monomer. The raw rates of photoactivation (k_2, red markers) are imposed on the oscillator strength absorbance spectrum of OCP^I (f_{OCP^I}, black line). The blue markers show the corrected rate of photoactivation (k_2 / f_{OCP^I}), which accounts for the probability of actinic photon absorbance at the excitation wavelength. The vertical dashed lines shown mark the positions of the 0-0, 0-1, and 0-2 vibronic transitions.

For both the photoactivation of the OCP^O dimer and the OCP^I monomer, the resulting per-photon rate of photoactivation departs from an action spectrum that matches the absorbance of the carotenoid, instead illustrating increased photoactivation for higher-energy actinic wavelengths. Additionally, the corrected photoactivation rate retains the vibronic character of the absorption spectrum, a feature not previously observed in any photosynthetic system to the author's knowledge.

2.5 Discussion

The main finding of this study, that photoactivation and dark recovery of OCP involve two-step mechanisms mediated by a metastable intermediates, OCP^I and OCP^I, leads to a new hypothesis on the protein structural response in OCP that starts with absorption of light by the bound keto-carotenoid. In short, we suggest that the OCP^O spectrum after dark adaptation arises from the dimer aggregate of OCP^O.[45] This dimer (Figure 2.1) is observed in the crystal structures of the orange form of all the structures of the OCP1 family to date, either in the asymmetric unit (e.g. pdb IDs 3mg1, 5ui2, 5hgr, 7ekr, 7qd1) or via crystallographic symmetry (e.g. pdb IDs 4xb5, 6pq1). The amount of surface area buried at the dimer interface (~1100 $Å^2$) suggests that the dimer is a biologically relevant form of the OCP^O. Photodissociation of the OCP^O dimer into a monomer is a precondition for the subsequent step of NTD-CTD separation and has been proposed to be a possible mode of OCP regulation.[80] The light-induced intermediate OCP^I is accordingly assigned to the OCP^O monomer. The events associated with translocation of the ketocarotenoid into the NTD and the displacement of the CTD to produce the OCP^R product state[52,53,60,81] would principally follow absorption of light by the OCP^I intermediate. This proposal is prompted by the changes we observe in the resolved vibronic structure of the absorption spectrum of CAN as the metastable intermediate OCP^I forms and as its dark counterpart $OCP^{I'}$ decays. The finding that the addition of 60% (*v*/*v*) glycerol enhances the rate of this step is new information, very likely reporting on how the exposure of the hydrophobic regions of the NTD–CTD interface as the NTD is rotated away controls the rate.

Zhang et al.[56] had concluded previously on the basis of mass spectrometric evidence that OCP^O is a dimer aggregate and that photoactivation produces OCP^R monomers, but the present global model results and the light intensity dependence of the rates for the two steps in the mechanism now reveal that the dissociation step requires absorption of a photon and precedes the light-driven formation of OCP^R. Further, owing to the mixture of OCP^I and OCP^R that persists for a long time during illumination, global modeling is clearly required to isolate the OCP^R

spectrum for further spectroscopic analysis. Similarly, the global model for the dark recovery from OCP^R shows that the $OCP^{I'}$ intermediate is present during most of the measured response but anticipates that the OCP^O dimer will be exclusively present after prolonged dark adaptation. Šlouf et al.[59] attributed the absorption spectra observed in their OCP preparations to two dark monomeric variants of OCP^O, a main form and a red-shifted form that may correspond to OCP^I. Maksimov et al.[69] also considered the possibility that the OCP dimer and monomer would account for their observations of a biexponential absorption response during dark recovery from OCP^R. In a subsequent paper, Maksimov et al.[82] observed using fluorescence anisotropy measurements that the effective hydrodynamic radius of their tetramethylrhodamine-labeled OCP preparations increased substantially when the ketocarotenoid is photoexcited, as would be expected for the OCP^I-to-OCP^R step in the mechanism. This result is consistent with the very low protein concentrations used in the fluorescence experiments, which would favor the monomeric OCP^I intermediate.

The requirement that OCP absorb two photons sequentially via a metastable intermediate to reach the product OCP^R state may be unique in photobiology. The light-intensity dependence of the forward photoactivation process (Figure 2.7) indicates that each of the two steps involves absorption of a single photon of light by the CAN chromophore. Owing to the use of very low light intensities to drive the forward reaction and the long lifetime of the intermediate $OCP^{I'}$ in the dark, we know that the CAN chromophore has relaxed nonradiatively to its ground electronic state, S_0, prior to the second photon's excitation of the OCP^I intermediate. Comparison of the evolution-associated spectra from the forward and reverse global models indicates that the light-induced and dark recovery reactions are effectively reversible. A subsequent study designed to avoid continuous exposure of the sample to a white-light probe beam during dark recovery would be required to determine whether or not the OCP^I and $OCP^{I'}$ intermediates have different structures.

An additional clue to the nature of the mechanisms here is that the $OCP^{I'}$ intermediate is a kinetically stable enough molecule to survive for more than an hour in the dark at 293 K. This finding assuredly limits us to consider only protein-derived structural changes during the conversion from OCP^O to OCP^I. In comparison, Niziński et al.[68] reported that an intermediate in the photoactivation

reaction was observed with a ~0.1-s lifetime following absorption of a single laser pulse by their OCP^O samples. Given the rate at which the absorption spectra were recorded in this study, we would not expect to be able to detect any ground-state photophysical intermediates from CAN with lifetimes in the dark of less than a few seconds.

The structure of the homodimer of OCP^O (Figure 2.1c) provides a starting point for a discussion of the partial red shift and the somewhat reduced resolution of vibronic structure associated with formation of the OCP^I intermediate. Molecular dynamics (MD) simulations indicate that the solvent accessible surface area (SASA) of CAN is larger in the OCP^O monomer than in the OCP^O dimer (Figure 2.16). This implies that absorption spectrum of CAN in the monomer would exhibit a modest red shift and broadening of the vibronic structure, respectively, from that of the dimer. This effect would arise from an overall change in polarity of the surroundings and an increase in λ due to a stronger interaction with the electrostatic fluctuations in the surroundings. The large surface cavity leading to the ketocarotenoid-binding cleft is not fully protected from the surrounding solvent upon formation of the OCP dimer.[45] However, metadynamics simulations by Sharawy et al.[83] have revealed a thermally accessible local minimum in the OCP^O monomer characterized by the detachment of the αA helix in the N-terminal extension (NTE, Figure 2.1ac) from the CTD domain. Several of the NTE residues (D6, R9, G10, P13, N14, T15, L16) are involved in the dimer interface. This finding suggests that the monomer might undergo additional fluctuations compared to the dimer, where detachment of the αA helix is hindered. The SASA distribution observed in the MD simulations at 300 K is about ten percent broader for the monomer than the dimer.

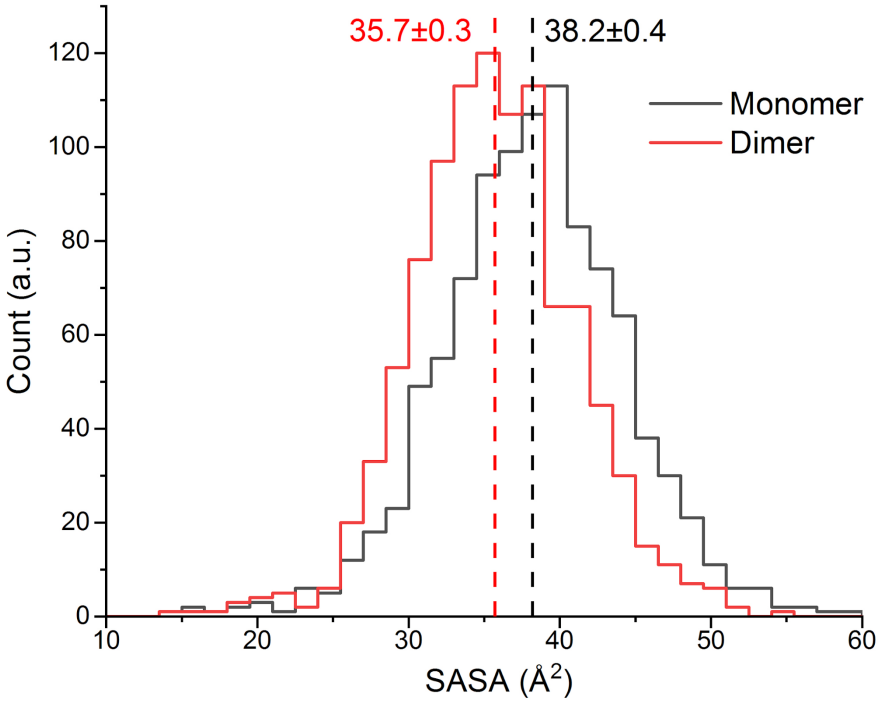

Figure 2.16 Distribution of the solvent accessible surface area (SASA) for the canthaxanthin chromophore in the OCP^O monomer (black) and dimer (red) structures from molecular dynamics (MD) trajectories at 300 K. The dotted vertical lines mark the average values, which are labeled with 95% confidence intervals due to the standard deviation of the mean for the 1000 samples in the MD trajectory. The distributions are characterized by the standard deviations 5.4 Å^2 for the dimer and 6.0 Å^2 for the monomer. Figure reprinted with permission from reference 58. Copyright 2023 Royal Society of Chemistry.

Given that hydrogen bonds and salt bridges between the NTDs of the two monomers stabilize the dimer assembly, it is intriguing to suggest that similar photophysical responses by the bound ketocarotenoid are responsible for the triggering of both steps of the forward photoactivation mechanism. As noted in the Introduction, the current perspective for the photoactivation of the OCP^O monomer is that absorption of light by the ketocarotenoid is followed by nonradiative decay processes leading to the breaking of the hydrogen-bonding interactions between the β_1-ionone ring of the ketocarotenoid with the surrounding binding site in the CTD, which would initiate the translocation of the ketocarotenoid (Figure 2.1ab). Photodissociation of the dimer would be a low-probability event, given that only one of the two ketocarotenoids in a given complex would be triggered by absorption of a photon, but light-induced conformational changes of one of the NTDs due to the photophysics of its associated ketocarotenoid might well destabilize the dimer assembly

enough to favor its dissociation. The analysis by Pigni et al.[81] of the intermediate states along the translocation of the ketocarotenoid in the photoactivation mechanism using QM/MM calculations further suggests that the partially red-shifted absorption spectrum of OCP^{I} may require at least a partial translocation of the ketocarotenoid. Given this suggestion, one should consider the possibility that the OCP^{I} and $OCP^{I'}$ spectra report the contributions of more than one intermediate state[60,81] in the translocation of the ketocarotenoid.

The blue photolysis light bias and vibronic features of the photoactivation action spectrum accounting for absorption probability (Fig 2.15), show that the dynamics of the excited state carotenoid, other than vibrations along the carotenoid's isoprenoid backbone, significantly affect the rate at which hydrogen bonds with the protein residue are broken, leading to carotenoid reorganization and separation of the protein domains. Following the promotion of an electron from a pi bonding to a pi star antibonding orbital, the conjugated polyenes that compose the isoprenoid backbone undergo bond length alternation and vibrations along the range of conjugation. If vibrations along the isoprenoid backbone were a sufficient mechanism to cause photoactivation of the protein, one would not expect to observe the blue photolysis light bias of the action spectrum for producing OCP photoproducts at higher rates. Therefore, the increased rate of photoactivation with higher energy actinic light suggests that an additional mechanism of carotenoid distortion accounts for the necessary perturbations of hydrogen bonds that lead to photoactivation. Exciting the carotenoid with energies sufficient to populate higher vibrational energy levels stores additional potential energy within the carotenoid, as evidenced by the apparent vibronic structure of the action spectrum. The increased potential energy may be used to cross energy barriers, granting access modes of carotenoid distortion other than in-plane vibrations. Further research into the dynamics of the carotenoid in its excited state may uncover the movements related to breaking hydrogen bonds within the protein, ultimately leading to photoactivation.

Chapter 3: Fluorescence anisotropy of carotenoids in solution and bound within the Orange Carotenoid Protein

3.1 Summary

Carotenoids are usually only weakly fluorescent despite being very strong absorbers in the mid visible because their first two excited singlet states, S_1 and S_2, have very short lifetimes. In order to probe the structural mechanisms that promote nonradiative decay of the S_2 state to the S_1 state, we have carried out a series of fluorescence lineshape and anisotropy measurements with carotenoids in solution and when bound within the Orange Carotenoid Protein. The anisotropy values observed in the fluorescence emission bands originating from the S_2 and S_1 states reveal that large internal rotations of the emission transition dipole moment, as much as 50° relative to that of the absorption transition dipole moment, are initiated during ultrafast evolution on the S_2 state potential energy surface and persist upon nonradiative decay to the S_1 state. Electronic structure calculations of the orientation of the transition dipole moment account for the anisotropy results in terms of torsional and pyramidal distortions near the center of the isoprenoid backbone. The excitation wavelength dependence of the fluorescence anisotropy indicates that these out-of-plane conformational motions are initiated by passage over a low activation energy barrier from the Franck–Condon S_2 structure. This conclusion is consistent with detection over the 77–200 K range of a broad, red-shifted fluorescence band from a dynamic intermediate evolving on a steep gradient of the S_2 state potential energy surface after crossing the activation barrier. The temperature dependence of the oscillator strength and anisotropy indicate that nonadiabatic passage from S_2 through a conical intersection seam to S_1 is promoted by out-of-plane motions of the isoprenoid backbone with strong hindrance by solvent friction.

Sections of material in this chapter have been published in another form: Gurchiek, J. K.; Rose, J. B.; Guberman-Pfeffer, M. J.; Tilluck, R. W.; Ghosh, S.; Gascón, J. A.; Beck, W. F. Fluorescence Anisotropy Detection of Barrier Crossing and Ultrafast Conformational Dynamics in the S_2 State of β-Carotene. *J. Phys. Chem. B* **2020,** 124, 9029–9046, DOI: 10.1021/acs.jpcb.0c06961.

These findings indicate definitively that the photoactivation reaction is initiated by conformational motions of the ketocarotenoid inside the OCP structure in the OCP^O state and that these motions are not hindered at cryogenic temperatures. We suggest that these light-driven motions of the ketocarotenoid provide the photophysical trigger for the photoactivation reaction by initiating providing strain and electrostatic driving forces for the displacement of the C-terminal domain.

In cyanobacteria, the orange carotenoid protein (OCP) mediates nonphotochemical quenching of bilin excited states in the phycobilisome. An intrinsic ketocarotenoid serves in OCP as an ambient light-intensity sensor by triggering the conversion of the resting, orange form (OCP^O) to the active, red form (OCP^R), which can then bind to the phycobilisome's core. We have performed fluorescence anisotropy measurements over the 77–293 K temperature range to determine the conformational motions of the ketocarotenoid canthaxanthin (CAN) that initiate the photoactivation response. The results reveal that even at cryogenic temperatures, CAN undergoes twisting and bending displacements of a C=C bond near the middle of the isoprenoid backbone during the nonradiative decay pathway from the optically prepared S_2 state via the Sx intermediate to the dark S_1 state. The anisotropy values are consistent with preparation of a pyramidal structure with significant delocalized intramolecular charge-transfer character near a seam of conical intersections with the S_1 state. At low temperatures in 2-MTHF solution, however, the frozen solvent cavity restricts the motions of CAN in the S_2 and Sx states to volume-conserving, concerted motions of more than one C=C bond, such as those of the "hula-twist" structure.

3.2 Introduction

Carotenoids perform essential roles in light harvesting and photoprotection in photosynthetic organisms.[16,84] These functions arise principally from the properties of the two lowest energy excited singlet states, the S_1 and S_2 states.[20,61,84,85] The S_2 state is optically populated by $\pi \rightarrow \pi^*$ transitions in the strong, mid-visible absorption band, which gives solutions of the carotenoids a characteristic yellow or orange color. In condensed phases and in the binding sites of proteins, the S_2 state decays usually in < 200 fs after absorption of light. Such short lifetimes, on the order of the mid-frequency

vibrations of the isoprenoid backbone (Scheme 2), suggest that passage to the S_1 state is mediated by a nonadiabatic mechanism,[86,87] involving strong coupling of the nonradiative electronic transitions to vibrational motions. The fluorescence quantum yield is ~10^{-6},[88] much smaller than that of many other $\pi \rightarrow \pi^*$ chromophores. Unusually for the lowest singlet excited states of $\pi \rightarrow \pi^*$ chromophores because it violates Kasha's rule,[89] fluorescence from the S_1 state of carotenoids is weaker than that from S_2 or not observed[90,91] despite the S_1 state's having a much longer lifetime, usually in the ~10 ps range.[90,91]

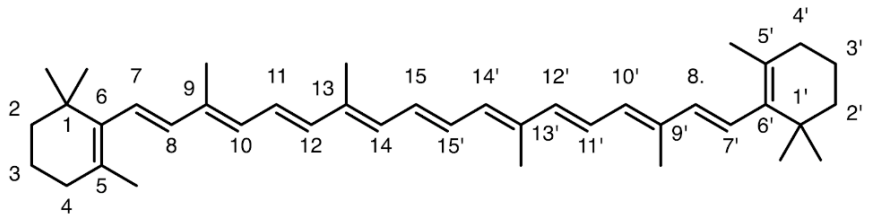

Scheme 2: Structure of β-carotene with β-ionone and isoprenoid carbons labeled.

The distinct spectroscopic properties of the S_1 and S_2 states in all–*trans* polyenes and carotenoids are usually rationalized in terms of the selection rules for optical transitions for planar structures belonging to the C_{2h} point group.[84] The S_0 and S_2 states are assigned the A_g and B_u characters, respectively, so one-photon electric-dipole transitions between them are fully allowed. The S_1 state is assigned the A_g character, however, so absorption and fluorescence transitions between it and the S_0 state are forbidden by the Laporte rule.[92,93] This scheme is consistent with the finding by Holtom and McClain[94] that the S_1 state of polyenes can be populated from the S_0 state by two-photon optical transitions.[92,93]

Nonradiative decay of the S_2 state to the S_1 state of carotenoids has been mainly attributed to activity in the resonance Raman-active C–C and C=C bond-stretching normal coordinates of the isoprenoid backbone. Displacements along these coordinates results in a partial inversion of the carbon–carbon bond-length alternation (BLA) pattern along the isoprenoid backbone upon optical preparation of the S_2 state and gives rise to a vibronic progression in the ground-state absorption spectrum.[61,84,91,95] Relaxation from S_2 to S_1 would involve passage through a conical

intersection (CI)[96,97] after a significant displacement from the photoexcited Franck–Condon S_2 structure along the BLA coordinates.[96,97] Because the C_{2h} symmetry would be maintained if only the BLA coordinates are involved, nonradiative decay from S_2 to S_1 would account for quenching of the fluorescence due to the symmetry selection rules. The S_1 state is readily detected in carotenoids, however, by virtue of its strong excited-state absorption (ESA) transitions in the 500–600 nm region, which populate a range of higher energy singlet excited states S_n with B_u character.[98,99]

The S_1 state is nevertheless spectroscopically dark when carotenoids assume asymmetric conformations with symmetries lower than C_{2h}. The ground electronic state, S_0, often favors nonplanar structures in solution; steric clashing of methyl substituents with the adjacent isoprenoid backbone results in canting out-of-plane of the β-ionone (cyclohexene) rings of β-carotene and related carotenoids and an overall sigmoidal distortion along the length of the intervening isoprenoid backbone.[22,100–102] Further, direct one-photon optical preparation of the S_1 state of carotenoids is not observed even when relief from the symmetry selection rules would be expected, such as in structures lacking an inversion center owing to asymmetric substitution,,[99] *cis* stereochemistry,[103] or nonlinear configurations.[104] Overall, these findings raise the argument that the distinct spectroscopic and dynamical properties of the S_1 and S_2 states in carotenoids arise from the underlying details of their electronic structures[105] and from the Franck–Condon overlaps of their potential energy surfaces with the ground state,[104] not as much from simple selection rules determined by symmetry or pseudoparity. The electronic character and the energy ordering[27] of the lowest singlet states of even the shortest polyenes remains controversial because of their considerable theoretical complexity, requiring multireference calculations to approach chemical accuracy in computational studies.[28–30] The use of multireference calculations to characterize the doubly excited character of the S_1 excited states of carotenoids has been noted in recent work by Mennucci and coworkers.[31,32] Because the carotenoids are large molecules, their potential energy surfaces and CIs have not yet been determined by accurate quantum chemical calculations.

As a further indication of the complexity of the electronic structures of carotenoids, studies of their photophysical properties persistently include mention of several additional dark electronic

states at energies adjacent to the S_2 and S_1 states.[61,84] Resonance Raman excitation profiles[34] and time-resolved spectroscopy with broadband, femtosecond pulses[36,106–108] have implicated one of these dark states, S_x, in mediating nonradiative transfer of population from the S_2 state to the S_1 state. There are two current proposals for the nature of the S_x state.[61,85] The first assigns the S_x state to a discrete singlet excited state with an energy lying below that of the bright S_2 state.[106] In the scheme introduced by Tavan and Schulten,[109] this state would have a B_u character in the C_{2h} point group.

An alternative recent proposal is that the S_x state is actually a dynamic intermediate moving on the S_2 state surface along out-of-plane vibrational coordinates of the isoprenoid backbone.[85] This hypothesis accounts for several key aspects of the femtosecond time evolution of the ESA signals from β-carotene observed by Cerullo et al.[106] and of the heterodyne transient grating signals from β-carotene and the ketocarotenoid peridinin observed in our laboratory.[75,76] As sketched in Scheme 3 in terms of schematic potential energy surfaces, an initial excursion along the BLA coordinates after absorption of a photon would drive the molecule in less than a vibrational period to the vicinity of a low activation energy barrier, which divides the regions of the S_2 potential energy surface for planar and out-of-plane distorted conformations. Crossing the barrier leads to a steep potential energy gradient with respect to torsional and/or pyramidal coordinates of the isoprenoid backbone.[75,76,85,110] The presence of the barrier was initially suggested[85] in analogy to that determined by electronic structure calculations of the potential energy surfaces for the $\pi \rightarrow \pi^*$ excited states of models for retinal protonated Schiff bases (PSBs) and of medium-conjugation length cyanines.[111] Qualitatively, the barrier height would be expected to increase with longer polyenes because the π^* character per bond would accordingly decrease; for ethene, the potential energy surface is barrierless.[112]

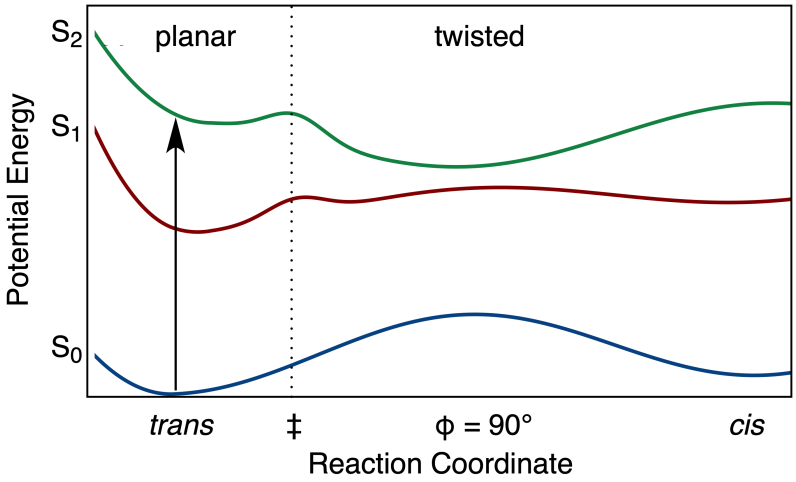

Scheme 3: Schematic potential energy curves[75,85,113] proposed for the singlet excited states of all-trans-β-carotene, as plotted with respect to a reaction coordinate for the structural response following optical preparation of the S_2 state. An activation-energy barrier (‡) divides planar (BLA coordinates) and out-of-plane distorted (torsional and/or pyramidal coordinates, ϕ) regions of the potential energy surfaces. The S_2 and S_1 surfaces strongly interact at a CI seam near the S_2 minimum with respect to the ϕ coordinates. Figure reprinted with permission from reference 42. Copyright 2020 American Chemical Society.

Following the barrier, the proposed S_2 and S_1 potential curves are depicted as converging along the out-of-plane coordinates at a seam of CIs,[27,97] where the two states are expected to be strongly mixed. Rather than the harmonic single-coordinate picture discussed in previous work, then, the photophysics of carotenoids is discussed in this hypothesis in terms of anharmonic multicoordinate dynamics. The shape of the S_1 potential energy curve suggested in Scheme 3 follows the main features of that proposed by de Weerd et al.[113] in a discussion of their femtosecond pump–continuum probe results, but we have added a low barrier at the onset of torsions corresponding to that proposed for the S_2 state. Because the S_1 state has a doubly excited character, corresponding to two spin-coupled triplet excitations,[27] the barrier height would be expected to be lower than that of the S_2 state, which is a singly excited state. The de Weerd et al. results suggest that the S_1 state should exhibit a global minimum near the planar, all-*trans* structure. Accordingly, crossing from the S_2 state to the S_1 state near the CI seam would usually be followed by conformational relaxation back to the planar structure. This aspect is consistent with the recent suggestion by Wei et al.[105] that the S_1 state of carotenoids should be conformationally stiffer (*e.g.*, favoring planar structures) than the

S_2 state. In a minor fraction of photoexcitations, of course, this scheme anticipates that relaxation from the CI would occur to the *cis* configuration on the S_0 surface after internal conversion from the S_1 state. We need to reiterate, however, that these aspects of the S_2 and S_1 potentials are merely hypotheses that are consistent with some, but not necessarily all, of the currently available experimental information.

S_x is detected in heterodyne transient grating spectra as a dynamic intermediate, following the decay of the stimulated emission (SE) from the Franck–Condon S_2 state and prior to the rise of the strong ESA from the S_1 state.[75] For peridinin, we found that the lifetime of S_x in a range of solvents exhibits a power law dependence with respect to the viscosity or the polar solvation time of the solvent. This behavior indicates that radiationless decay from the S_x intermediate on the S_2 surface to the S_1 state is promoted by large-amplitude out-of-plane distortions of the isoprenoid backbone, with the polar solvation dependence implicating formation of an intramolecular charge-transfer (ICT) character.[110] The changes in electronic structure that accompany twisting and pyramidal distortions of a isoprenoid backbone have been extensively discussed by Bonačić-Koutecký et al.[114–116] In peridinin, the electron-withdrawing tendency of the carbonyl substituent on the γ-lactone ring in conjugation with the isoprenoid backbone would be expected to enhance the ICT character significantly, which would increase the solvent friction for the motions that promote decay to the S_1 state. This proposal accounts for the observation that the lifetime of the S_x state of peridinin is substantially longer than that of β-carotene, which lacks a carbonyl substituent.[110]

An important implication of the assignment of S_x to a dynamic intermediate in the S_2 state is that the spontaneous fluorescence and SE signals should evolve rapidly to longer wavelengths, well into the near-IR, as molecules descend along the out-of-plane potential energy gradient. The femtosecond pump–probe experiments and global target modeling by de Weerd et al.[113] suggested this possibility for β-carotene early on. The SE from the S_2 state is red shifted from the ground-state bleaching signal at short time delays following photoexcitation, but at longer time delays it is partially obscured by a much stronger ESA band at longer wavelengths. This time evolution to the red was interpreted in terms of progress along a torsional potential energy gradient, which would

narrow the energy gap between the S_2 and S_1 surfaces as they converge at a CI. In recent work, Liebel et al.[117] used femtosecond transient absorption spectroscopy to observe in β-carotene that passage through the CI between the S_2 and S_1 states occurs with retention of vibrational coherence in modes that lack resonance Raman activity. In Scheme 3, the out-of-plane coordinates lack resonance Raman activity because the gradient is accessed only after a significant displacement with respect to the BLA coordinates.

In the present study, we report a test of this picture for the light-induced dynamics in carotenoids using the continuous-wave line shape, quantum yield, and anisotropy of the fluorescence emission from carotenoids in several aprotic solvents. Emission from molecules moving on a gradient on the S_2 potential energy surface with respect to out-of-plane coordinates after passage over a low activation energy barrier gives rise to a broad fluorescence spectrum with a low anisotropy, with the anisotropy decreasing as the excitation source is scanned to the blue over the vibronic structure of the absorption spectrum from the 0–0 region. A weaker fluorescence spectrum with partially resolved vibronic structure arising from the S_1 state is detected in the near-IR, and it also exhibits a strong intensity dependence on the excitation wavelength. The minimum fluorescence anisotropy detected at long emission wavelengths is consistent with a large internal rotation of the emission transition dipole moment (TDM), as much as 50° in nonpolar solvents. Because the TDM is aligned within a few degrees of the molecular frame of the isoprenoid backbone in all-*trans* polyenes,[118–120] these results indicate directly that β-carotene undergoes large-amplitude out-of-plane conformational motions as nonradiative decay from the S_2 state to the S_1 state occurs. This picture is further supported by studies of the fluorescence emission at low temperatures, which show that it is possible to observe stronger emission from a dynamic intermediate evolving on the S_2 state that may correspond to S_x or to its precursor from the photoexcited, Franck–Condon structure. Companion electronic structure calculations are then used to determine how the permanent dipole moment and the rotation of the emission TDM are induced by torsional and pyramidal distortions of the isoprenoid backbone. These calculations suggest that the fluorescence anisotropy results

are consistent with a zwitterionic structure with a pyramidal conformation in the center of the isoprenoid backbone.

3.3 Experimental and Computational

3.3.1 Sample Handling for Fluorescence Spectroscopy

β-carotene purchased from Sigma/Aldrich (C9750-5G) was purified by Amy LaFountain in the Frank laboratory at the University of Connecticut by high-performance liquid chromatography (HPLC) on a Waters 600E/600S multisolvent delivery system equipped with a 2996 photodiode array detector, which has been described previously.[121,122] For the present samples, the separation employed a Waters Atlantis Prep T3 OBD 5 µm column (19 x 100 mm). Acetonitrile was delivered isocratically at a flow rate of 7.0 mL/min. All-*trans*-β-carotene fractions collected from the HPLC were dried under nitrogen gas and stored in a freezer at -70°C in darkness until required for experiments.

β-carotene was removed from freezer storage and dissolved in one of the four solvents to obtain an absorbance of 0.2 at 460 nm with a 1 cm optical path length. The four solvents, chloroform (Sigma/Aldrich 372978), carbon disulfide (Sigma/Aldrich 335266), *n*-Hexane (EMD HX0295-6), and 2-methyltetrahydrofuran (Sigma/Aldrich 414247), were used as received from freshly opened bottles. Each sample was centrifuged at 17000 x *g* prior to recording fluorescence spectra to pellet undissolved, light-scattering particles. Samples of beta-carotene were held in 1 cm fused-silica cuvettes either in a Quantum Northwest Peltier-effect temperature controller or in a Janis liquid nitrogen cryostat.

Samples of canthaxanthin (Sigma/Aldrich 11775) and used without further treatment. Fresh bottles of 2-methyltetrahydrofuran (Sigma/Aldrich 414247) were used for each series of experiments to reduce the likelihood of solvent contamination due to peroxide formation or other environmental factors. Absorbance spectra of canthaxanthin in 2-MTHF were measured prior to every experiment to ensure consistent sample concentrations and qualitative appearance prior to experiment. Fol-

lowing fluorescence experiments, the absorbance spectra of canthaxanthin samples were measured to check for impurities that may have occurred during an experiment, such as exposure to vacuum grease, but no such cases of sample contamination were observed. Samples of OCP binding canthaxanthin were grown and provided by the Kerfeld research group as detailed in Chapter 2.

Samples of CAN in 2-MTHF were measured in a 1 cm fused-silica cuvette, while spectra from OCP in glycerol/buffer solution were measured in a 1 cm plastic cuvette due to its better resilience against cracking at extremely low temperatures.

3.3.2 Linear Absorption Spectra

Absorption spectra were acquired at room temperature (23°C) with a Shimadzu UV-2600 spectrophotometer with a spectral bandpass of 2 nm.

In variable temperature work, beta-carotene absorption spectra were acquired with the sample *in situ* in a Janis liquid nitrogen cryostat or a Peltier cuvette temperature controller (Quantum Northwest) before and after fluorescence measurements. The canathaxanthin and OCP samples were acquire *in situ* in an Oxford Instruments OptistatDN liquid nitrogen cryostat. The absorption measurements were carried out using a home-built, fiber optic absorption spectrometer. The light source was an Ocean Optics DH-2000 deuterium/quartz halogen fiber illuminator. Ocean Optics QP400-1-UV-VIS fiber optic cables were used with fiber collimators before and after the sample. The transmitted light was detected by an Ocean Optics USB4000 spectrograph/CCD detector. LabVIEW (National Instruments) programs were used to acquire blank and sample transmission spectra using this apparatus and then to calculate the absorption spectrum.

3.3.3 Fluorescence Spectroscopy

The home-built fluorescence spectrometer used in the current work was also used for the experiments reported previously on the fluorescence of the ketocarotenoids 3'-hydroxyechinenone and canthaxanthin in the orange carotenoid protein.[2] The following specifies improvements to the in-

strument that were made since that work, and specific details are provided about the polarization optics and the methods used for measurement of the fluorescence anisotropy spectra.

A schematic diagram of the fluorescence spectrometer is provided as Figure 3.1. Excitation light was obtained from a Thorlabs MNWHL4 broadband LED and a Spectral Products CM112 double monochromator operated in an additive configuration. The monochromator was equipped with 1200 gr/mm gratings blazed at 500 nm (Spectral Products AG1200-00500-303) and entrance and intermediate slits selected to obtain a spectral bandpass of 2 nm (100 cm^{-1} at 430 nm, 80 cm^{-1} at 500 nm). A Thorlabs SH1 shutter was placed between the LED and monochromator to turn on and off the excitation beam. The monochromatic excitation light selected by the double monochromator was routed to the sample cuvette by fused silica plano-convex collimating and focusing lenses. A Glan-Thompson calcite polarizer (10 mm aperture, Newport) was placed in the collimated excitation beam between the two lenses and manually rotated to set the linear plane of polarization vertically, as outlined below. As an example, the average power delivered to the sample was 5.86 μW at 460 nm, as measured by a Newport model 818-SL silicon photodiode detector and a model 835 picowatt optical power meter.

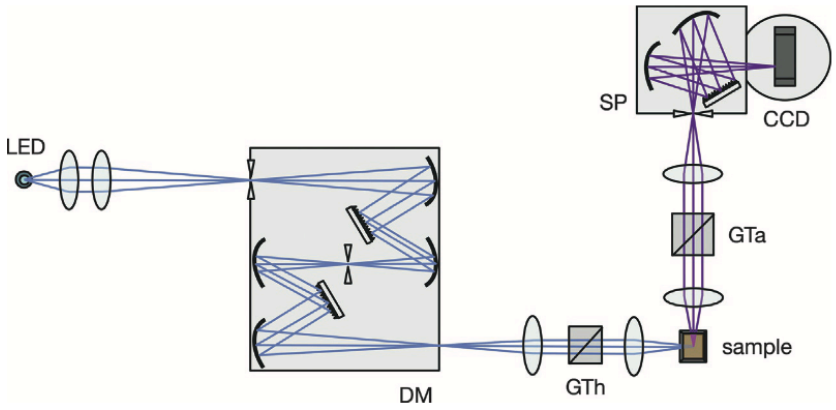

Figure 3.1 Schematic diagram of the home-built fluorescence spectrometer used in the present work. Symbols: DM, double monochromator; GTh, Glan-Thompson polarizer; GTa, Glan-Taylor polarizer; SP, grating spectrograph. Figure reprinted with permission from reference 42. Copyright 2020 American Chemical Society.

For experiments at 298 K, the sample cuvette (fused silica, 1 cm path length) was mounted in a Quantum Northwest LUMA 40 Peltier-type cuvette holder, which was controlled by a Quantum Northwest TC 125 temperature controller.

Fluorescence emission and Raman scattering was collected 90° from the excitation beam by a f2 fused-silica spherical lens. The collimated emission beam between was passed through a Glan-Taylor calcite polarizer (20 mm aperture, Melles-Griot). The polarizer was mounted in a Newport 495B-A motorized rotation stage, which was driven by a Newport PMC200-P motion controller. After passage through the Glan Taylor polarizer, the collimated fluorescence beam was focused onto the input slit of an Acton Research SP-150 spectrograph (150 mm focal length) by a second fused-silica spherical lens. The fluorescence emission was dispersed in the spectrograph by a 300 gr/mm diffraction grating (500 nm blaze wavelength). The input slit was adjusted to obtain a spectral bandpass of 4 nm (110 cm^{-1} at 600 nm), as determined by the breadth of Hg emission lines. The grating was turned to image the 423 to 927 nm range of the emission spectrum onto a Princeton Instruments Versarray 1300B CCD detector (back-illuminated sensor chip, liquid nitrogen cooled), which was equipped with a shutter controlled by the Princeton Instruments ST-133 detector controller. The spectrograph and CCD detector were calibrated using an Ocean Optics HG-1 Hg calibration lamp mounted at the sample's position. The wavelength dependence of the sensitivity of the spectrograph and CCD detector was calibrated using the emission spectrum of the quartz halogen lamp in the Ocean Optics DH-2000 fiber illuminator. Data acquisition was controlled using LabVIEW (National Instruments) and Scientific Imaging Toolkit for LabVIEW (R Cubed Software Consultants, LLC) routines, the latter providing subroutines to operate the CCD detector.

For the measurements of canthaxanthin in solution and when bound within OCP, the Princeton Instruments Versarray detector was replaced with an Oxford Instruments Newton 940-BV CCD camera. All canthaxanthin and OCP fluorescence measurements were recorded in an Oxford Instruments OptistatDN sample-in-gas liquid nitrogen cryostat with its temperature controlled by the accompanying MercuryiTC system.

3.3.4 Data Acquisition and Processing

Fluorescence data acquisition was performed by recording dark background (excitation beam shutter closed), magic angle (54.7°), and horizontal (90°) fluorescence emission spectra, with the given angle specifying the orientation of the emission polarizer relative to the vertical excitation polarizer. For each excitation wavelength, four 5-minute exposures of the CCD detector were accumulated sequentially for the dark background, magic angle polarization, and horizontal polarization spectra. This procedure was repeated four times, which obtains a total of 16 five-minute CCD exposures for each type. Accordingly, each data acquisition sequence required 4 hours in total, with the sample repeatedly allowed to recover in the dark for 20 minute periods during the procedure during the acquisition of background spectra. 2.5 minute CCD exposures were employed for the 2-MTHF series over the 77–200 K range owing to the larger quantum yields observed.

The absorption spectrum of the carotenoid samples was measured before and after the fluorescence data acquisition cycle in order to determine if permanent photobleaching occurred or if photoproducts were accumulated. No changes in absorption were detected in any of the samples monitored during these experiments.

After data acquisition using the protocol described above, cosmic ray spikes were removed from the vertically binned emission and dark background spectra by comparing the detected emission intensities of the 16 equivalent CCD exposures to that of the mean on a horizontal pixel-by-pixel (dispersed wavelength) basis. A reading from one of the scans was rejected from the set if its intensity was outside of 0.9 times the standard deviation of the mean. The surviving readings were then averaged. After subtraction of the averaged background spectrum, the magic-angle intensity spectra reported in this paper were then corrected for the wavelength dependence of the emission spectrograph and CCD detector sensitivity using a reference spectrum an Ocean Optics HL-3*plus*-CAL radiometrically calibrated lamp. Intensity correction was not performed when computing the fluorescence anisotropy spectra because the correction factor is canceled out by the anisotropy ratio calculation.

3.3.5 Determination of Fluorescence Anisotropy and Quantum Yield

The fluorescence anisotropy, r, is calculated from the linear polarization emission components detected parallel and perpendicular to the plane of polarization of the excitation light, $F_{\parallel}$ and $F_{\perp}$, as

$$r = \frac{F_{\parallel} - F_{\perp}}{F_{\parallel} + 2F_{\perp}} \tag{1}$$

The anisotropy reports the angle θ between the emission and absorption TDMs, the latter as photoselected from the randomly oriented ground-state ensemble present in solution,[123]

$$r = r_0 P_0(\theta) = r_0(3\cos^2\theta - 1)/2 \tag{2}$$

In this equation, r_0 is for the maximum anisotropy, 0.4, which corresponds to parallel TDM directions for the absorption and emission TDMs, and P_2 is the second Legendre polynomial.

The fluorescence anisotropy spectrum from the β-carotene samples was obtained by measuring the fluorescence emission spectrum with the emission polarizer oriented 90° and at the magic angle, 54.7°, from the vertically oriented excitation polarizer, as described above. This procedure was adopted in lieu of the usual practice of recording 90° and 0° spectra because it obtains anisotropy spectra with an improved signal/noise ratio. Owing to the low fluorescence quantum yield for β-carotene, it was necessary to use long exposures of the CCD detector to obtain good signal/noise ratios. With 0° polarization, however, the length of time that the CCD detector could be exposed is significantly reduced owing to the presence of several relatively intense Raman scattering lines, which are highly polarized.

The calculations used to determine the anisotropy using the 90° and 54.7° spectra is described below. As shown below in Figure S_2, this procedure returns fluorescence anisotropy spectra that are indistinguishable from those conventionally recorded with 0° and 90° spectra with a reference fluorophore, rhodamine 6G.

The equations that follow specify the orientation of the emission and excitation polarizers in the fluorescence spectrometer using subscripts. For example, F_{xy} indicates the fluorescence intensity spectrum recorded as a function of emission wavelength when the excitation polarizer is in the *x* orientation and the emission polarizer is in the *y* orientation. The subscript V indicates that the plane of linear polarization for the polarizer is vertical; H indicates a horizontal polarization, and M indicates orientation at the magic angle, 54.7°.

Using this notation, the total fluorescence emission spectrum, F_T, is obtained as

$$F_T = 2\ G\ F_{VH} + F_{VV} \tag{3}$$

The *G* factor used in equation 1 is determined as the ratio of vertically and horizontally polarized emission spectra from a reference fluorophore, in our case rhodamine 6G in methanol, with horizontally polarized excitation.

$$G = \frac{F_{HV}}{F_{HH}} \tag{4}$$

G is determined by the efficiencies of the diffraction grating and curved mirrors in the emission spectrograph.[123]

The total fluorescence F_T is proportional to the polarized fluorescence intensity measured with the emission polarizer at the magic angle,

$$F_T = C\ F_{VM} \tag{5}$$

Combining equations 3 and 5,

$$F_T = C\ F_{VM} = 2\ G\ F_{VH} + F_{VV} \tag{6}$$

Re-arranging equation 6 obtains two results:

$$C = \frac{2\,G\,F_{VH} + F_{VV}}{F_{VM}} \tag{7}$$

$$F_{VV} = C\,F_{VM} - 2\,G\,F_{VH} \tag{8}$$

The anisotropy spectrum can be calculated from the 90° and magic-angle emission spectra using these results as

$$r = \frac{F_{VV} - G\,F_{VH}}{F_{VV} + 2\,G\,F_{VH}} = \frac{C\,F_{VM} - 2\,GF_{VH} - G\,F_{VH}}{C\,F_{VM} - 2\,G\,F_{VH} + 2\,G\,F_{VH}} = \frac{C\,F_{VM} - 3\,G\,F_{VH}}{C\,F_{VM}} \tag{9}$$

Figure 3.2 shows a determination of the fluorescence anisotropy from a reference chromophore, rhodamine 6G in glycerol, using 90° and magic-angle spectra. The results are not distinguishable from those obtained with 0° and 90° spectra. Also note that the anisotropy is flat all the way across the fluorescence emission spectrum except near the excitation wavelength, where highly polarized scattered light is observed. This response should be compared to the emission fluorescence anisotropy spectra reported in this paper for β-carotene, which often exhibit a pronounced decrease in the near-IR region of the spectrum. The Rhodamine 6G anisotropy spectrum establishes that the low anisotropies determined for β-carotene do not arise from deficiencies in the optics nor from the data acquisition or data processing procedures.

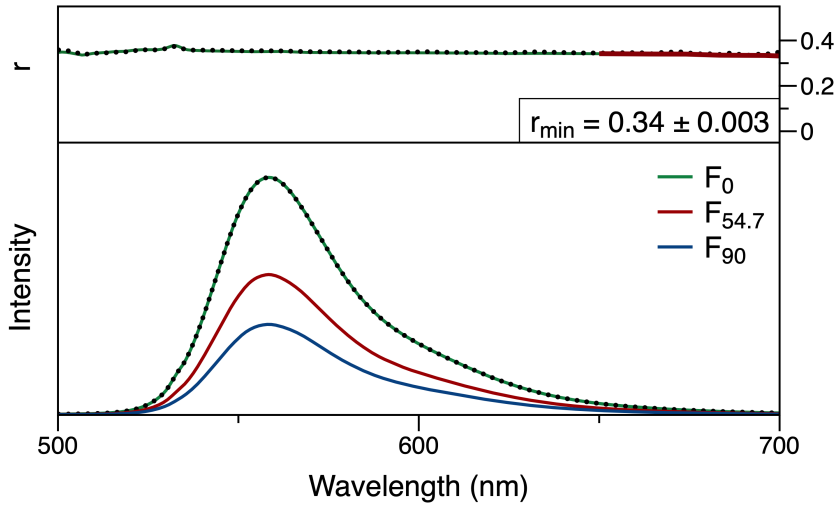

Figure 3.2 Fluorescence emission anisotropy (top panel) and linearly polarized fluorescence emission spectra (bottom panel) from rhodamine 6G in glycerol at 23°C with excitation at 532 nm. The angles indicated for the emission polarizer are with respect to the vertically polarized excitation polarizer. The green anisotropy trace was calculated conventionally using the F_0 and F_{90} spectra. The superimposed dotted anisotropy trace was calculated using the magic angle, $F_{54.7}$, and F_{90} spectra. The red trendline in the >650 nm region of the anisotropy spectrum was used to calculate the minimum anisotropy value, 0.34 ± 0.003. Figure reprinted with permission from reference 42. Copyright 2020 American Chemical Society.

The fluorescence anisotropy reported previously for rhodamine B and rhodamine 101 in glycerol solvent is 0.38-0.39.[124,125] Similarly, the fluorescence anisotropy for rhodamine 6G in glycerol and propane-1,2-diol is 0.37.[126] These values were determined at the peak emission wavelength. The results we obtained for rhodamine 6G are comparable to these published values. Figure S_2 shows that the fluorescence anisotropy for rhodamine 6G is 0.35 at 560 nm and 0.34 as averaged over the >650 nm region.

The fluorescence quantum yield was estimated in comparison to that for rhodamine 6G in methanol as a standard, for which $\Phi_F = 0.93$.[127] The integrated area of the fluorescence emission spectrum for a β-carotene solution was determined by fitting it to a normalized lognormal line shape[128] or to a sum of lognormal line shapes. The absolute quantum yield was then calculated as discussed in reference[129] using

$$\Phi_{f,car} = \Phi_{f,ref} \frac{F_{car} \left[1 - 10^{-A_{ref}} \eta^2_{car}\right]}{F_{ref} \left[1 - 10^{-A_{car}} \eta^2_{ref}\right]} \quad (10)$$

where $\Phi_{F,car}$ and $\Phi_{F,ref}$ are the quantum yields, F_{car} and F_{ref} are the integrated areas of the fluorescence spectra, A_{car} and A_{ref} are the absorptions at the excitation wavelengths, and n_{car} and n_{ref} are the indices of refraction of the two solvents used in the β-carotene (car) and rhodamine 6G (ref) samples, respectively. The fitted lognormal line shapes were optimized to avoid interference from the excitation light scattering and Raman scattering peaks in the fluorescence spectra. The resulting estimates of the absolute fluorescence quantum yield reliably allow a comparison of the yields in the different solvents.

3.3.6 Electronic Structure Calculations

Electronic structure calculations were performed with the B3LYP hybrid functional,[130,131] a 6-31G(d) basis set, and an ultrafine grid for integration, as implemented in Gaussian 16 revision A.01.[132] As discussed below, relaxed potential energy scans were conducted around each double bond of β-carotene and of those in a truncated analogue in which the β-ionone rings were replaced by hydrogens. These scans were conducted around each bond by varying the dihedral angle from 180° to 90°. The all-*trans* and twisted conformers were submitted to time-dependent density functional theory (TD-DFT) calculations under the Tamm-Dancoff approximation using the CAM-B3LYP/6-31G(d) model chemistry.[133] For full-length, all-*trans* β-carotene, this level of theory delivers an $S_0 \rightarrow S_2$ vertical excitation energy within ~0.08 eV (~12 nm) of the experimental absorption maximum at 460 nm. This combination of two different levels of DFT and/or basis sets, one for ground state optimization and the other for excited state energies, has been used before and particularly in the context of carotenoids.[31,32] The transition density for the $S_0 \rightarrow S_2$ excitation was generated with MultiWFN[134] and visualized in Gaussview.

3.4 Results

3.4.1 Fluorescence Anisotropy Detection of Barrier Crossing and Excited State Torsional Distortion

Figure 3.3 compares the room temperature (23°C) absorption spectrum with the fluorescence spectra observed at two excitation wavelengths from β-carotene in hexane solvent. As discussed previously by Gillbro and Cogdell,[88] the fluorescence and absorption spectra overlap over the ~480–520 nm region, which is consistent with an assignment of the emission to the S_2 state. Owing to the low quantum yield, ~10^{-6}, the broad fluorescence lineshape is decorated with sharper line shapes arising from light scattering at the excitation wavelength, from resonance Raman scattering at the C-C and C=C mode frequencies, and from non-resonance Raman scattering from the hexane solvent. The Raman signals move at fixed Stokes shifts (in wavenumbers) as the excitation wavelength is scanned across the absorption spectrum, revealing as they move that the obscured part of the fluorescence line shape lacks any resolved vibronic structure. In contrast, the absorption spectrum exhibits a partially resolved vibronic progression in the BLA coordinates. This observation indicates that the optically prepared S_2 state abruptly undergoes a change in electronic structure that increases the solvation reorganization energy (or system–bath coupling). The absorption transition would be expected to impact the chromophore–solvent interactions by increasing the chromophore's permanent dipole moment and/or the molecular size relative to the that of the surrounding solvent cavity.

As the excitation wavelength is scanned from the 0–0 region (Figure 3.3) of the vibronic structure of the absorption spectrum, the fluorescence spectrum exhibits a significant broadening in the emission bandwidth and is strengthened especially in the near-IR, >600 nm region.

The oscillator (or dipole) strengths $\epsilon(\nu)/\nu$ and $\lambda^2 F(\nu)/\nu^3$ express the squares of the absorption and fluorescence transition probabilities[123,135] with respect to the wavenumber, ν, as determined by the absorption and the fluorescence intensity, $\epsilon(\nu)$ and $F(\nu)$, respectively, and with λ standing for the wavelength.[136–139] In Figure 3.3, the fluorescence oscillator strength spectra obtained with excitation at 490 nm and 430 nm are plotted with consistent scaling factors after normalizing

them for the excitation light intensity. Tuning of the excitation wavelength to 430 nm from 490 nm substantially increases the oscillator strength of the fluorescence emission across the entire detection range but especially below ~18000 cm^{-1}.

The oscillator strength spectra make it clear that a second fluorescence band is superimposed on the tail of the main emission band from S_2. This second band is assigned to emission from the S_1 state following nonradiative decay from S_2. The contribution from the S_1 fluorescence band is not nearly as obvious in the intensity spectra plotted in Figure 3.3 due to the effective attenuation by the fixed wavelength bandpass of the emission spectrograph. Although the signal/noise ratio is relatively poor in this region of the spectrum owing to the decreasing sensitivity at long wavelengths of the silicon CCD detector used in these experiments, one can discern the weak emission band from S_1 in the spectrum obtained with 490 nm excitation (Figure 3.3) from its apparent peak maximum in the ~14000 cm^{-1} range. A weak S_1 spectrum from β-carotene in carbon disulfide in this wavenumber region was detected previously with a germanium detector and laser excitation by Andersson et al.[140]

The S_1 band observed with excitation at 430 nm (Figure 3.3), however, is substantially stronger than observed with 490 nm excitation. Its line shape is broader, extending at least from 18000 cm^{-1} to the low frequency limit of the detected spectra, and its peak maximum is markedly blue shifted. Further, the intensity is modulated over the 13500–14000 cm^{-1} range, which may arise from partially resolved vibronic structure. The S_1 fluorescence spectrum reported by Andersson et al.[140] was assigned a weak vibronic progression in the BLA mode frequencies.

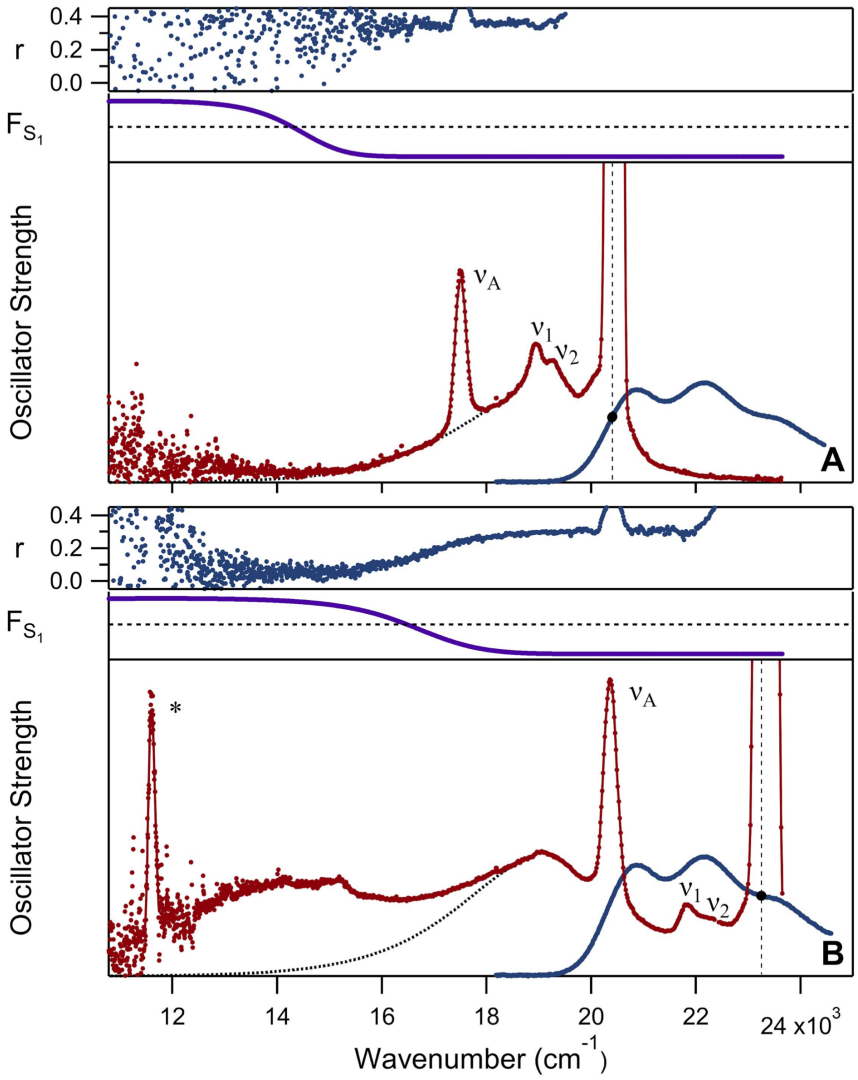

Figure 3.3 Fluorescence oscillator strength and anisotropy (r) spectra for β-carotene in hexane at 293 K: (a) with excitation at 490 nm (20,400 cm^{-1}); (b) with excitation at 430 nm (23,250 cm^{-1}). The magic-angle fluorescence oscillator strength (red) is plotted after correction for the intensity of the excitation light at the two wavelengths with the same intensity scaling in panels (a) and (b). The excitation wavenumber is marked in each panel with a vertical dashed line. The absorption oscillator strength (blue) is arbitrarily scaled to mirror that of the S_2 fluorescence emission line shape. A baseline for the S_1 emission is suggested by a lognormal lineshape for the red tail of the S_2 emission. FS_1 (purple) estimates the fraction of the fluorescence oscillator strength from the S_1 state; FS_1 = 0.5 is marked by the dashed line. The positions of resonance Raman peaks from β-carotene (ν_1 = 1517 cm^{-1} and ν_2 = 1157 cm^{-1})[141] and for a non-resonance Raman peak from the hexane solvent (ν_A = 2966 cm^{-1})[142] are marked. Also marked (*) is the second-order excitation light scattering peak. Figure reprinted with permission from reference 42. Copyright 2020 American Chemical Society.

As the emission TDM is rotated away from alignment with the absorption TDM, the anisotropy decreases. Complete loss of memory of the photoselected absorption TDM direction due to rotational diffusion would result in a full depolarization of the fluorescence emission and an anisotropy of 0.0, but the rotational correlation time measured for β-carotene in hexane determined using optical Kerr effect measurements is 115 ps at 20°C.[143] Depolarization of the fluorescence from S_2 from rotational diffusion is entirely negligible owing to the <150 fs lifetime of the S_2 state. Further, for the S_1 emission, at most a 5 percent decrease in the fluorescence anisotropy would accompany rotational diffusion averaged over the 10 ps lifetime[75,98,144,145] of the S_1 state. Thus, fluorescence anisotropies much lower than 0.4 arise in carotenoids from an internal rotation of the emission TDM relative to the photoselected direction of the absorption TDM.

With excitation at 490 nm (Figure 3.4), the minimum anisotropy observed in the S_2 emission region at 16,500 cm^{-1} is ~0.35, which indicates only a 17° rotation of the emission TDM from the direction of the vertical absorption TDM using equation 2. A similar anisotropy value extends across the weak S_1 emission region, though the signal/noise ratio is very poor. With excitation at 430 nm (Figure 3.4), however, the anisotropy is as low as 0.28 in the S_2 region, implying a rotation of the emission TDM by 26°. An even lower anisotropy is then observed in the S_1 region, 0.05, corresponding to a rotation of the TDM by almost 50°. These results make it clear that tuning the excitation wavelength to shorter wavelengths over about a 3000 cm^{-1} range from the 0–0 transition results in an increased rotation of the emission TDM in both the S_2 and S_1 bands.

We carried out additional studies of the fluorescence properties of β-carotene in three additional aprotic solvents affording comparable solubility to that in hexane: chloroform, carbon disulfide, and most notably, 2-methyltetrahydrofuran (Figure 3.4, 2-MTHF). In this solvent, the S_2 fluorescence anisotropy is ~0.2, somewhat lower than observed in hexane, whereas the fluorescence anisotropy from the S_1 state is significantly lower in the nonpolar solvents, ~0.06, compared to that in the polar solvents, ~0.15. Additionally, the S_1 emission exhibits some weakly resolved vibronic structure not previously observed in hexane.

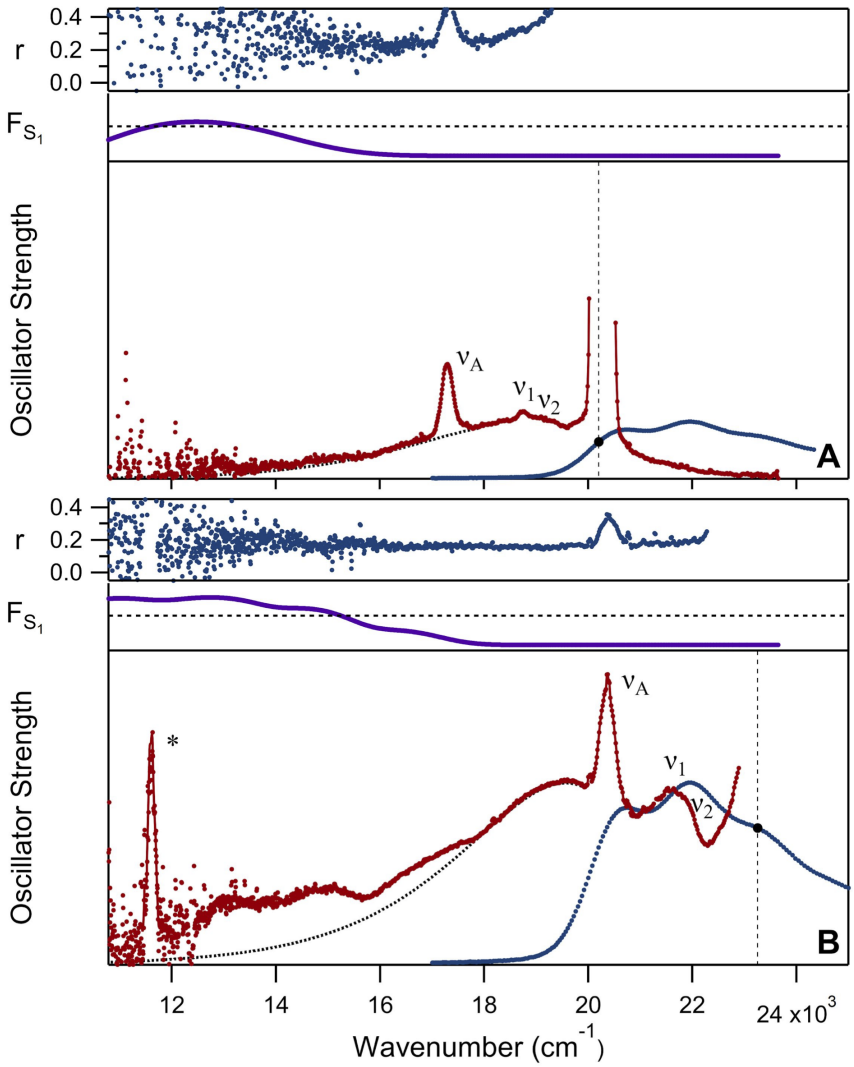

Figure 3.4 Fluorescence oscillator strength and anisotropy (r) spectra for β-carotene in 2-MTHF at 293 K: (a) with excitation at 495 nm (20,200 cm^{-1}); (b) with excitation at 430 nm (23,250 cm^{-1}). Other details are as indicated in the caption to Figure HEXANE, including plotting the fluorescence oscillator strength spectra with the same intensity scaling in panels (a) and (b). The positions of resonance Raman peaks from β-carotene (ν_1 = 1517 cm^{-1} and ν_2 = 1157 cm^{-1})[141] and for a non-resonance Raman peak from the 2-MTHF solvent (ν_A = 2915 cm^{-1})[146] are marked. Figure reprinted with permission from reference 42. Copyright 2020 American Chemical Society.

These aspects have been observed previously by other workers, but the fluorescence line shape and anisotropy properties were not simultaneously connected in any prior work, to our knowledge. Gillbro and Cogdell[88] reported a decrease in the fluorescence emission anisotropy from β-carotene in carbon disulfide at a single emission wavelength, 570 nm, as the excitation wavelength was scanned to the blue over the 500 nm to 400 nm range; fluorescence emission spectra over this

excitation tuning range were not shown. The results described above for the S_2 emission are in line with their findings. To explain the anisotropy decrease, Gillbro and Cogdell proposed that the absorption spectrum contains two overlapping bands with distinct emission TDM directions. A similar argument was made by Oustramov et al.[107] to account for their observation that the fluorescence line shape of β-carotene deviates from mirror symmetry and from that expected from the Stepanov relation, which assumes that no structural rearrangements occur from the Franck–Condon structure and that the emission arises from the lowest vibrational level of the emitting state.[147] In fact, it was concluded in this work that the majority of the fluorescence emission with excitation near the 0–0 transition arises from optical preparation of the low lying B state of Tavan and Schulten mentioned in the introduction. Tuning of the excitation into the blue wavelengths associated in the present work with the near-IR fluorescence was not reported nor was there any discussion of fluorescence anisotropy results.

We should point out at this point that the possible presence of overlapping transitions in the mid-visible absorption band of β-carotene does not really provide a satisfactory physical explanation for the correlated changes observed here in the fluorescence line shape and anisotropy. As shown below in the electronic structure calculations and consistent with previous work,[118,140] the TDMs of all-*trans* carotenoids are well aligned longitudinally with the direction of the isoprenoid backbone. Contribution from $\pi \rightarrow \pi^*$ transitions with TDMs components in the transverse direction would be expected to be blue shifted from the main band and much weaker in oscillator strength. Further, linear dichroism spectra indicate that photoselection of ground-state molecules with *cis* configurations does not occur over the 430–500 nm excitation range.[148] The *cis* band in β-carotene is located at shorter wavelengths, ~300–350 nm.[122]

The carotenoid canthaxanthin differs from beta-carotene because it has carbonyl groups on the terminal rings, which are conjugated with the rest of the polyene backbone. This increases the available length for electron delocalization and potentially serves as a stabilizer of charge separation in the excited state.

The absorbance spectrum of canthaxanthin in 2-MTHF solution (Figure 3.5) absorbs over the same frequency range as beta-carotene, but lacks resolved vibronic structure at room temperature, immediately suggesting increased interactivity between the excited state molecule and the surrounding solvent. In comparison to beta-carotene in the same solvent and with the same excitation wavelength, the emission lineshape of canthaxanthin is characterized by an equally broad emission spectrum but lacks the resolved vibronic structure of the S_1 state emission.

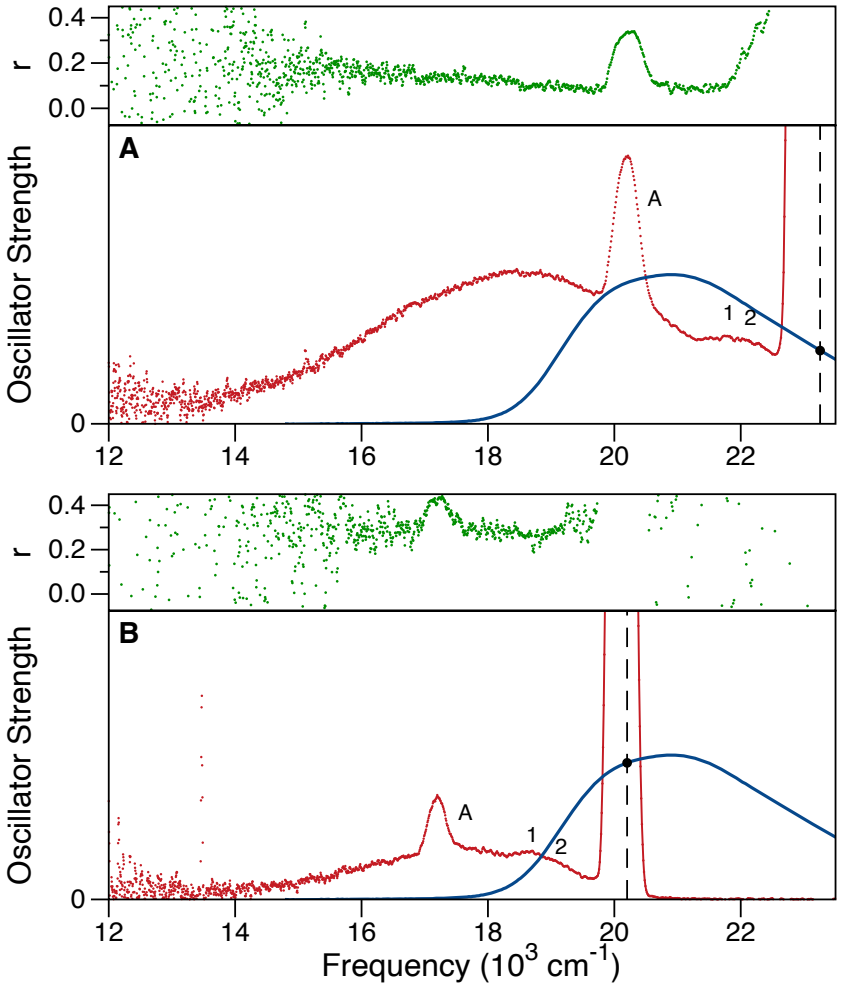

Figure 3.5 Fluorescence oscillator strength (red), absorbance oscillator strength (blue), and anisotropy (r, green) spectra for CAN in 2-MTHF at 293 K with excitation at (a) 430 nm (23,250 cm^{-1}) and (b) 495 nm (20,200 cm^{-1}). The magic-angle fluorescence oscillator strength (red) is plotted after correction for the intensity of the excitation light at the two wavelengths with the same intensity scaling in panels (a) and (b). The excitation wavenumbers are marked in each panel with a vertical dashed line. The positions of resonance Raman peaks from canthaxanthin (1 = 1517 cm^{-1} and 2 = 1157 cm^{-1})[141] and for a non-resonance Raman peak from the 2-MTHF solvent (A = 2966 cm^{-1})[142] are marked.

The fluorescence anisotropy measurement of canthaxanthin in 2-MTHF differs significantly from that of beta-carotene. Emissions from canthaxanthin exhibit a higher anisotropy, with a minimum r value of 0.08 or xxx degrees, and show a positive trend with increasing emission frequency. The emission that occurs after being excited to the 0-0 vibronic peak position at 20,200 cmˆ-1 is almost the same as that of beta carotene. This indicates that being excited with energy that only causes BLA does not explain the significant dynamic changes in the excited state.

3.4.2 Temperature Dependence of Volume-coordinated Torsional Distortion

An alternative explanation for the fluorescence anisotropy results is that the isoprenoid backbone of canthaxanthin undergoes out-of-plane distortions that rotate the emission TDM while still evolving on the S_2 potential energy surface during the <100 fs emission timescale.[75,85,149] The excitation wavelength dependence of the fluorescence anisotropy would then indicate that passage over a low activation barrier from the Franck–Condon region of the S_2 state's potential energy surface, as depicted in Scheme 3, is required to access to the potential energy gradient with respect to out-of-plane motions. Further, the lower anisotropy observed in the S_1 fluorescence band would be explained by an additional internal rotation of the emission TDM that follows passage through the CI from the S_2 state.

A test of the possible assignments for the fluorescence anisotropy of canthaxanthin can be made by performing a series of fluorescence observations as a function of temperature. At low temperatures, a high fluorescence anisotropy would be expected if the friction from the surrounding frozen solvent inhibits large amplitude out-of-plane motions from the Franck–Condon S_2 state structure. On the other hand, if tuning of the excitation wavelength to shorter wavelengths changes the fluorescence line shape or anisotropy because of coming into resonance with a low lying B state, the alternative assignment suggested above, the same anisotropy value would be anticipated at low and higher temperatures. Lowering the temperature would then be expected mainly to result in a sharpening of the fluorescence line shape without affecting the anisotropy.

Cryogenic fluorescence measurements were recording using the solvent 2-MTHF because it forms high quality clear glasses of carotenoid solutions at cryogenic temperatures,[122] which would be favored to lower the background light scattering that might obscure the weak fluorescence signals anticipated from canthaxanthin. A fixed excitation wavelength was used, 430 nm, which obtains at room temperature the signal shown in Figure 3.5 featuring a low anisotropy value, 0.08, in the S_2 band and 0.17 in the S_1 band. The absorption and fluorescence spectra were recorded sequentially at a given temperature with the canthaxanthin sample in 2-MTHF held in the liquid nitrogen cryostat. Figure 3.6 shows the absorption and fluorescence spectra from canthaxanthin in 2-MTHF at 77 K and 293 K. The panels present the fluorescence oscillator strength and anisotropy spectra in these solvents in the same manner used above.

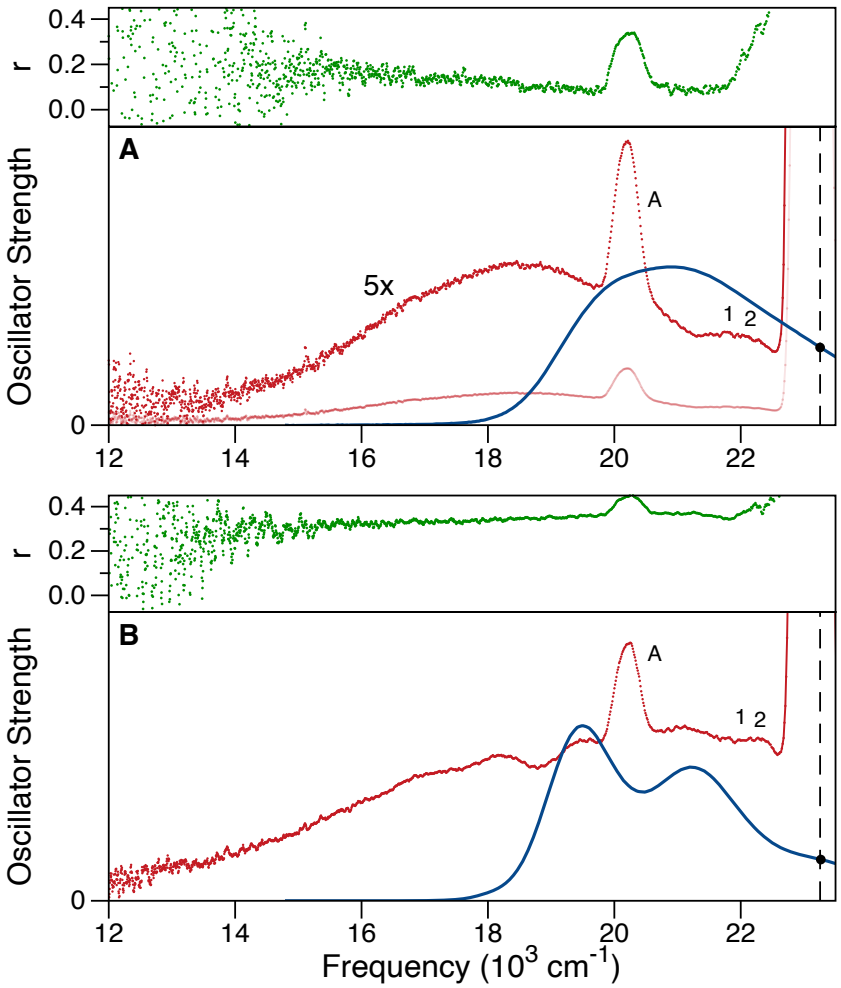

Figure 3.6 Fluorescence oscillator strength, absorbance oscillator strength (blue), and anisotropy (r) spectra for CAN in 2-MTHF with excitation at 430 nm (23,250 cm^{-1}) at 293 K and 77 K (a and b, respectively). The fluorescence lineshape of CAN at room temperature has been magnified by 5x for comparison to the 77 K spectrum. The excitation wavenumber is marked with a vertical dashed line. The absorption oscillator strength is arbitrarily scaled to mirror that of the fluorescence emission line shape. The positions of resonance Raman peaks from canthaxanthin (1 = 1517 cm^{-1} and 2 = 1157 cm^{-1})[141] and for a non-resonance Raman peak from the 2-MTHF solvent (A = 2966 cm^{-1})[142] are marked.

As the temperature is lowered, the absorption spectrum from canthaxanthin in 2-MTHF shifts with respect to the room temperature spectrum to lower wavenumbers and develops vibronic structure. This effect can be attributed to a constriction of the solvent cavity around the canthaxanthin chromophore in the ground state as the temperature decreases in the dark prior to illumination. The

shift of the absorption spectrum to the red as the temperature is lowered arises from the temperature dependence of the solvent polarizability.[88,118,150,151]

The main result from Figure 3.6, however, is that the integrated oscillator strength of the fluorescence emission from canthaxanthin with 430 nm excitation markedly increases as the temperature is lowered due to a new contribution to the emission spectrum from a short-lived spectral "intermediate" along the S_2 to S_1 nonradiative decay pathway. The fluorescence oscillator strength spectra are shown with absolute scaling in Figure 3.6 to make clear how much stronger the emission is at 77 K; the quantum yield determined from the integrated oscillator strength is 7 times larger at 77 K than that at room temperature. As the temperature is raised above 77 K, the fluorescence spectrum maintains its broad lineshape albeit with a decreasing amount of emission in the blue rangeas it decreases in intensity, essentially disappearing above 200 K to reveal the underlying much weaker S_2 and S_1 emission bands characteristic of the high temperature emission spectrum.

The broad emission lineshape observed at 77 K very likely corresponds to formation of a distorted intermediate moving on the out-of-plane potential energy gradient linking the Franck–Condon S_2 state to the CI with the S_1 state (Scheme 3). The lineshape is comparable to that determined as the instantaneous species associated difference (SADS) spectrum observed by de Weerd et al.[113] in a global target analysis of their femtosecond pump–continuum probe spectra with β-carotene at room temperature in three solvents. These signals should not be regarded as arising from a conventional intermediate spectroscopic state; the breadth of the fluorescence signals observed at 77 K would correspond to uncertainty broadening of a state with an infinitessimal lifetime, ~660 as, which would preclude its detection via fluorescence. Thus, the overall breadth of the fluorescence (and SE) signals from canthaxanthin reflect the integral of narrower lineshapes from molecules moving rapidly on the S_2 out-of-plane gradient over the <150 fs timescale. As the temperature is raised over the 77–293 K range for the example spectra in Figure 3.6, the solvent viscosity (and the resulting friction) decreases over many orders of magnitude.[152] Above 200 K it is evident that the time spent by a given molecule on the out-of-plane gradient is very short indeed.

Very few fluorescence photons are detected during progress to the CI with the S_1 state, allowing the high temperature S_2 and S_1 emission bands to be observed.

The high fluorescence anisotropy value detected at 77 K, 0.36, indicates that the isoprenoid backbone of canthaxanthin is still constrained at 77 K to point roughly along the direction of the equilibrium ground state structure even though the emission spectrum reports the presence of a distorted intermediate. This finding strongly suggests that concerted out-of-plane distortions of more than one bond occur along the isoprenoid backbone of canthaxanthin when large volumes of motion are constrained by the frozen solvent cavity. The "bicycle pedal"[65] and "hula-twist" mechanisms[153] for the retinal PSBs in rhodopsin or bacteriorhodopsin are well discussed examples of out-of-plane pathways leading to fully photoisomerized structures incorporating torsions of more than one bond along a polyene's length. These structures are termed volume conserving because they can occur from initially all-*trans* configurations despite being confined by the frozen solvent cavity at low temperature.[154] Further, assumption of these structures would not be reported by a large internal rotation of the emission TDM since a large sweep of half of the isoprenoid backbone of β-carotene would not be required as it would for a single-bond distortion.

At higher temperatures, the melting 2-MTHF solvent apparently allows the isoprenoid backbone of canthaxanthin to lower its conformational potential energy further by relaxing further out-of-plane at a single point along its length. This process results in lower anisotropy values Figure 3.7 shows that the minimum anisotropy smoothly decreases over the 77–200 K range to level off at the 0.16 value observed in the S_2 and S_1 emission regions in 2-MTHF at high temperatures. Although the confidence intervals are large and overlap extensively, the anisotropy measured for the S_1 emission exhibits an decreasing trend as the temperature is raised. The lifetime of the S_1 state is ~5.4 ps,[75,98,144,145,149] somewhat longer than the 0.5–2 ps timescale associated for vibrational cooling in carotenoids,[122,155] so the emission spectrum from S_1 would be expected to be that from an ensemble nearly at thermal equilibrium with the surrounding medium.

The coupling of the temperature dependence of the fluorescence quantum yield and anisotropy observed here for canthaxanthin in 2-MTHF had not been reported previous to our work on beta-

carotene,[42] but Andersson et al.[156] observed a comparable temperature dependence for the quantum yield of fluorescence from the triene analog of β-carotene, mini-3. The mini-carotenes exhibit a fluorescence spectrum with a more pronounced "dual" character, with bands from the S_2 and S_1 states both apparent.[129] The shortest of these, mini-3, having only a single/double bond backbone between the two β-cyclohexane rings, absorbs in the 250 nm region of the UV and emits in the 360 nm region. The fluorescence quantum yield of mini-3 was observed to follow an Arrhenius dependence with an activation energy of 610 cm^{-1}; over the 77–110 K temperature range, the quantum yield decreases from 0.61 to 0.04. Andersson et al. discuss this trend in terms of a nonradiative decay mechanism promoted by out-of-plane torsional motions. The fluorescence anisotropy measured at 77 K is high, 0.39, but unfortunately no measurements of the anisotropy at higher temperatures were reported, most likely because the fluorescence quantum yield decreases to very low values in liquid media, rendering it effectively "nonfluorescent."[156] In mini-3, the activation energy barrier (Scheme 3) for access from the Franck–Condon region of the S_2 potential energy surface to the out-of-plane gradient would be expected to be small or nonexistent compared to that in canthaxanthin, which requires excitation to the 0-2 vibronic transition to cause out of plane torsional distortion associated with large rotation of the transition dipole moment (Figure 3.7).

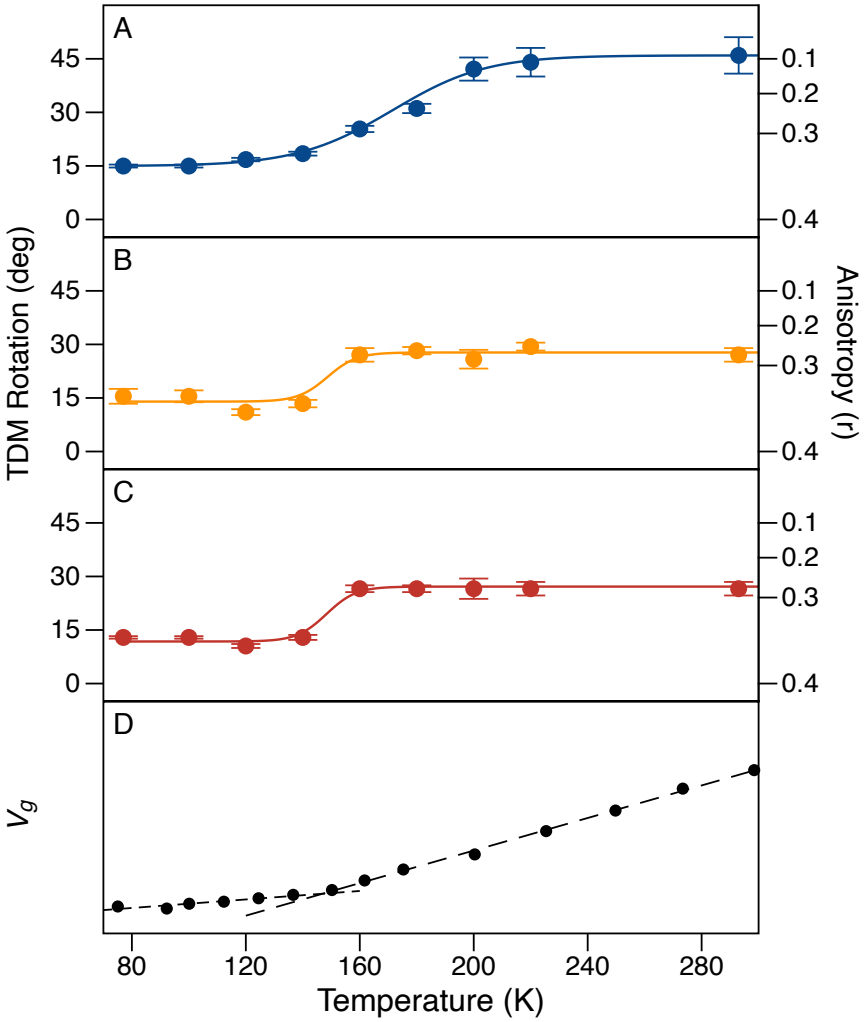

Figure 3.7 Vibronic transition excitation wavelength (panels a-c, 0-2, 0-1, and 0-0, respectively) and sample temperature (77 K to 293 K) dependence for TDM rotation of canthaxanthin in 2-MTHF solvent. (d) The specific volume of 2-MTHF calculated by Tan et al.[157] depicts the glassing temperature of 2-MTHF solvent at approximately 140 K.

3.4.3 Electronic Structure and DFT Calculations

To explore how internal out-of-plane structural deformations of the isoprenoid backbone of carotenoids in the S_2 state might cause the emission TDM to rotate, producing the experimentally observed low minimum fluorescence anisotropies, we computed the electronic structures of a set of torsionally distorted β-carotene conformers starting from the all-*trans* structure. As the simplest case, we consider here a single torsional coordinate for the initial excited state relaxation

away from the Franck–Condon region of the S_2 potential energy surface. Of course, the possibility that rotations of more than one coordinate of the isoprenoid backbone contribute to the observed rotation of the TDM should not be dismissed arbitrarily. As noted above, concerted or sequential torsions of more than one C–C bond have been discussed, in particular for the photochemistry of retinal PSBs in rhodopsin and bacteriorhodopsin.[154] Further, calculations by Hynes and coworkers[158] on retinal PSB models indicate that the torsional and pyramidal coordinates are strongly coupled, so the out-of-plane distortions observed in β-carotene would very likely involve simultaneous displacements along both coordinates.

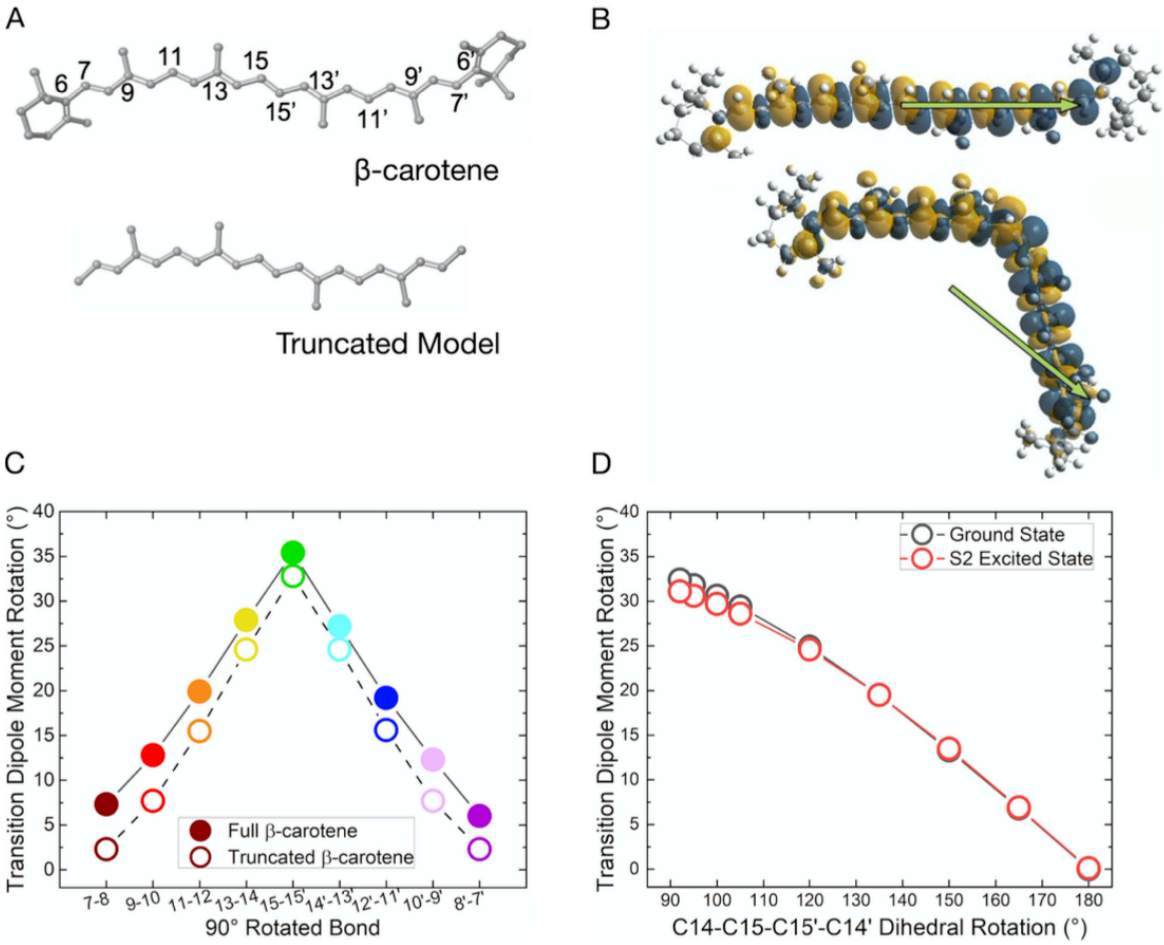

Figure 3.8 (a) Minimum energy structure of β-carotene and of a truncated model, with a numbering scheme indicated (as also used in Scheme 2) for the carbon atoms in the isoprenoid backbone. (b) Optical transition densities for the $S_0 \rightarrow S_2$ absorption transition for the all-trans structure and for the C15-C15' 90°-twisted structure. Orange/blue orbital colors denote an instantaneous gain or loss of electron density, respectively, upon excitation. Green arrows indicate the direction of the TDM with the vector origins drawn at the center of mass. (c) Calculated TDM rotations with respect to the all-trans structure as a function of the choice of the bond undergoing a 90° torsion for the $S_0 \rightarrow S_2$ absorption TDM, the latter for the truncated model. (d) Calculated rotations for the $S_0 \rightarrow S_2$ absorption and $S_2 \rightarrow S_0$ emission TDMs with respect to torsions of the C15-C15' bond of β-carotene, the latter for the truncated model. Figure reprinted with permission from reference 42. Copyright 2020 American Chemical Society.

Potential energy surface scans in the electronic ground state, S_0, were conducted with respect to torsion of each of the labeled bonds numbered in Figure 3.8a, with the C–C=C–C dihedral angle varied from 180° for the nominally planar, all-*trans* structure to 90°. This procedure allows a smooth relaxation of the internal coordinates to accompany the fixed torsional distortion. The computed

transition density isosurfaces and the $S_0 \rightarrow S_2$ absorption TDM vectors for the particular example of rotation around the C_{15}–$C_{15'}$ double bond are shown in Figure 3.8b. The colored isosurfaces show how the π-electron density increases or decreases upon optical excitation. The TDM vectors are referenced in each conformation with respect to the center of mass. Figure 3.8c summarizes how the orientation of the TDM depends on which C–C bond in the isoprenoid backbone is twisted to assume a 90° conformation. The rotation angle is determined relative to the orientation of the TDM for the all-*trans* configuration. This angle would be expected to be comparable to that for the vertical fluorescence emission transition from a distorted S_2 structure to the ground state. Twisting of bonds 14-15, 15-15', and 15'-14' to the 90° conformation rotates the TDM by 28–35°, with the largest rotation arising from twisting the central C_{15}-$C_{15'}$ bond.

The results shown in Figure 3.8c for rotations of the absorption TDM due to torsions of the isoprenoid backbone of β-carotene in the ground state are recapitulated by relaxed scans of the S_2 potential energy surface of a truncated version of β-carotene in which the β-ionone rings have been replaced by hydrogen atoms (Figure 3.8a). This truncation lessens the time and considerable expense required for excited-state optimizations; the π-electron density is mostly resident on this section of the β-carotene structure. Figure 3.8d compares the calculated rotations for the $S_0 \rightarrow S_2$ absorption and $S_2 \rightarrow S_0$ emission TDMs with respect to torsions of the C_{15}-$C_{15'}$ bond for the truncated model. The TDM rotations were found to agree within 2°. This agreement justifies the use of ground state conformers for the TDM rotation analysis for the full β-carotene structure (Figure 3.8c). The close agreement between these two calculations demonstrates that 90° torsional distortions of a single C–C bond near the center of the isoprenoid backbone are remarkably consistent with the 39° TDM rotations determined by the fluorescence anisotropy values of 0.16 for the S_2 band in the polar solvents, chloroform and 2-MTHF. The barrier for torsions would be expected to be the lowest near the center of the isoprenoid backbone, where the BLA amplitude is the smallest along the chain.[159]

It is important to clearly state the assumptions we are making to model the hypothesised torsional conformations. The purpose of the scan of the torsional angles on the S_0 and S_2 surfaces, the latter

for the truncated model, is strictly to make a correlation between the structure and the direction of the vertical transition dipole moment (TDM) for transitions between the two surfaces. This work is intended to extend the general conclusion[118,140] that the transition dipole moments of linear polyenes point down the isoprenoid backbone. To our knowledge, there have not been any reports of electronic structure calculations of the TDM directions in twisted conformers or even in *cis* configurations. The structures at each torsional angle should be considered local minima because the energy was minimized at each stated torsional conformation, primarily to avoid steric clashes, but a global minimum energy path was not sought given that we held only one torsion fixed during the energy minimization. Further, we have not attempted calculations of the TDM direction in the S_1 state because it is well known that TDDFT methods should not be used to model states involving a large component of double excitations. There is no reason to suggest, however, that the S_1 state's TDM direction should point in a different direction from that determined for the S_0 or S_2 states.

A physical explanation for the larger rotations of the TDM observed in the nonpolar solvents, 48–50°, requires the displacement of an additional coordinate of the isoprenoid backbone of β-carotene during the fluorescence emission timescale. Of particular interest is the possibility that a pyramidal distortion converts the diradical electron configuration of a twisted bond to the lone-pair configuration consistent with a full ICT.[115,116] The pyramidal structure corresponds to a candidate for a CI of the S_2 state with the S_1 state. Although determination of a true CI on the S_2 surface is beyond the scope of the present work (and beyond the capabilities of TDDFT for such a large system), we constructed an *ad hoc* model for the β-carotene CI structure using a template constructed with the internal coordinates of ethylene at the CI determined using spin-flip TDDFT by Minezawa and Gordon.[160] Specifically, the ethylene CI's structure was superimposed with our 90° rotated structure, as obtained via the relaxed scan discussed above. After that, the four dihedral angles of the C_{15}–$C_{15'}$ bond were manually adjusted to visually maximize the overlap between the C_{15}-$C_{15'}$ adjacent atoms and those of the ethylene CI. The structure was then relaxed in the ground state but keeping the dihedral angles of the C_{15}-$C_{15'}$ bond fixed to minimize steric interactions.

Figure 3.9 shows the superposition of three relevant conformations: the all-*trans* structure, the 90° rotated structure used in Figure 3.8b, which gives rise to a 35° rotation of the TDM, and the pyramidal structure resembling the ethylene CI. For the latter structure, the calculated TDM rotation is 47°. This result is remarkably similar to the 48–50° rotation angle observed in the fluorescence anisotropy measurements for the S_1 state in the nonpolar solvents.

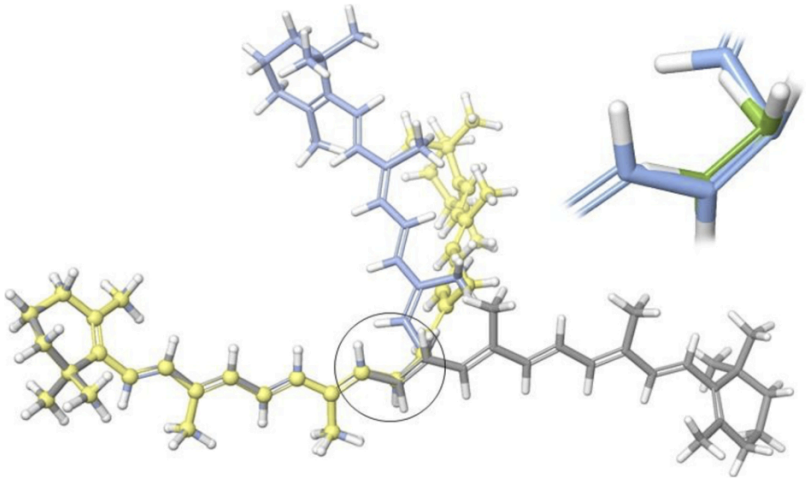

Figure 3.9 Modeled structures representing the Franck-Condon S_2 structure (gray), the 90° twisted conformer (yellow), and a conformer with a pyramidal distortion (light blue). The inset is a zoomed-in view of the circled region, which shows the modeled β-carotene pyramidal structure superimposed with the pyramidal structure of the CI of ethylene (green).[160] Figure reprinted with permission from reference 42. Copyright 2020 American Chemical Society.

Figure 3.10 shows how the emission TDM vectors for the Franck–Condon S_2 state and those of the 90° twisted and pyramidal S_2 conformations are oriented with respect to the molecular frame of the ground-state structure of β-carotene. The ground-state all–*trans* structure is shown in two orientations, with the point-of-view directed in the plane and from above. The TDM vectors are drawn with their origins placed at the center-of-mass, which coincides with the midpoint C_{15}-$C_{15'}$ bond.

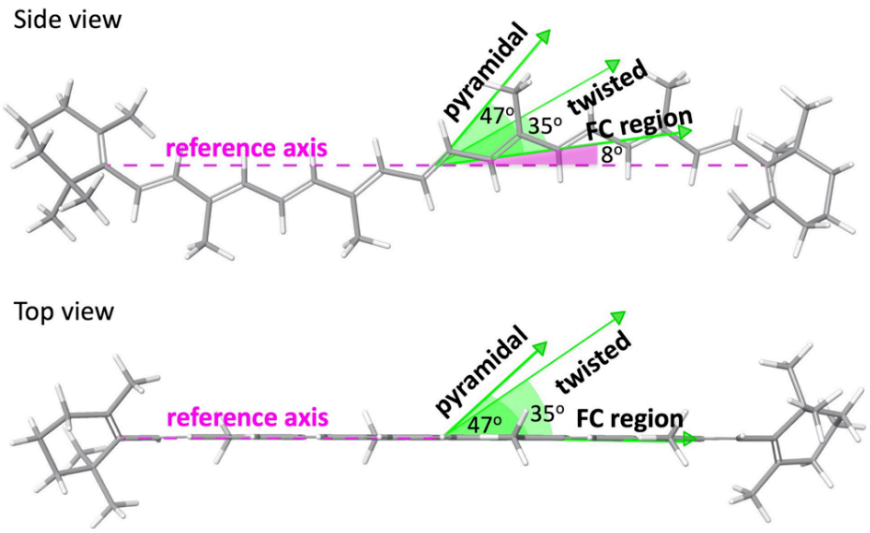

Figure 3.10 Orientations of the emission TDM vectors for the Franck-Condon S_2 state and those of the 90° twisted and pyramidal S_2 conformations with respect to the ground-state structure of β-carotene. The reference axis is the C6-C6' vector. Figure reprinted with permission from reference 42. Copyright 2020 American Chemical Society.

The TDM for the Franck–Condon S_2 state is rotated by 8° with respect to the molecular frame axis, which is chosen here as the vector connecting the C_6 and $C_{6'}$ atoms on the opposite ends of the isoprenoid backbone. In comparison, Birge et al.[119] obtained an estimate of 15° for the orientation of the TDM compared to the molecular frame axis for a conjugated polyene with N = 11 conjugated polyene double bonds with the methyl groups included along the backbone, 12.6° if the methyl groups were not included. The effective conjugation length for β-carotene is shorter than this, but similar values were obtained for N = 8–15. Similarly, Dolan et al.[120] used linear dichroism measurements in squeezed polyacrylamide gels to determine that the absorption TDM is rotated 9.1° from the molecular frame axis in the "corkscrew" ground state conformation of rhodopin glucoside in LH2 from *Rhodopseudomonas acidophila* strain 10050.

Photoexcitation to the S_2 state results in only a small increase in the non-zero permanent dipole moment exhibited by the ground state structure, which is not perfectly C_2 symmetric. The 90° twisted structure has a larger dipole moment, 1.6 D, which implies a significant polar character. A substantially larger dipole moment is determined for the pyramidal structure, 8.3 D, indicating ICT across the C_{15}-$C_{15'}$ bond and delocalization on either side of it. These results are consistent with

the suggestion that evolution on the S_2 surface should be accompanied by a large increase in the solvent friction as the structure nears the CI with the S_1 state.

3.4.4 Fluorescence Anisotropy and Photoactivation Yield of the Orange Carotenoid Protein

Fluorescence emissions from dimers of OCP-CAN have similar fluorescence properties to canthaxanthin in a 2-MTHF solution, such as excitation wavelength dependence, emission breadth, and fluorescence anisotropy.

Compared to canthaxanthin in 2-MTHF, the absorbance spectrum of OCP^O-CAN has increased vibronic resolution because the hydrophobic region between the two protein manifolds decreases the amount of system-bath coupling. When excited at the frequency corresponding to the 0-2 vibronic transition at room temperature (see Figure 3.11), the resulting emission spectrum lacks the vibronic resolution present in the absorbance spectrum. This is due to the electronic reorganization of the carotenoid and the subsequent response of the protein's residues as the forces reach equilibrium. The measured fluorescence anisotropy, r = 0.15, further indicates rotations of the carotenoid within the protein membrane. When the sample temperature is decreased from 293 K to 220 K, the fluorescence quantum yield of OCP^O increases by approximately 3.5 times, appears more mirror-symmetric, and has a lowered anisotropy which indicates primarily small displacements along the polyene chain.

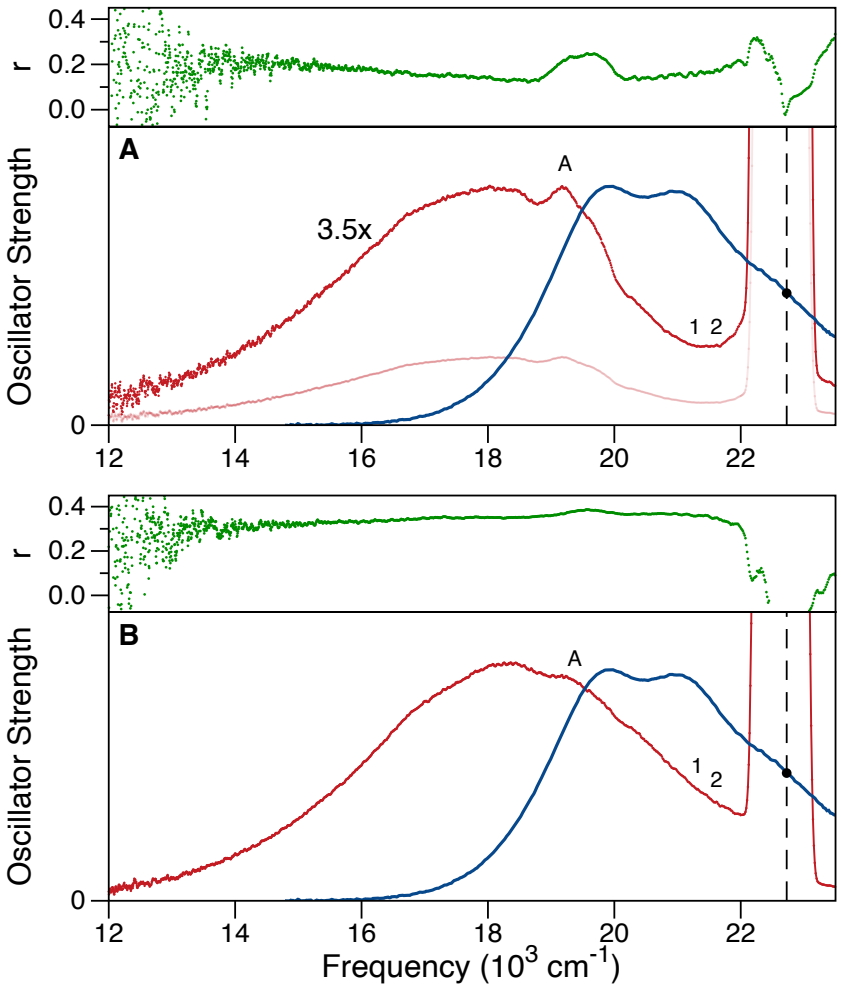

Figure 3.11 Fluorescence oscillator strength, absorbance oscillator strength (blue), and anisotropy (r) spectra for OCP in 60/40 (v/v) glycerol and buffer solution with excitation at 430 nm (23,250 cm^{-1}) at 293 K and 220 K (a and b, respectively). The fluorescence lineshape of OCP at room temperature has been magnified by 3.5x for comparison to the 220 K spectrum. The excitation wavenumber is marked with a vertical dashed line. The absorption oscillator strength is arbitrarily scaled to mirror that of the fluorescence emission line shape. The positions of resonance Raman peaks from the canthaxanthin molecule bound within OCP (1 = 1517 cm^{-1} and 2 = 1157 cm^{-1})[141] and for a non-resonance Raman peak from the buffer (A = 3500 cm^{-1}) are marked.

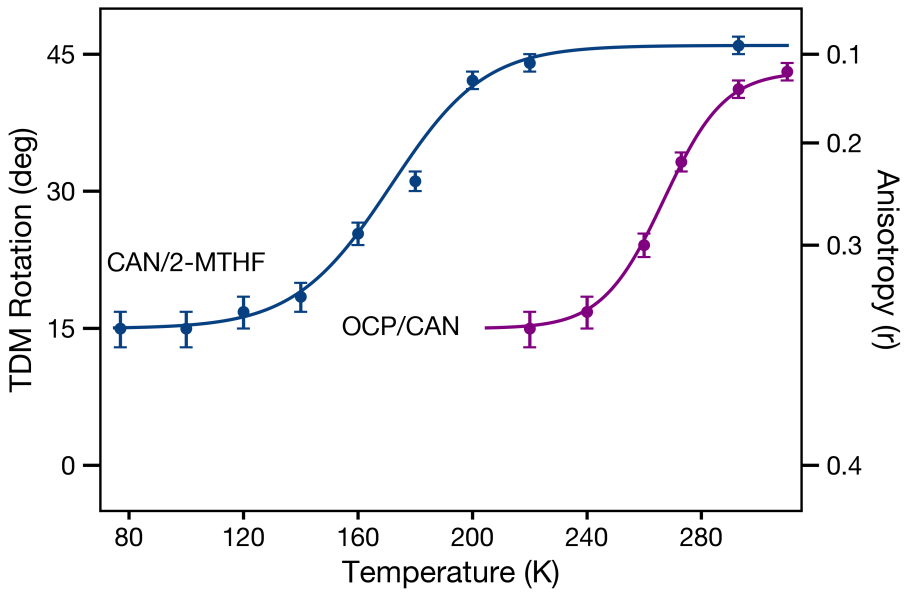

Figure 3.12 Temperature dependence of TDM rotation of CAN in 2-MTHF solvent (blue) and CAN bound within OCP^O in 60/40 (v/v) glycerol/buffer solution as a function of temperature.

When comparing the fluorescence anisotropy of canthaxanthin in OCP and in solution at the 0-2 vibronic transition frequency (Figure 3.12), the total rotation of the transition dipole moment is nearly identical at both room temperature and when the solution medium has been cryogenically frozen, and both also exhibit similar sigmoidal response curves. As the canthaxanthin molecule is effectively shielded from the larger solvent medium by the protein's hydrophobic pocket, as evidenced by identical OCP^O absorption spectra for OCP in buffer and OCP in a glycerol and buffer mixture, the difference in the midpoint of the sigmoidal response likely indicates the temperature at which the protein domains of the OCP^O dimer are frozen in the solution. Consequently, the carotenoid is not able to rearrange the protein to accommodate conformational distortions, leading to non-radiative decay.

Similar to the sigmoidal response displayed by the rotation of the transition dipole moment in OCP^O-CAN (Figure 3.12), the temperature dependence of OCP^O photoactivation also shows a sigmoidal response (Figure 3.13). For this measurement, a simplistic model was used to analyze the change in the absorbance spectrum in the early moments following illumination with photolysis light centered at 440 nm, instead of utilizing the global modeling method outlined in Chapter 2.

The temperature at which photoactivation reaches half of its maximum value is 270 K, but the temperature where the rate of OCP photoactivation reaches half of its maximum value is 281 K. In terms of anisotropy, the difference in TDM rotation between the two temperatures indicates that an additional 6.4 degrees of TDM rotation is required to reach half of the maximum value of photoactivation, possibly indicating the specific minimum magnitude of carotenoid distortion necessary to initiate the photoactivation process.

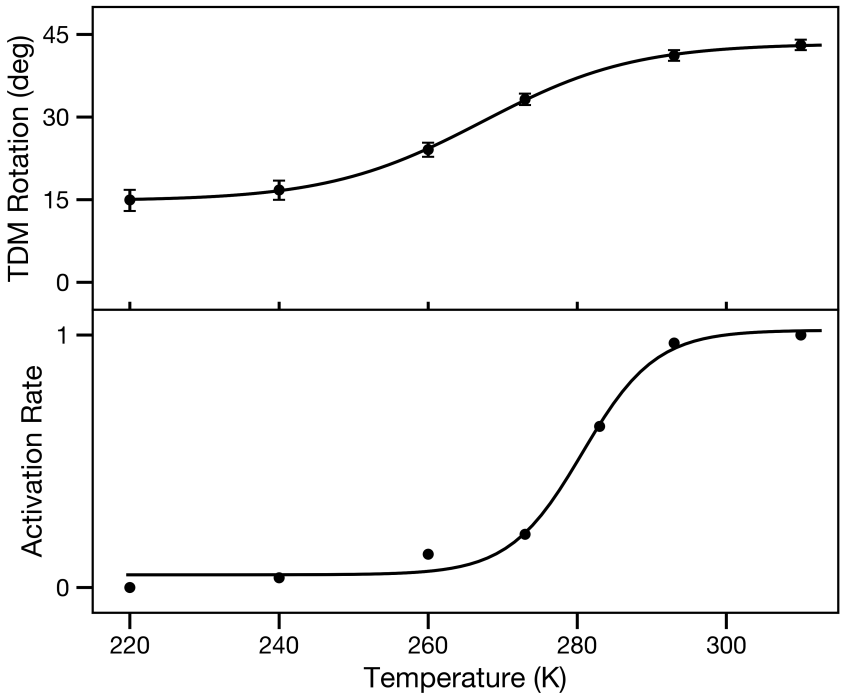

Figure 3.13 Temperature dependence of (top) OCP^O photoactivation with excitation at 440 nm and (bottom) early-time change in OCP^O absorbance spectrum with 440 nm photolysis light.

3.5 Discussion

The results presented above suggest a new picture for the photophysical and photochemical properties of carotenoids arising from optical preparation of the bright S_2 state. As demonstrated here with β-carotene and canthaxanthin, fluorescence emission is observed from two distinct groups of excited-state molecules depending on the excitation wavelength. A fraction is retained by a low activation barrier near the Franck–Condon geometry (Scheme 3); these molecules are optically

prepared by absorption transitions near to the 0–0 transition. The fluorescence spectrum from these S_2 state molecules is roughly mirror symmetric with respect to the absorption spectrum, and the fluorescence anisotropy is at least 0.35, near to the 0.4 value expected for molecules retaining the essentially planar all-*trans* structure photoselected from the ground state ensemble. An example of a fluorescence spectrum predominantly from these molecules is that observed from β-carotene in hexane with 490 nm excitation (Figure 3.3).

As the excitation wavelength is tuned to the blue over the ~3000 cm^{-1} range spanned in the vibronic structure from the 0–0 transition to the 0–2 transition, an increasing fraction of S_2 state molecules are able to pass over an activation barrier dividing the planar and out-of-plane distorted regions of the S_2 potential energy surface. This part of the excited-state ensemble contributes at high temperatures to a broadening of the red tail of the S_2 spectrum and to a more prominent and blue-shifted S_1 emission band compared to that observed upon nonradiative decay from the planar molecules retained by the barrier.

The work presented here contributes the key connection that the near-IR portion of the emission from S_2 and the enhanced emission from S_1 observed with blue excitation has a low fluorescence anisotropy. This finding indicates that passage over the activation barrier is followed by evolution on a steep gradient on the S_2 state potential energy surface with respect to the out-of-plane coordinates of the isoprenoid backbone (Scheme 3), producing emission that is progressively red shifted from the mirror-symmetric S_2 emission. Over the 77–200 K range, we observed a broad emission band with an enhanced emission quantum yield and a temperature dependent anisotropy that arises from a dynamic intermediate, perhaps S_x or its successor evolving on the out-of-plane gradient. Progress along the out-of-plane coordinates in the S_2 state results in rotation of the emission TDM and quenching of the initially strong emission oscillator strength. Further, electronic structure calculations indicate that an enhanced permanent dipole moment develops due to ICT as the out-of-plane coordinates advance, especially with pyramidalization. The ICT character imparts some solvent sensitivity to the barrier height because the gradient region of the S_2 potential energy surface is increasingly stabilized in polar or polarizable solvents.

The preceding description of the fluorescence emission from canthaxanthin is unconventional because it discusses the emission line shape as being *dynamic*, reporting fast, large amplitude motions on the S_2 state potential energy surface. As determined in the present experiments with continuous excitation, the recorded fluorescence line shape is the sum of the instantaneous, time-resolved line shapes emitted by the evolving excited-state ensemble. This situation is made especially obvious in canthaxanthin for the barrier-crossing molecules because the structural evolution is ultrafast compared to the vibrational relaxation time. In this dynamic picture, the fluorescence line shape, quantum yield, and anisotropy are very sensitive probes of changes of the molecular properties of a chromophore during the emission process.

Several of these ideas have precedence in the work by Kochendoerfer and Mathies[147] on the fluorescence of the retinal PSBs in rhodopsin and isorhodopsin.[147,161] As background on this point, recall that the ordering of the lowest two electronic states for the retinal PSBs is inverted compared to that for carotenoids, with the bright S_1 ($^1B_u^+$) state lying below the dark S_2 ($^1A_g^-$) state.[162] The quantum yield of fluorescence from S_1 is very small due to fast nonradiative recovery to the ground state and photochemistry in a significant fraction of events in the proteins, less so in solution. The potential energy surface of the S_1 state is usually considered barrierless for 11-*cis*-retinal in rhodopsin and isorhodopsin.[163,164] In contrast, a low barrier may precede the torsional gradient on the excited state potential energy surface for all-*trans*-retinal in bacteriorhodopsin.[165,166]

Kochendoerfer and Mathies[147] observed that the maximum of the fluorescence spectrum from retinal in rhodopsin and isorhodopsin tracks the excitation wavelength as it is tuned to shorter wavelengths. At the same time, however, it is notable that the fluorescence line shape broadens considerably into the near-IR. These behaviors are very similar to those reported here for the fluorescence of β-carotene and canthaxanthin. By tuning to shorter wavelengths, the energy of the Franck–Condon structure is increased on the excited-state potential energy surface. Given the present paper's context, the increased breadth of the fluorescence spectrum observed by Kochendoerfer and Mathies with excitation at blue wavelengths is probably consistent with the presence of a low barrier on the retinal excited-state potential energy surface. Although measurements of

the fluorescence anisotropy were not reported by Kochendoerfer and Mathies, low fluorescence anisotropies were observed with excitation at shorter wavelengths in early studies of fluorescence in rhodopsin and bacteriorhodopsin.[167,168] It is also notable that a low anisotropy was observed in the SE signals detected in femtosecond pump–probe anisotropy measurements in bacteriorhodopsin by Haran et al.[169]

This work develops for the first time, however, that the fluorescence anisotropy can provide information on the structure of the isoprenoid backbone of a carotenoid prior to and after nonradiative passage from the S_2 state to the S_1 state. The minimum fluorescence anisotropy measured in the S_2 and S_1 bands for β-carotene with 430 nm excitation in 2-MTHF is fully consistent with that calculated for a 90° twist of one of the carbon–carbon bonds in the middle of the isoprenoid backbone (Figure 3.8). This finding indicates that nonradiative decay from S_2 to S_1 occurs when the isoprenoid backbone is significantly distorted along the coupled torsional and pyramidal coordinates but very likely not at the minimum along the S_2 gradient. The S_2 and S_1 emission bands overlap extensively, so an unambiguous determination of the fluorescence anisotropy reached at the CI seam is not possible. But it is clear that the S_1 emission TDM is rotated even further in canthaxanthin, which extends the conjugation of the isoprenoid backbone into the carbonyl bearing beta-ionone rings, to a rotation of almost 50°. This observation is consistent with the rotation of the emission TDM calculated for a pyramidalized, zwitterionic structure. One explanation is that the presence of the carbonyl substituent on the isoprenoid backbone has an especially large impact on the dynamics on the S_2 and S_1 surfaces due to its electron-withdrawing character, which enhances the permanent dipole moment due to ICT and increases the solvent friction, thereby slowing the progress made on the out-of-plane gradient in the S_2 state. Note that the S_1 state apparently retains a distorted conformation over its 10 ps fluorescence lifetime, which is significantly longer than that expected for vibrational relaxation and thermal equilibration on the S_1 surface.

This discussion indicates that a multicoordinate anharmonic picture is required even to understand qualitatively the excitation wavelength-dependent S_1 emissions observed from carotenoids. The weaker and red-shifted S_1 emission band arising from photoexcited molecules retained by the

activation barrier originates from a minimum on the S_1 potential energy surface in the Franck–Condon region, which is not displaced very much with respect to the out-of-plane coordinates of the isoprenoid backbone. In comparison, a significantly stronger and somewhat blue shifted S_1 emission band is observed from the molecules that pass over the activation barrier. This emission arises from a distinct minimum on the S_1 potential energy surface with a significant displacement from the Franck–Condon structure along the out-of-plane coordinates. The enhanced strength of the emission from the distorted S_1 minimum can be attributed to an enhanced intensity borrowing from the S_2 state that accompanies out-of-plane distortions of the isoprenoid backbone. Note that the apparent enhancement of the depth of the vibronic structure in the S_1 emission suggests the possibility that this minimum has a larger displacement along the BLA coordinates than the Franck–Condon minimum.

The present study of the fluorescence properties of canthaxanthin in solution and in the protein now make it clear that large amplitude out-of-plane motions are possible even when motions of the isoprenoid backbone are strongly hindered by the surrounding medium or the protein binding site. As noted above, all-*trans* configurations of carotenoids in protein binding sites usually exhibit distorted conformations, which would already favor out-of-plane distortions following the vertical optical transition from the ground state. At room temperature in solution it is possible for canthaxanthin to form a zwitterionic structure with charage separation that is stabilized by the carbonyls on the terminal rings, but this is not possible in the OCP^O dimer due to steric constraints from the surrounding protein residues. The total amount of TDM rotation between the two environments (Figure 3.13) is approximately seven degrees, further indicating that the formation of a zwitterionic structure is not formed within the protein. The carotenoid distortions within the protein are likely similar to the out-of-plane volume-constrained bicycle-pedal distortions[65] experienced by canthaxanthin when trapped in frozen 2-MTHF solvent. That the rate of OCP photoactivation lags behind the bound carotenoid's anisotropy provides insight that the latching mechanism of the carotenoid depends only on distortions along the center of the carotenoid isoprenoid backbone, but that a certain degree of torsion from bicycle-pedal motions shortens the bound carotenoid's length,

moving the carbonyls out of hydrogen bonding distance with the protein's residues in two domains, thereby initiating the photoactivation response.

The observation that out-of-plane distorted S_2 structures can be formed despite steric hindrance from the surrounding medium is fully consistent with the recent studies by Geiger, Borhan, and coworkers[170,171] on engineered model retinal PSB-binding proteins, where full photoisomerization, not just conformational distortion, is observed even in protein crystals. In these studies, the X-ray crystal structures indicate that the TDM of the photochemical product species would be restricted to point along the binding site's principal axis. A similar conclusion would be made on the basis of Warshel's early analysis of the photoisomerization mechanism in rhodopsin, where the "bicycle pedal" isomerization mechanism is proposed.[65]

Chapter 4: Future Work and Preliminary Results

In addition to the work completed in this dissertation advancing our knowledge of carotenoid photophysics and OCP photoactivation, additional studies of the effects of the carotenoid's electronic structure on excited state distortions will help confirm the results of our previous experiments.

4.1 Torsional Rigidity of Zeaxanthin

As discovered by Punginelli et al,[14] OCP which binds the carotenoid Zeaxanthin (ZEA, Scheme 4) does not photoactivate from OCP^O to OCP^R, nor does it quench fluorescence from phycobilisomes. Unlike the photoactive ketocarotenoids CAN and 3h-ECN, both β-ionone rings on ZEA are capped with hydroxyl groups, lacking carbonyls which form hydrogen bonds with the protein residue, which offers a *prima facie* structural argument for the lack of OCP-ZEA activity.

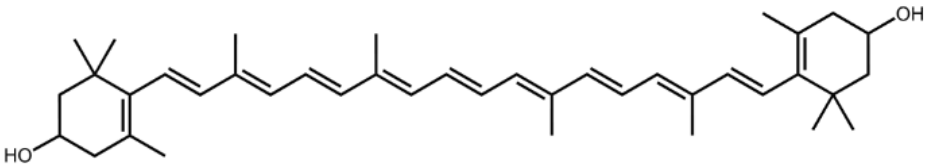

Scheme 4: Structure of zeaxanthin.

Despite the structural similarity to both β-carotene and canthaxanthin, fluorescence anisotropy measurements of zeaxanthin in 2-MTHF (Figure 4.1) solution at room temperature reveal that the potential energy surface of the S_2 molecule does not relax via large magnitude out-of-plane torsional distortions, yet the emission from the S_1 region is slightly distorted. Further experiments measuring the fluorescence anisotropy and quantum yield of ZEA in solvents of varying polarity, paired with theoretical modeling of excited state conformational relaxation, may reveal additional details of carotenoid potential energy surfaces and the interactions between carotenoids and protein residues within OCP.

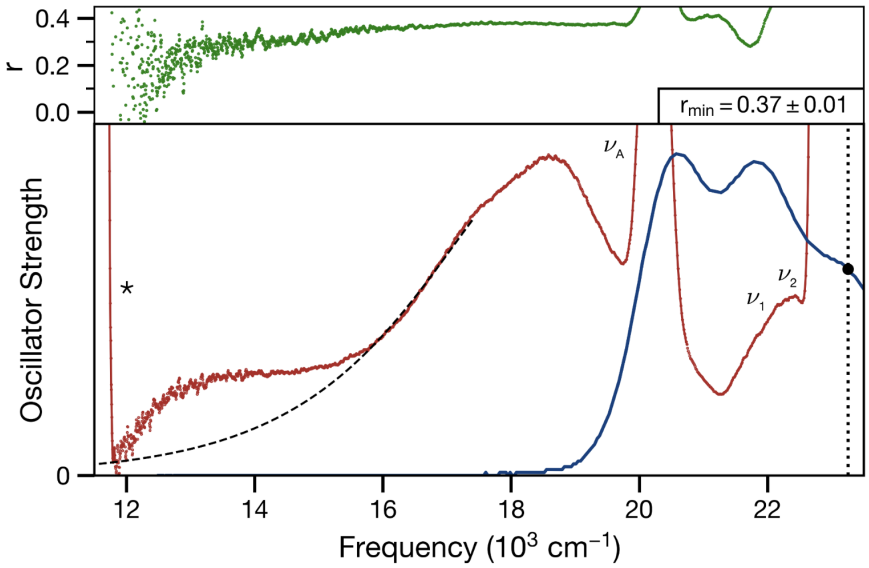

Figure 4.1 Fluorescence oscillator strength, absorbance oscillator strength (blue), and anisotropy (r) spectra for zeaxanthin in 2-MTHF with excitation at 430 nm (23,250 cm^{-1}) at 293 K. The excitation wavenumber is marked with a vertical dashed line. The absorption oscillator strength is arbitrarily scaled to mirror that of the fluorescence emission line shape. The positions of resonance Raman peaks from zeaxanthin (ν_1 = 1517 cm^{-1} and ν_2 = 1157 cm^{-1})[141] and for a non-resonance Raman peak from the 2-MTHF solvent (ν_A = 2966 cm^{-1})[142] are marked.

4.2 Franck-Condon Coordinates of Peridinin Fluorescence and Absorbance

The highly asymmetric carotenoid peridinin (Scheme 5) belongs to the C_S symmetry group, yet it exhibits absorbance properties similar to standard C_{2h} carotenoids - specifically, one-photon excitation is prohibited.[26,104,172] However, unlike other carotenoids, peridinin is known to have a high fluorescence quantum yield emitting from the S_1 state.

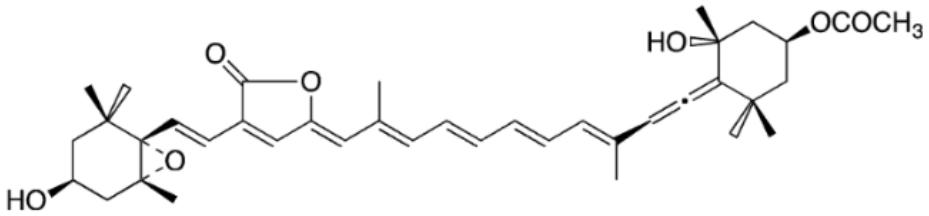

Scheme 5: Structure of peridinin.

Despite the apparent molecular differences between peridinin and C_{2h} carotenoids such as canthaxanthin, they likely have similar absorption properties due to a displacement of the S_1

potential energy surface on a nonlinear coordinate.[25,39,40,104,110] Preliminary measurements of emission anisotropy from peridinin indicate that the molecule immediately undergoes torsional distortion following optical preparation of the S_2 energy level, as the S_X and S_1 regions of emission are decreasing in anisotropy, suggesting relaxation back to the planar ground state. Additional measurements of peridinin fluorescence anisotropy as varying temperature may inhibit torsional distortion in the excited state, increasing the amount of emission from the S_2 state.

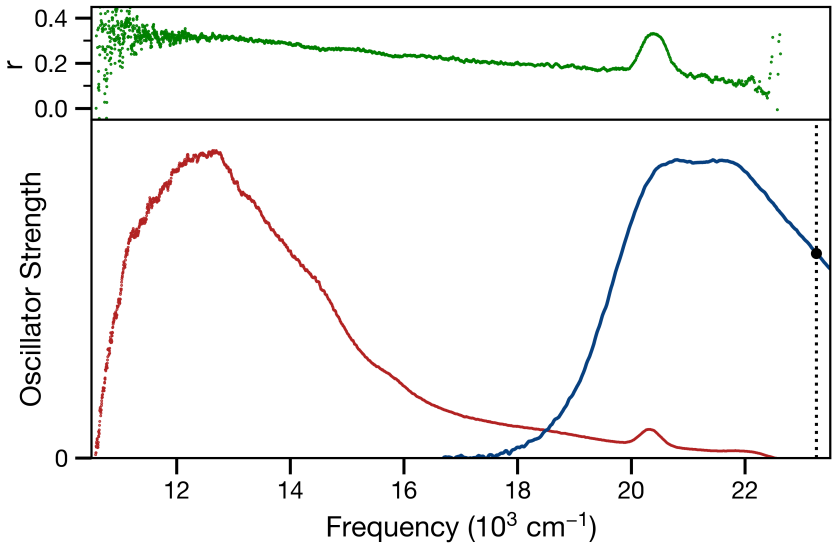

Figure 4.2 Fluorescence oscillator strength (red), absorbance oscillator strength (blue), and anisotropy (r) spectra for peridinin in 2-MTHF with excitation at 430 nm (23,250 cm^{-1}) at 293 K. The excitation wavenumber is marked with a vertical dashed line. The absorption oscillator strength is arbitrarily scaled to mirror that of the fluorescence emission line shape.

REFERENCES

[1] Kay Holt, T.; Krogmann, D. W. A carotenoid-protein from cyanobacteria. *Biochimica et Biophysica Acta (BBA) - Bioenergetics* **1981**, *637*, 408–414.

[2] Gurchiek, J. K.; Bao, H.; Domínguez-Martín, M. A.; McGovern, S. E.; Marquardt, C. E.; Roscioli, J. D.; Ghosh, S.; Kerfeld, C. A.; Beck, W. F. Fluorescence and Excited-State Conformational Dynamics of the Orange Carotenoid Protein. *J. Phys. Chem. B* **2018**, *122*, 1792–1800.

[3] Kerfeld, C. A.; Sawaya, M. R.; Brahmandam, V.; Cascio, D.; Ho, K. K.; Trevithick-Sutton, C. C.; Krogmann, D. W.; Yeates, T. O. The crystal structure of a cyanobacterial water-soluble carotenoid binding protein. *Structure* **2003**, *11*, 55–65.

[4] Rakhimberdieva, M. G.; Stadnichuk, I. N.; Elanskaya, I. V.; Karapetyan, N. V. Carotenoid-induced quenching of the phycobilisome fluorescence in photosystem II-deficient mutant of Synechocystis sp. *FEBS Lett.* **2004**, *574*, 85–88.

[5] Wilson, A.; Ajlani, G.; Verbavatz, J.-M.; Vass, I.; Kerfeld, C. A.; Kirilovsky, D. A soluble carotenoid protein involved in phycobilisome-related energy dissipation in cyanobacteria. *Plant Cell* **2006**, *18*, 992–1007.

[6] Bao, H.; Melnicki, M. R.; Kerfeld, C. A. Structure and functions of Orange Carotenoid Protein homologs in cyanobacteria. *Curr. Opin. Plant Biol.* **2017**, *37*, 1–9.

[7] Wilson, A.; Punginelli, C.; Gall, A.; Bonetti, C.; Alexandre, M.; Routaboul, J.-M.; Kerfeld, C. A.; van Grondelle, R.; Robert, B.; Kennis, J. T. M.; Kirilovsky, D. A photoactive carotenoid protein acting as light intensity sensor. *Proc. Natl. Acad. Sci. U. S. A.* **2008**, *105*, 12075–12080.

[8] Rubinstenn, G.; Vuister, G. W.; Mulder, F. A.; Düx, P. E.; Boelens, R.; Hellingwerf, K. J.; Kaptein, R. Structural and dynamic changes of photoactive yellow protein during its photocycle in solution. *Nat. Struct. Biol.* **1998**, *5*, 568–570.

[9] Harper, S. M.; Neil, L. C.; Gardner, K. H. Structural basis of a phototropin light switch. *Science* **2003**, *301*, 1541–1544.

[10] Wilson, A.; Gwizdala, M.; Mezzetti, A.; Alexandre, M.; Kerfeld, C. A.; Kirilovsky, D. The essential role of the N-terminal domain of the orange carotenoid protein in cyanobacterial photoprotection: importance of a positive charge for phycobilisome binding. *Plant Cell* **2012**, *24*, 1972–1983.

[11] Leverenz, R. L.; Jallet, D.; Li, M.-D.; Mathies, R. A.; Kirilovsky, D.; Kerfeld, C. A. Structural and functional modularity of the orange carotenoid protein: distinct roles for the N- and C-terminal domains in cyanobacterial photoprotection. *Plant Cell* **2014**, *26*, 426–437.

[12] Leverenz, R. L.; Sutter, M.; Wilson, A.; Gupta, S.; Thurotte, A.; Bourcier de Carbon, C.; Petzold, C. J.; Ralston, C.; Perreau, F.; Kirilovsky, D.; Kerfeld, C. A. PHOTOSYNTHESIS. A

12 Å carotenoid translocation in a photoswitch associated with cyanobacterial photoprotection. *Science* **2015**, *348*, 1463–1466.

[13] Gurchiek, J. K.; Bao, H.; Domínguez-Martín, M. A.; McGovern, S. E.; Marquardt, C. E.; Roscioli, J. D.; Ghosh, S.; Kerfeld, C. A.; Beck, W. F. Fluorescence and Excited-State Conformational Dynamics of the Orange Carotenoid Protein. *J. Phys. Chem. B* **2018**, *122*, 1792–1800.

[14] Punginelli, C.; Wilson, A.; Routaboul, J.-M.; Kirilovsky, D. Influence of zeaxanthin and echinenone binding on the activity of the orange carotenoid protein. *Biochim. Biophys. Acta* **2009**, *1787*, 280–288.

[15] Polívka, T.; Pullerits, T.; Frank, H. A.; Cogdell, R. J.; Sundström, V. Ultrafast Formation of a Carotenoid Radical in LH2 Antenna Complexes of Purple Bacteria. *J. Phys. Chem. B* **2004**, *108*, 15398–15407.

[16] Polívka, T.; Frank, H. A. Molecular factors controlling photosynthetic light harvesting by carotenoids. *Acc. Chem. Res.* **2010**, *43*, 1125–1134.

[17] Bishop, M. M.; Roscioli, J. D.; Ghosh, S.; Mueller, J. J.; Shepherd, N. C.; Beck, W. F. Vibrationally Coherent Preparation of the Transition State for Photoisomerization of the Cyanine Dye Cy5 in Water. *J. Phys. Chem. B* **2015**, *119*, 6905–6915.

[18] Beck, W. F.; Bishop, M. M.; Roscioli, J. D.; Ghosh, S.; Frank, H. A. Excited state conformational dynamics in carotenoids: dark intermediates and excitation energy transfer. *Arch. Biochem. Biophys.* **2015**, *572*, 175–183.

[19] Ghosh, S.; Bishop, M. M.; Roscioli, J. D.; Mueller, J. J.; Shepherd, N. C.; LaFountain, A. M.; Frank, H. A.; Beck, W. F. Femtosecond Heterodyne Transient-Grating Studies of Nonradiative Decay of the S2 (1(1)Bu(+)) State of β-Carotene: Contributions from Dark Intermediates and Double-Quantum Coherences. *J. Phys. Chem. B* **2015**, *119*, 14905–14924.

[20] Hashimoto, H.; Uragami, C.; Yukihira, N.; Gardiner, A. T.; Cogdell, R. J. Understanding/unravelling carotenoid excited singlet states. *J. R. Soc. Interface* **2018**, *15*.

[21] Polívka, T.; Sundström, V. Dark excited states of carotenoids: Consensus and controversy. *Chem. Phys. Lett.* **2009**, *477*, 1–11.

[22] Warshel, A.; Karplus, M. Calculation of pi-pi excited state conformations and vibronic structure of retinal and related molecules. *J. Am. Chem. Soc.* **1974**, *96*, 5677–5689.

[23] Warshel, A. Bicycle-pedal model for the first step in the vision process. *Nature* **1976**, *260*, 679–683.

[24] Fiedor, L.; Heriyanto; Fiedor, J.; Pilch, M. Effects of Molecular Symmetry on the Electronic Transitions in Carotenoids. *J. Phys. Chem. Lett.* **2016**, *7*, 1821–1829.

[25] Fiedor, L.; Dudkowiak, A.; Pilch, M. The origin of the dark S1 state in carotenoids: a comprehensive model. *J. R. Soc. Interface* **2019**, *16*, 20190191.

[26] Zigmantas, D.; Polívka, T.; Hiller, R. G.; Yartsev, A.; Sundström, V. Spectroscopic and Dynamic Properties of the Peridinin Lowest Singlet Excited States. *J. Phys. Chem. A* **2001**, *105*, 10296–10306.

[27] Kuhlman, T. S.; Glover, W. J.; Mori, T.; Møller, K. B.; Martínez, T. J. Between ethylene and polyenes–the non-adiabatic dynamics of cis-dienes. *Faraday Discuss.* **2012**, *157*, 193–212; discussion 243–84.

[28] Levine, B. G.; Martínez, T. J. Ab initio multiple spawning dynamics of excited butadiene: role of charge transfer. *J. Phys. Chem. A* **2009**, *113*, 12815–12824.

[29] Shu, Y.; Truhlar, D. G. Doubly Excited Character or Static Correlation of the Reference State in the Controversial 2^1A_g State of trans-Butadiene? *J. Am. Chem. Soc.* **2017**, *139*, 13770–13778.

[30] Glover, W. J.; Mori, T.; Schuurman, M. S.; Boguslavskiy, A. E.; Schalk, O.; Stolow, A.; Martínez, T. J. Excited state non-adiabatic dynamics of the smallest polyene, trans 1,3-butadiene. II. Ab initio multiple spawning simulations. *J. Chem. Phys.* **2018**, *148*, 164303.

[31] Spezia, R.; Knecht, S.; Mennucci, B. Excited state characterization of carbonyl containing carotenoids: a comparison between single and multireference descriptions. *Phys. Chem. Chem. Phys.* **2017**, *19*, 17156–17166.

[32] Andreussi, O.; Knecht, S.; Marian, C. M.; Kongsted, J.; Mennucci, B. Carotenoids and light-harvesting: from DFT/MRCI to the Tamm-Dancoff approximation. *J. Chem. Theory Comput.* **2015**, *11*, 655–666.

[33] Ghosh, S.; Bishop, M. M.; Roscioli, J. D.; LaFountain, A. M.; Frank, H. A.; Beck, W. F. Femtosecond Heterodyne Transient Grating Studies of Nonradiative Deactivation of the S2 (1(1)Bu(+)) State of Peridinin: Detection and Spectroscopic Assignment of an Intermediate in the Decay Pathway. *J. Phys. Chem. B* **2016**, *120*, 3601–3614.

[34] Sashima, T.; Koyama, Y.; Yamada, T.; Hashimoto, H. The 1Bu+, 1Bu-, and 2Ag- Energies of Crystalline Lycopene, β-Carotene, and Mini-9-β-carotene as Determined by Resonance-Raman Excitation Profiles: Dependence of the 1Bu- State Energy on the Conjugation Length. *J. Phys. Chem. B* **2000**, *104*, 5011–5019.

[35] Cerullo, G.; Polli, D.; Lanzani, G.; De Silvestri, S.; Hashimoto, H.; Cogdell, R. J. Photosynthetic light harvesting by carotenoids: detection of an intermediate excited state. *Science* **2002**, *298*, 2395–2398.

[36] Polli, D.; Cerullo, G.; Lanzani, G.; De Silvestri, S.; Yanagi, K.; Hashimoto, H.; Cogdell, R. J. Conjugation length dependence of internal conversion in carotenoids: role of the intermediate state. *Phys. Rev. Lett.* **2004**, *93*, 163002.

[37] Ostroumov, E.; Müller, M. G.; Marian, C. M.; Kleinschmidt, M.; Holzwarth, A. R. Electronic coherence provides a direct proof for energy-level crossing in photoexcited lutein and beta-carotene. *Phys. Rev. Lett.* **2009**, *103*, 108302.

[38] Ostroumov, E. E.; Mulvaney, R. M.; Cogdell, R. J.; Scholes, G. D. Broadband 2D electronic spectroscopy reveals a carotenoid dark state in purple bacteria. *Science* **2013**, *340*, 52–56.

[39] Ghosh, S.; Bishop, M. M.; Roscioli, J. D.; others Femtosecond Heterodyne Transient Grating Studies of Nonradiative Deactivation of the S2 (11Bu+) State of Peridinin: Detection and Spectroscopic Assignment of . . . . *The Journal of* **2016**,

[40] Ghosh, S.; Roscioli, J. D.; Bishop, M. M.; Gurchiek, J. K.; LaFountain, A. M.; Frank, H. A.; Beck, W. F. Torsional Dynamics and Intramolecular Charge Transfer in the S2 (1(1)Bu(+)) Excited State of Peridinin: A Mechanism for Enhanced Mid-Visible Light Harvesting. *J. Phys. Chem. Lett.* **2016**, *7*, 3621–3626.

[41] Gillbro, T.; Cogdell, R. J. Carotenoid fluorescence. *Chem. Phys. Lett.* **1989**, *158*, 312–316.

[42] Gurchiek, J. K.; Rose, J. B.; Guberman-Pfeffer, M. J.; Tilluck, R. W.; Ghosh, S.; Gascón, J. A.; Beck, W. F. Fluorescence Anisotropy Detection of Barrier Crossing and Ultrafast Conformational Dynamics in the S2 State of β-Carotene. *J. Phys. Chem. B* **2020**, *124*, 9029–9046.

[43] Siano, D. B.; Metzler, D. E. Band Shapes of the Electronic Spectra of Complex Molecules. *J. Chem. Phys.* **1969**, *51*, 1856–1861.

[44] Wu, Y. P.; Krogmann, D. W. The orange carotenoid protein of *Synechocystis* PCC 6803. *Biochim. Biophys. Acta* **1997**, *1322*, 1–7.

[45] Kerfeld, C. A.; Sawaya, M. R.; Brahmandam, V.; Cascio, D.; Ho, K. K.; Trevithick-Sutton, C. C.; Krogmann, D. W.; Yeates, T. O. The crystal structure of a cyanobacterial water-soluble carotenoid binding protein. *Structure* **2003**, *11*, 55–65.

[46] Kerfeld, C. A. Water-soluble carotenoid proteins of cyanobacteria. *Arch. Biochem. Biophys.* **2004**, *430*, 2–9.

[47] Wilson, A.; Ajlani, G.; Verbavatz, J. M.; Vass, I.; Kerfeld, C. A.; Kirilovsky, D. A soluble carotenoid protein involved in phycobilisome-related energy dissipation in cyanobacteria. *Plant Cell* **2006**, *18*, 992–1007.

[48] Boulay, C.; Abasova, L.; Six, C.; Vass, I.; Kirilovsky, D. Occurrence and function of the orange carotenoid protein in photoprotective mechanisms in various cyanobacteria. *Biochim. Biophys. Acta* **2008**, *1777*, 1344–1354.

[49] Wilson, A.; Punginelli, C.; Gall, A.; Bonetti, C.; Alexandre, M.; Routaboul, J. M.; Kerfeld, C. A.; van Grondelle, R.; Robert, B.; Kennis, J. T.; Kirilovsky, D. A photoactive carotenoid protein acting as light intensity sensor. *Proc. Natl. Acad. Sci. U. S. A.* **2008**, *105*, 12075–12080.

[50] Berera, R.; van Stokkum, I. H. M.; d'Haene, S.; Kennis, J. T. M.; van Grondelle, R.; Dekker, J. P. A mechanism of energy dissipation in cyanobacteria. *Biophys. J.* **2009**, *96*, 2261–2267.

[51] Wilson, A.; Kinney, J. N.; Zwart, P. H.; Punginelli, C.; D'Haene, S.; Perreau, F.; Klein, M. G.; Kirilovsky, D.; Kerfeld, C. A. Structural determinants underlying photoprotection in the photoactive orange carotenoid protein of cyanobacteria. *J. Biol. Chem.* **2010**, *285*, 18364–18375.

[52] Gupta, S.; Guttman, M.; Leverenz, R. L.; Zhumadilova, K.; Pawlowski, E. G.; Petzold, C. J.; Lee, K. K.; Ralston, C. Y.; Kerfeld, C. A. Local and global structural drivers for the photoactivation of the orange carotenoid protein. *Proc. Natl. Acad. Sci. U. S. A.* **2015**, *112*, E5567–74.

[53] Leverenz, R. L.; Sutter, M.; Wilson, A.; Gupta, S.; Thurotte, A.; de Carbon, C. B.; Petzold, C. J.; Ralston, C.; Perreau, F.; Kirilovsky, D.; Kerfeld, C. A. A 12 Å carotenoid translocation in a photoswitch associated with cyanobacterial photoprotection. *Science* **2015**, *348*, 1463–1466.

[54] Kirilovsky, D.; Kerfeld, C. A. Cyanobacterial photoprotection by the orange carotenoid protein. *Nat Plants* **2016**, *2*, 16180.

[55] Domínguez-Martín, M. A.; Sauer, P. V.; Kirst, H.; Sutter, M.; Bína, D.; Greber, B. J.; Nogales, E.; Polívka, T.; Kerfeld, C. A. Structures of a phycobilisome in light-harvesting and photoprotected states. *Nature* **2022**, *609*, 835–845.

[56] Zhang, H.; Liu, H.; Niedzwiedzki, D. M.; Prado, M.; Jiang, J.; Gross, M. L.; Blankenship, R. E. Molecular mechanism of photoactivation and structural location of the cyanobacterial orange carotenoid protein. *Biochemistry* **2014**, *53*, 13–19.

[57] Liu, H.; Zhang, H.; Orf, G. S.; Lu, Y.; Jiang, J.; King, J. D.; Wolf, N. R.; Gross, M. L.; Blankenship, R. E. Dramatic Domain Rearrangements of the Cyanobacterial Orange Carotenoid Protein upon Photoactivation. *Biochemistry* **2016**, *55*, 1003–1009.

[58] Rose, J. B.; Gascón, J. A.; Sutter, M.; Sheppard, D. I.; Kerfeld, C. A.; Beck, W. F. Photoactivation of the orange carotenoid protein requires two light-driven reactions mediated by a metastable monomeric intermediate. *Phys. Chem. Chem. Phys.* **2023**,

[59] Šlouf, V.; Kuznetsova, V.; Fuciman, M.; de Carbon, C. B.; Wilson, A.; Kirilovsky, D.; Polívka, T. Ultrafast spectroscopy tracks carotenoid configurations in the orange and red carotenoid proteins from cyanobacteria. *Photosynth. Res.* **2017**, *131*, 105–117.

[60] Konold, P. E.; van Stokkum, I. H. M.; Muzzopappa, F.; Wilson, A.; Groot, M.-L.; Kirilovsky, D.; Kennis, J. T. M. Photoactivation Mechanism, Timing of Protein Secondary Structure Dynamics and Carotenoid Translocation in the Orange Carotenoid Protein. *J. Am. Chem. Soc.* **2019**, *141*, 520–530.

[61] Polívka, T.; Sundström, V. Dark excited states of carotenoids: consensus and controversy. *Chem. Phys. Lett.* **2009**, *477*, 1–11.

[62] Yaroshevich, I. A. et al. Role of hydrogen bond alternation and charge transfer states in photoactivation of the Orange Carotenoid Protein. *Commun Biol* **2021**, *4*, 539.

[63] Niziński, S.; Wilson, A.; Uriarte, L. M.; Ruckebusch, C.; Andreeva, E. A.; Schlichting, I.; Colletier, J.-P.; Kirilovsky, D.; Burdzinski, G.; Sliwa, M. Unifying Perspective of the Ultrafast Photodynamics of Orange Carotenoid Proteins from *Synechocystis*: Peril of High-Power Excitation, Existence of Different S* States, and Influence of Tagging. *JACS Au* **2022**, *2*, 1084–1095.

[64] Chukhutsina, V. U.; Baxter, J. M.; Fadini, A.; Morgan, R. M.; Pope, M. A.; Maghlaoui, K.; Orr, C. M.; Wagner, A.; van Thor, J. J. Light activation of Orange Carotenoid Protein reveals bicycle-pedal single-bond isomerization. *Nat. Commun.* **2022**, *13*, 6420.

[65] Warshel, A. Bicycle-pedal model for the first step in the vision process. *Nature* **1976**, *260*, 679–683.

[66] Wang, Q.; Schoenlein, R. W.; Peteanu, L. A.; Mathies, R. A.; Shank, C. V. Vibrationally coherent photochemistry in the femtosecond primary event of vision. *Science* **1994**, *266*, 422–424.

[67] Mathies, R. A. Photochemistry: A coherent picture of vision. *Nat. Chem.* **2015**, *7*, 945–947.

[68] Niziński, S.; Schlichting, I.; Colletier, J.-P.; Kirilovsky, D.; Burdzinski, G.; Sliwa, M. Is orange carotenoid protein photoactivation a single-photon process? *Biophys Rep* **2022**, *2*, 100072.

[69] Maksimov, E. G.; Shirshin, E. A.; Sluchanko, N. N.; Zlenko, D. V.; Parshina, E. Y.; Tsoraev, G. V.; Klementiev, K. E.; Budylin, G. S.; Schmitt, F.-J.; Friedrich, T.; Fadeev, V. V.; Paschenko, V. Z.; Rubin, A. B. The Signaling State of Orange Carotenoid Protein. *Biophys. J.* **2015**, *109*, 595–607.

[70] Cunningham, F. X.; Gantt, E. A portfolio of plasmids for identification and analysis of carotenoid pathway enzymes: *Adonis aestivalis* as a case study. *Photosynth. Res.* **2007**, *92*, 245–259.

[71] Polívka, T.; Sundström, V. Ultrafast dynamics of carotenoid excited States—from solution to natural and artificial systems. *Chem. Rev.* **2004**, *104*, 2021–2071.

[72] van Stokkum, I. H. M.; Larsen, D. S.; van Grondelle, R. Global and target analysis of time-resolved spectra. *Biochim. Biophys. Acta* **2004**, *1657*, 82–104.

[73] Hirai, M.; Ajito, S.; Sugiyama, M.; Iwase, H.; Takata, S.-I.; Shimizu, N.; Igarashi, N.; Martel, A.; Porcar, L. Direct Evidence for the Effect of Glycerol on Protein Hydration and Thermal Structural Transition. *Biophys. J.* **2018**, *115*, 313–327.

[74] Fleming, G. R.; Cho, M. Chromophore-solvent dynamics. *Annu. Rev. Phys. Chem.* **1996**, *47*, 109–134.

[75] Ghosh, S.; Bishop, M. M.; Roscioli, J. D.; Mueller, J. J.; Shepherd, N. C.; LaFountain, A. M.; Frank, H. A.; Beck, W. F. Femtosecond Heterodyne Transient-Grating Studies of Nonradiative Decay of the S_2 ($1^1B_u^+$) State of β-Carotene: Contributions from Dark Intermediates and Double-Quantum Coherences. *J. Phys. Chem. B* **2015**, *119*, 14905–14924.

[76] Ghosh, S.; Bishop, M. M.; Roscioli, J. D.; LaFountain, A. M.; Frank, H. A.; Beck, W. F. Femtosecond heterodyne transient grating studies of nonradiative deactivation of the S_2 ($1^1B_u^+$) state of peridinin: detection and spectroscopic assignment of an intermediate in the decay pathway. *J. Phys. Chem. B* **2016**, *120*, 3601–3614.

[77] Marcus, R. A. On the theory of oxidation-reduction reactions involving electron transfer. I. *J. Chem. Phys.* **1956**, *24*, 966–989.

[78] Balevičius, V., Jr; Pour, A. G.; Savolainen, J.; Lincoln, C. N.; Lukeš, V.; Riedle, E.; Valkunas, L.; Abramavicius, D.; Hauer, J. Vibronic energy relaxation approach highlighting deactivation pathways in carotenoids. *Phys. Chem. Chem. Phys.* **2015**, *17*, 19491–19499.

[79] Kish, E.; Pinto, M. M.; Kirilovsky, D.; Spezia, R.; Robert, B. Echinenone vibrational properties: From solvents to the orange carotenoid protein. *Biochim. Biophys. Acta* **2015**, *1847*, 1044–1054.

[80] Kerfeld, C. A.; Melnicki, M. R.; Sutter, M.; Dominguez-Martin, M. A. Structure, function and evolution of the cyanobacterial orange carotenoid protein and its homologs. *New Phytol.* **2017**, *215*, 937–951.

[81] Pigni, N. B.; Clark, K. L.; Beck, W. F.; Gascón, J. A. Spectral Signatures of Canthaxanthin Translocation in the Orange Carotenoid Protein. *J. Phys. Chem. B* **2020**, *124*, 11387–11395.

[82] Maksimov, E. G.; Sluchanko, N. N.; Mironov, K. S.; Shirshin, E. A.; Klementiev, K. E.; Tsoraev, G. V.; Moldenhauer, M.; Friedrich, T.; Los, D. A.; Allakhverdiev, S. I.; Paschenko, V. Z.; Rubin, A. B. Fluorescent labeling preserving OCP photoactivity reveals its reorganization during the photocycle. *Biophys. J.* **2017**, *112*, 827.

[83] Sharawy, M.; Pigni, N. B.; May, E. R.; Gascón, J. A. A favorable path to domain separation in the orange carotenoid protein. *Protein Sci.* **2022**, *31*, 850–863.

[84] Polívka, T.; Sundström, V. Ultrafast dynamics of carotenoid excited states—from solution to natural and artificial systems. *Chem. Rev.* **2004**, *104*, 2021–2071.

[85] Beck, W. F.; Bishop, M. M.; Roscioli, J. D.; Ghosh, S.; Frank, H. A. Excited state conformational dynamics in carotenoids: dark intermediates and excitation energy transfer. *Arch. Biochem. Biophys.* **2015**, *572*, 175–183.

[86] Tully, J. C. Perspective: Nonadiabatic dynamics theory. *J. Chem. Phys.* **2012**, *137*, 22A301.

[87] Levine, B. G. Nonadiabatic dynamics of *cis–trans* photoisomerization—a first principles study. Ph.D. thesis, University of Illinois at Urbana-Champagne, Urbana, Illinois, 2007.

[88] Gillbro, T.; Cogdell, R. J. Carotenoid fluorescence. *Chem. Phys. Lett.* **1989**, *158*, 312–316.

[89] Demchenko, A. P.; Tomin, V. I.; Chou, P.-T. Breaking the Kasha Rule for More Efficient Photochemistry. *Chem. Rev.* **2017**, *117*, 13353–13381.

[90] Christensen, R. L. The Electronic States of Carotenoids. In *The Photochemistry of Carotenoids*; Frank, H. A., Young, A. J., Britton, G., Cogdell, R. J., Eds.; Springer Netherlands: Dordrecht, 1999; pp 137–159.

[91] Frank, H. A.; Christensen, R. L. Excited electronic states and the photochemistry and photophysics of carotenoids. In *The Carotenoids*; Britton, G., Liaaen-Jensen, S., Pfander, H., Eds.; Birkhauser Verlag: Basel, 2008; pp 167–188.

[92] Schulten, K.; Karplus, M. On the origin of a low-lying forbidden transition in polyenes and related molecules. *Chem. Phys. Lett.* **1972**, *14*, 305–309.

[93] Hudson, B.; Kohler, B. Linear Polyene Electronic Structure and Spectroscopy. *Annu. Rev. Phys. Chem.* **1974**, *25*, 437–460.

[94] Holtom, G. R.; McClain, W. M. Two-photon excitation spectra of the low energy excited states of diphenylhexatriene and diphenyloctatetraene. *Chem. Phys. Lett.* **1976**, *44*, 436–439.

[95] Nagae, H.; Kuki, M.; Zhang, J.-P.; Sashima, T.; Mukai, Y.; Koyama, Y. Vibronic Coupling through the In-Phase, C=C Stretching Mode Plays a Major Role in the $2A_g^-$ to $1A_g^-$ Internal Conversion of all-*trans*-β-Carotene. *J. Phys. Chem. A* **2000**, *104*, 4155–4166.

[96] Yarkony, D. R. Conical intersections: diabolical and often misunderstood. *Acc. Chem. Res.* **1998**, *31*, 511–518.

[97] Levine, B. G.; Martínez, T. J. Isomerization through conical intersections. *Annu. Rev. Phys. Chem.* **2007**, *58*, 613–634.

[98] Wasielewski, M. R.; Kispert, L. D. Direct measurement of the lowest excited singlet state lifetime of all-trans-β-carotene and related carotenoids. *Chem. Phys. Lett.* **1986**, *128*, 238–243.

[99] Frank, H. A.; Bautista, J. A.; Josue, J.; Pendon, Z.; Hiller, R. G.; Sharples, F. P.; Gosztola, D.; Wasielewski, M. R. Effect of the solvent environment on the spectroscopic properties and dynamics of the lowest excited states of carotenoids. *J. Phys. Chem. B* **2000**, *104*, 4569–4577.

[100] Hemley, R.; Kohler, B. E. Electronic structure of polyenes related to the visual chromophore. A simple model for the observed band shapes. *Biophys. J.* **1977**, *20*, 377–382.

[101] Requena, A.; Ceron-Carrasco, J. P.; Bastida, A.; Zuniga, J.; Miguel, B. A Density Functional Theory Study of the Structure and Vibrational Spectra of β-Carotene, Capsanthin, and Capsorubin. *J. Phys. Chem. A* **2008**, *112*, 4815–4825.

[102] Fiedor, L.; Pilch, M. Side Methyl Groups Control the Conformation and Contribute to Symmetry Breaking of Isoprenoid Chromophores. *Angew. Chem. Int. Ed Engl.* **2018**, *57*, 6501–6506.

[103] Andersson, P. O.; Takaichi, S.; Cogdell, R. J.; Gillbro, T. Photophysical Characterization of Natural *cis*-Carotenoids. *Photochem. Photobiol.* **2001**, *74*, 549–557.

[104] Fiedor, L.; Heriyanto; Fiedor, J.; Pilch, M. Effects of molecular symmetry on the electronic transitions in carotenoids. *J. Phys. Chem. Lett.* **2016**, *7*, 1821–1829.

[105] Wei, T.; Balevičius, V.; Polívka, T.; Ruban, A. V.; Duffy, C. D. P. How carotenoid distortions may determine optical properties: lessons from the Orange Carotenoid Protein. *Phys. Chem. Chem. Phys.* **2019**, *21*, 23187–23197.

[106] Cerullo, G.; Polli, D.; Lanzani, G.; De Silvestri, S.; Hashimoto, H.; Cogdell, R. J. Photosynthetic light harvesting by carotenoids: detection of an intermediate excited state. *Science* **2002**, *298*, 2395–2398.

[107] Ostroumov, E.; Müller, M. G.; Marian, C. M.; Kleinschmidt, M.; Holzwarth, A. R. Electronic coherence provides a direct proof for energy-level crossing in photoexcited lutein and β-carotene. *Phys. Rev. Lett.* **2009**, *103*, 108302.

[108] Ostroumov, E. E.; Mulvaney, R. M.; Cogdell, R. J.; Scholes, G. D. Broadband 2D electronic spectroscopy reveals a carotenoid dark state in purple bacteria. *Science* **2013**, *340*, 52–56.

[109] Tavan, P.; Schulten, K. Electronic excitations in finite and infinite polyenes. *Phys. Rev. B Condens. Matter* **1987**, *36*, 4337–4358.

[110] Ghosh, S.; Roscioli, J. D.; Bishop, M. M.; Gurchiek, J. K.; LaFountain, A. M.; Frank, H. A.; Beck, W. F. Torsional Dynamics and Intramolecular Charge Transfer in the S_2 ($1^1B_u{}^+$) Excited State of Peridinin: A Mechanism for Enhanced Mid-Visible Light Harvesting. *J. Phys. Chem. Lett.* **2016**, *7*, 3621–3626.

[111] Sanchez-Galvez, A.; Hunt, P.; Robb, M. A.; Olivucci, M.; Vreven, T.; Schlegel, H. B. Ultrafast Radiationless Deactivation of Organic Dyes: Evidence for a Two-State Two-Mode Pathway in Polymethine Cyanines. *J. Am. Chem. Soc.* **2000**, *122*, 2911–2924.

[112] Ben-Nun, M.; Martınez, T. J. Photodynamics of ethylene: ab initio studies of conical intersections. *Chem. Phys.* **2000**, *259*, 237–248.

[113] de Weerd, F. L.; van Stokkum, I. H. M.; van Grondelle, R. Subpicosecond dynamics in the excited state absorption of all-*trans*-β-carotene. *Chem. Phys. Lett.* **2002**, *354*, 38–43.

[114] Bonačić-Koutecký, V.; Bruckmann, P.; Hiberty, P.; Koutecký, J.; Leforestier, C.; Salem, L. Sudden polarization in the zwitterionic Z1 excited states of organic intermediates. Photochemical implications. *Angew. Chem. Int. Ed.* **1975**, *14*, 575–576.

[115] Bonačić-Koutecký, V.; Koutecký, J.; Michl, J. Neutral and charged biradicals, zwitterions, funnels in S_1, and proton translocation: Their role in photochemistry, photophysics, and vision. *Angew. Chem. Int. Ed.* **1987**, *26*, 170–189.

[116] Michl, J.; Bonačić-Koutecký, V. *Electronic Aspects of Organic Photochemistry*; Wiley: New York, 1990.

[117] Liebel, M.; Schnedermann, C.; Kukura, P. Vibrationally coherent crossing and coupling of electronic states during internal conversion in β-carotene. *Phys. Rev. Lett.* **2014**, *112*, 198302.

[118] Hudson, B. S.; Kohler, B. E.; Schulten, K. Linear Polyene Electronic Structure and Potential Surfaces. In *Excited States*; Lim, E. C., Ed.; Elsevier, 1982; Vol. 6; pp 1–95.

[119] Birge, R. R.; Zgierski, M. Z.; Serrano-Andres, L.; Hudson, B. S. Transition Dipole Orientation of Linear Polyenes: Semiempirical Models and Extrapolation to the Infinite Chain Limit. *J. Phys. Chem. A* **1999**, *103*, 2251–2255.

[120] Dolan, P. M.; Miller, D.; Cogdell, R. J.; Birge, R. R.; Frank, H. A. Linear Dichroism and the Transition Dipole Moment Orientation of the Carotenoid in the LH2 Antenna Complex in Membranes of *Rhodopseudomonas acidophila* Strain 10050. *J. Phys. Chem. B* **2001**, *105*, 12134–12142.

[121] Enriquez, M. M.; Fuciman, M.; LaFountain, A. M.; Wagner, N. L.; Birge, R. R.; Frank, H. A. The intramolecular charge transfer state in carbonyl-containing polyenes and carotenoids. *J. Phys. Chem. B* **2010**, *114*, 12416–12426.

[122] Niedzwiedzki, D. M.; Enriquez, M. M.; Lafountain, A. M.; Frank, H. A. Ultrafast Time-resolved Absorption Spectroscopy of Geometric Isomers of Xanthophylls. *Chem. Phys.* **2010**, *373*, 80–89.

[123] Lakowicz, J. R. *Principles of Fluorescence Spectroscopy*, 3rd ed.; Springer US: New York, 2011.

[124] Ameloot, M.; vandeVen, M.; Acuña, A. U.; Valeur, B. Fluorescence anisotropy measurements in solution: Methods and reference materials (IUPAC Technical Report). *J. Macromol. Sci. Part A Pure Appl. Chem.* **2013**, *85*, 589–608.

[125] Prazeres, T. J. V.; Fedorov, A.; Barbosa, S. P.; Martinho, J. M. G.; Berberan-Santos, M. N. Accurate determination of the limiting anisotropy of rhodamine 101. Implications for its use as a fluorescence polarization standard. *J. Phys. Chem. A* **2008**, *112*, 5034–5039.

[126] Johansson, L. B.-Å. Limiting fluorescence anisotropies of perylene and xanthene derivatives. *J. Chem. Soc. Faraday Trans.* **1990**, *86*, 2103–2107.

[127] Magde, D.; Wong, R.; Seybold, P. G. Fluorescence quantum yields and their relation to lifetimes of rhodamine 6G and fluorescein in nine solvents: improved absolute standards for quantum yields. *Photochem. Photobiol.* **2002**, *75*, 327–334.

[128] Siano, D. B.; Metzler, D. E. Band Shapes of the Electronic Spectra of Complex Molecules. *J. Chem. Phys.* **1969**, *51*, 1856–1861.

[129] Andersson, P. O.; Gillbro, T.; Asato, A. E.; Liu, R. S. H. Dual singlet state emission in a series of mini-carotenes. *J. Lumin.* **1992**, *51*, 11–20.

[130] Becke, A. D. Density-functional thermochemistry. III. The role of exact exchange. *J. Chem. Phys.* **1993**, *98*, 5648–5652.

[131] Stephens, P. J.; Devlin, F. J.; Chabalowski, C. F.; Frisch, M. J. Ab Initio Calculation of Vibrational Absorption and Circular Dichroism Spectra Using Density Functional Force Fields. *J. Phys. Chem.* **1994**, *98*, 11623–11627.

[132] Frisch, M. J. et al. Gaussian 16 Rev. A.01. 2016.

[133] Yanai, T.; Tew, D. P.; Handy, N. C. A new hybrid exchange–correlation functional using the Coulomb-attenuating method (CAM-B3LYP). *Chem. Phys. Lett.* **2004**, *393*, 51–57.

[134] Lu, T.; Chen, F. Multiwfn: a multifunctional wavefunction analyzer. *J. Comput. Chem.* **2012**, *33*, 580–592.

[135] Cantor, C. R.; Schimmel, P. R. *Biophysical Chemistry. Part II: Techniques for the Study of Biological Structure and Function*; W. H. Freeman and Company: San Francisco, 1980.

[136] Yu, A.; Tolbert, C. A.; Farrow, D. A.; Jonas, D. M. Solvatochromism and Solvation Dynamics of Structurally Related Cyanine Dyes. *J. Phys. Chem. A* **2002**, *106*, 9407–9419.

[137] Ejder, E. Methods of representing emission, excitation, and photoconductivity spectra. *J. Opt. Soc. Amer.* **1969**, *59*, 223–224.

[138] Melhuish, W. H. Absolute spectrofluorimetry. *J. Res. Natl. Bur. Stand.* **1972**, *76A*, 547–560.

[139] Mooney, J.; Kambhampati, P. Get the Basics Right: Jacobian Conversion of Wavelength and Energy Scales for Quantitative Analysis of Emission Spectra. *J. Phys. Chem. Lett.* **2013**, *4*, 3316–3318.

[140] Andersson, P. O.; Bachilo, S. M.; Chen, R.-L.; Gillbro, T. Solvent and Temperature Effects on Dual Fluorescence in a Series of Carotenes. Energy Gap Dependence of the Internal Conversion Rate. *J. Phys. Chem.* **1995**, *99*, 16199–16209.

[141] Saito, S.; Tasumi, M.; Eugster, C. H. Resonance Raman spectra (5800-40 cm1) of All-trans and 15-cis isomers of β-carotene in the solid state and in solution. Measurements with various laser lines from ultraviolet to red. *J. Raman Spectrosc.* **1983**, *14*, 299–309.

[142] Sverdlov, L. M.; Kovner, M. A.; Kraĭ *Vibrational spectra of polyatomic molecules*; John Wiley & Sons, 1973.

[143] Ricci, M.; Torre, R.; Foggi, P.; Kamalov, V.; Righini, R. Molecular dynamics of β-carotene in solution by resonance enhanced optical Kerr effect. *J. Chem. Phys.* **1995**, *102*, 9537.

[144] Bondarev, S. L.; Bachilo, S. M.; Dvornikov, S. S.; Tikhomirov, S. A. $S_2 \rightarrow S_0$ fluorescence and transient $S_n \leftarrow S_1$ absorption of all-trans-β-carotene in solid and liquid solutions. *J. Photochem. Photobiol. A Chem.* **1989**, *46*, 315–322.

[145] Shreve, A. P.; Trautman, J. K.; Owens, T. G.; Albrecht, A. C. Determination of the S_2 lifetime of β-carotene. *Chem. Phys. Lett.* **1991**, *178*, 89–96.

[146] Durig, J. R.; Kizer, K. L.; Karriker, J. M. Spectra and structure of small ring compounds. XXXVI. 2-methyl-1,3-dioxolane; 2-methyl-1,3-dioxolane-d4; 2-methyltetrahydrofuran; and methylcyclopentane. *J. Raman Spectrosc.* **1973**, *1*, 17–45.

[147] Kochendoerfer, G. G.; Mathies, R. A. Spontaneous Emission Study of the Femtosecond Isomerization Dynamics of Rhodopsin. *J. Phys. Chem.* **1996**, *100*, 14526–14532.

[148] Norden, B.; Lindblom, G.; Jonas, I. Linear dichroism spectroscopy as a tool for studying molecular orientation in model membrane systems. *J. Phys. Chem.* **1977**, *81*, 2086–2093.

[149] Mohan T M, N.; Leslie, C. H.; Sil, S.; Rose, J. B.; Tilluck, R. W.; Beck, W. F. Broadband 2DES detection of vibrational coherence in the Sx state of canthaxanthin. *J. Chem. Phys.* **2021**, *155*, 035103.

[150] Andersson, P. O.; Gillbro, T.; Ferguson, L.; Cogdell, R. J. Absorption spectral shifts of carotenoids related to medium polarizability. *Photochem. Photobiol.* **1991**, *54*, 353–360.

[151] Qu, G.; Xin, M.; Jia, Q.; Cai, P.; Jin, G.; Zhou, Y.; Liu, C.; Tan, Y.; Zhang, Y.; Yao, Z.; Feng, A.; Cai, H. Resonance Raman features all-trans-β-carotene during phase transition and theoretical investigation analysis. *Optik* **2019**, *185*, 191–198.

[152] Ling, A. C.; Willard, J. E. Viscosities of some organic glasses used as trapping matrixes. *J. Phys. Chem.* **1968**, *72*, 1918–1923.

[153] Liu, R. S.; Asato, A. E. The primary process of vision and the structure of bathorhodopsin: a mechanism for photoisomerization of polyenes. *Proc. Natl. Acad. Sci. U. S. A.* **1985**, *82*, 259–263.

[154] Liu, R. S. H. Photoisomerization by Hula-Twist: A Fundamental Supramolecular Photochemical Reaction. *Acc. Chem. Res.* **2001**, *34*, 555–562.

[155] Ostroumov, E. E.; Reus; Müller, M. G.; Michael; Holzwarth, A. R. On the Nature of the "Dark S*" Excited State of β-Carotene. *J. Phys. Chem. A* **2011**, *115*, 3698–3712.

[156] Andersson, P. O.; Gillbro, T.; Asato, A. E.; Liu, R. S. H. Temperature and viscosity sensitive S_1 emission from a highly substituted triene. *Chem. Phys. Lett.* **1995**, *235*, 76–82.

[157] Tan, R.-R.; , Shen, X.; , Hu, L.; , Zhang, F.-S.; , Liquid-to-glass transition of tetrahydrofuran and 2-methyltetrahydrofuran. *Chin. Physics B* **2012**, *21*, 086402.

[158] Malhado, J. P.; Spezia, R.; Hynes, J. T. Dynamical friction effects on the photoisomerization of a model protonated Schiff base in solution. *J. Phys. Chem. A* **2011**, *115*, 3720–3735.

[159] Fuß, W.; Haas, Y.; Zilberg, S. Twin states and conical intersections in linear polyenes. *Chem. Phys.* **2000**, *259*, 273–295.

[160] Minezawa, N.; Gordon, M. S. Optimizing conical intersections by spin-flip density functional theory: application to ethylene. *J. Phys. Chem. A* **2009**, *113*, 12749–12753.

[161] Kochendoerfer, G. G.; Mathies, R. A. Ultrafast spectroscopy of rhodopsins—photochemistry at its best! *Isr. J. Chem.* **1995**, *35*, 211–226.

[162] Birge, R. R. Nature of the primary photochemical events in rhodopsin and bacteriorhodopsin. *Biochim. Biophys. Acta* **1990**, *1016*, 293–327.

[163] Kukura, P.; McCamant, D. W.; Yoon, S.; Wandschneider, D. B.; Mathies, R. A. Structural observation of the primary isomerization in vision with femtosecond-stimulated Raman. *Science* **2005**, *310*, 1006–1009.

[164] Schnedermann, C.; Liebel, M.; Kukura, P. Mode-specificity of vibrationally coherent internal conversion in rhodopsin during the primary visual event. *J. Am. Chem. Soc.* **2015**, *137*, 2886–2891.

[165] Hasson, K. C.; Gai, F.; Anfinrud, P. A. The photoisomerization of retinal in bacteriorhodospin: experimental evidence for a three-state model. *Proc. Natl. Acad. Sci. U. S. A.* **1996**, *93*, 15124–15129.

[166] Song, L.; El-Sayed, M. A. Primary Step in Bacteriorhodopsin Photosynthesis: Bond Stretch Rather than Angle Twist of Its Retinal Excited-State Structure. *J. Am. Chem. Soc.* **1998**, *120*, 8889–8890.

[167] Lewis, A.; Spoonhower, J. P.; Perreault, G. J. Observation of light emission from a rhodopsin. *Nature* **1976**, *260*, 675.

[168] Kouyama, T.; Kinosita, K., Jr; Ikegami, A. Excited-state dynamics of bacteriorhodopsin. *Biophys. J.* **1985**, *47*, 43–54.

[169] Haran, G.; Wynne, K.; Xie, A.; He, Q.; Chance, M.; Hochstrasser, R. M. Excited state dynamics of bacteriorhodopsin revealed by transient stimulated emission spectra. *Chem. Phys. Lett.* **1996**, *261*, 389–395.

[170] Nosrati, M.; Berbasova, T.; Vasileiou, C.; Borhan, B.; Geiger, J. H. A Photoisomerizing Rhodopsin Mimic Observed at Atomic Resolution. *J. Am. Chem. Soc.* **2016**, *138*, 8802–8808.

[171] Ghanbarpour, A.; Nairat, M.; Nosrati, M.; Santos, E. M.; Vasileiou, C.; Dantus, M.; Borhan, B.; Geiger, J. H. Mimicking Microbial Rhodopsin Isomerization in a Single Crystal. *J. Am. Chem. Soc.* **2019**, *141*, 1735–1741.

[172] Enriquez, M. M.; Hananoki, S.; Hasegawa, S.; Kajikawa, T.; Katsumura, S.; Wagner, N. L.; Birge, R. R.; Frank, H. A. Effect of Molecular Symmetry on the Spectra and Dynamics of the Intramolecular Charge Transfer (ICT) state of peridinin. *J. Phys. Chem. B* **2012**, *116*, 10748–10756.